August 2014

Propagation of an Optical Vortex in Fiber Arrays with Triangular Lattices

Muhammad Abdulrahman Mushref
University of Wisconsin-Milwaukee

PROPAGATION OF AN OPTICAL VORTEX IN FIBER ARRAYS

WITH TRIANGULAR LATTICES

by

Muhammad Abdulrahman Abdulghani Mushref

A Dissertation Submitted in

Partial Fulfillment of the

Requirements for the Degree of

Doctor of Philosophy

in Engineering

at

The University of Wisconsin-Milwaukee

August 2014

ABSTRACT
PROPAGATION OF AN OPTICAL VORTEX IN FIBER ARRAYS
WITH TRIANGULAR LATTICES

by

Muhammad Abdulrahman Abdulghani Mushref

The University of Wisconsin-Milwaukee, 2014
Under the supervision of Professor Chiu-Tai Law

The propagation of optical vortices (OVs) in linear and nonlinear media is an important

field of research in science and engineering. The most important goal is to explore the

properties of guiding dynamics for potential applications such as sensing, all-optical

switching, frequency mixing and modulation. In this dissertation, we present analytical

methods and numerical techniques to investigate the propagation of an optical vortex in

fiber array waveguides. Analytically, we model wave propagation in a waveguide by

coupled mode Equations as a simplified approximation. The beam propagation method

(BPM) is also employed to numerically solve the paraxial wave Equation by finite

difference (FD) techniques. We will investigate the propagation of fields in a 2D

triangular lattice with different core arrangements in the optical waveguide. In order to

eliminate wave reflections at the boundaries of the computational area, the transparent

boundary condition (TBC) is applied. In our explorations for the propagation properties

of an optical vortex in a linear and a non-linear triangular lattice medium, images are

numerically generated for the field phase and intensity in addition to the interferogram of

the vortex field with a reference plane or Gaussian field. The finite difference beam propagation method (FD-BPM) with transparent boundary condition (TBC) is a robust approach to numerically deal with optical field propagations in waveguides.

In a fiber array arranged in triangular lattices, new vortices vary with respect to the propagation distance and the number of cores in the fiber array for both linear and nonlinear regimes. With more cores and longer propagation distances, more vortices are created. However, they do not always survive and may disappear while other new vortices are formed at other points.

In a linear triangular lattice, the results demonstrated that the number of vortices may increase or decrease with respect to the number of cores in the array lattice. In a nonlinear triangular lattice, however, the number of vortices tends to increase as the core radius increases and decrease as the distance between cores increases. Investigations revealed that new vortices are generated due to the effects of the phase spiral around the new points of zero intensity. These points are formed due to the mode coupling of the optical field between the cores inside the array.

In order to understand the dynamics of vortex generation, we examine vortex density, defined as the total number of vortices per unit area of the fiber array. This parameter is to be explored versus the propagation distance, the core radius size and the distance between cores. The Shack-Hartmann wavefront sensor can be employed to find the vortex density and the locations of vortices. Simulation results revealed that the vortex density increases with respect to propagation distance until saturation. It also increases with an increasing radius size but decreases with increasing distance between the array cores for linear and nonlinear regimes.

iv

To my family

Acknowledgment

I would like to express my sincere recognition and appreciation to those who provided encouragement and advice during this research.

- Prof Chiu-Tai Law for his outstanding comments, assistance and support of the area of study and field of research.

- Prof Arash Mafi, Prof Mahsa Ranji, Prof Hossein Hosseini and Prof Rani El-Hajjar for their valuable guidance as members of the committee.

- The Department of Electrical Engineering for making all possible efforts in preparing laboratories, tools and computer systems.

- The University of Wisconsin - Milwaukee Library for making all necessary references achievable and available.

- Members of my family for their love, care, understanding and enormous help throughout this serious effort.

Without all of them, I would not be able to even consider completion of this dissertation research.

Contents

List of Figures

List of Tables

Chapter 1   Introduction

Optical fibers form the most important component in modern telecommunications and data technology systems due to their high channel capacity and enhanced signal to noise ratio. Laser is the primary light source due to its Gaussian profile and nearly monochromatic features. Engineers have recently started to investigate and study the propagation of optical vortices in linear and nonlinear materials for possible future applications in sensing, frequency mixing and modulations. In this chapter, we review the significant works published in this field of study and also present our research investigation and analysis methodology.

1.1   Literature review

In 1992, optical vortex solitons were experimentally observed in a bulk self-defocusing Kerr nonlinear medium [1]. The wave was stationary and stable with a size that inversely depends on the background field strength and located at the axis of a 2π helical phase ramp. Pairs with opposite topological charge were also experimentally and numerically examined by a convective Kelvin-Helmholtz instability of dark soliton stripes [1].

The decay of dark soliton stripes to optical vortex solitons was investigated in 1993 by C. Law and G. Swartzlander under long-period transverse modulation [2]. Numerical techniques were applied to perform nonlinear stability analysis to explore the nonlinear dynamics of that process. Investigations were also adjusted for verification by experiments by numerically determining the distance where soliton stripes transform into

vortex pairs [2].

F. Ruox investigated the dynamical behavior of optical vortices propagating as an electromagnetic wave by scalar diffraction theory [3]. It was observed that a single optical vortex propagates perpendicularly to the wave front. Two optical vortices with the same charges were observed to gyrate around each other during propagation. Conversely, two optical vortices with opposite charges were observed to drift perpendicular to the direction of propagation. An elementary model for the propagation of vortex pairs was then proposed to explain the gyration and drift phenomena [3].

Vortex soliton motion and steering were later examined by J. Christou et al. in 1996 [4]. The steering of an optical vortex soliton by the superposition of a weak coherent background field was presented by experiments. To account for vortex motion, a model was derived and verified both experimentally and numerically [4].

Propagation dynamics of optical vortices were also studied by D. Rozas et al. in 1997 [5]. The authors stated that optical vortices in linear or nonlinear media display propagation dynamics close to hydrodynamic vortex phenomena. Analytical and numerical methods were employed to explain and investigate the interaction between vortices and the background field. It was found that optical vortices with quasi-point core functions, such as optical vortex solitons, orbit one another at rates that are orders of magnitude larger compared to those with non-localized cores [5].

In early 2000, C. Law et al. employed numerical techniques to determine the waveguide dispersion and optimal size of the guided beam [6]. Authors used the phenomenon that an optical vortex soliton propagating in a self-defocusing nonlinear optical medium induces a graded-index waveguide [6].

Linear and nonlinear waveguides induced by optical vortex solitons were investigated by A. Carlsson et al. in 2000 [7]. The study was done both numerically and analytically for linear and nonlinear waveguides induced by optical vortex solitons in a Kerr medium. Both fundamental and first-order guided modes were discussed in addition to other occurrences of effective defocusing and focusing nonlinearity [7].

A notable research study about the vortex trajectories was published in July 2000 by I. Freund [8]. Specific rules were formulated that limit relations between optical vortex trajectories on a given manifold. Possible topologies for these trajectories were also considered and discussed [8].

In 2003, J. Curtis and D. Grier explained that single-beam optical gradient force traps created by focusing helical modes of light are known as optical vortices [9]. They also discussed that the modulation of the helical pitch may yield a new class of optical traps. These are dynamically reconfigurable intensity distributions that may provide new opportunities for controlling motion in mesoscopic systems. The authors described the implementation of modulated vortices based on the holographic tweezer technique [9].

Optical vortices evolving from helicoidal integer and fractional phase steps were presented in 2004 by M. Berry [10]. The evolution of a wave with unit amplitude and a phase step 2π on the positive x axis was studied exactly and paraxially. For integer steps, the singularity at the origin becomes an optical vortex but far from the axis the wave is a diffracted wave [10]. For fractional steps, no fractional strength vortices can propagate but the interference between an extra diffracted wave and the scattered wave generates a pattern of vortex lines [10].

F. Flossmann and others have calculated, in 2005, the propagation dynamics of an

initial off-axis vortex with topological charge +1 in Laguerre-Gaussian background beams [11]. The intention was to investigate the propagation dynamics of optical vortices in that background. Initially, a vortex with a broad core was embedded in the background beam, the dislocation surfaces were destroyed during propagation and two vortices with opposite charge were created per dislocation surface in planes perpendicular to the propagation direction [11]. For a vortex with a narrow core, diffraction led to the birth of more than two vortices per dislocation surface. The authors also experimentally demonstrated vortex propagation and showed excellent agreement with the calculated intensity distributions [11].

When optical beams are united, optical vortices generically arise. J. Leach and others reported, in 2005, how several laser beams containing optical vortices could be combined to form optical vortex loops, links and knots embedded in a light beam [12]. They also described the experiments where vortex loops form these structures following a theoretical model originally proposed. In addition, the beams were synthesized using a programmable spatial light modulator and imaged using a CCD camera [12].

Propagation of optical vortices in coiled weakly guiding optical fibers was then examined in 2007 by K. Alekseyev and M. Yavorsky [13]. The structure of modes of regularly coiled weakly guiding optical fibers with a round cross section was determined. The modes were shown to be represented by two right- and left-hand polarized stable optical vortices [13]. In addition, the parameters for optimal coiling at which the transmission of vortices along the fibers was the most stable with respect to fiber perturbations were determined [13].

In early 2008, the propagation of vortex beams through weak-to-strong atmospheric

turbulence was simulated and analyzed by G. Gbur and R. Tyson [14]. It was demonstrated that the topological charge of such a beam is a robust quantity that can be used as an information carrier in optical communications. The advantages and limitations of such an approach were discussed [14].

C. Ke and others investigated composite optical vortices in non-collinear Laguerre-Gaussian beams and their propagation in free space in 2008 [15]. With two Laguerre-Gaussian beams, they investigated the composite optical vortices formed by two non-collinear Laguerre-Gaussian beams with different phases, amplitudes, waist widths, off-axis distances and their propagation in free space. The motion, creation and annihilation of composite vortices occurred in the free-space propagation and the net charge during the propagation were found to be unchanged [15].

Both propagation and diffraction of optical vortices (Laguerre-Gaussian beams) traversing a circular obstacle and Young's double slit were then studied by P. Fischer and others in 2008 [16]. Using Young's double slits, the authors measured the azimuthal index of the vortex beam even for polychromatic vortices generated by broadband supercontinuum radiation [16].

Optical vortices in self-focusing Kerr nonlinear media were additionally investigated in 2009 by P. Hansinger et al. [17]. The interactions of optical vortices in self-defocusing and self-focusing Kerr nonlinear media were compared numerically. Results showed that the interaction of two and three vortices with equal and alternative topological charges were the same in both media. However, the vortex dynamics under self-focusing conditions was influenced by the reshaping of the background [17].

Experimentally, Y. Zhang and others examined the modulated vortex solitons of

four-wave mixing in 2010 [18]. They demonstrated the vortex solitons of four-wave mixing in multi-level atomic media created by the interference patterns with superposing three or more waves. The modulation effect of the vortex solitons was also induced by the cross-Kerr nonlinear dispersion due to atomic coherence in the multi-level atomic system [18].

In late 2010, H. Dai et al. discussed the propagation dynamics of an optical vortex imposed on an Airy beam [19]. The general propagation dynamics of an Airy beam carrying unit phase singularity was demonstrated. For the optical vortex with a unit charge, theoretical analysis indicated that it was propagated along the parabolic trajectory. The acceleration velocity was twice as fast as conventional Airy beams before a critical position [19].

S. Vedad and A. Heidari presented, in 2012, an analytical and numerical investigation of the optical vortex solitons by a computational study [20]. They discussed the possibility of forming spatiotemporal vortex solitons in the dispersive inhomogeneous non-linear optical fibers using a graded-index Kerr medium [20]. They also used a variation approach to solve the multidimensional inhomogeneous non-linear Schrodinger Equation and showed that spatiotemporal vortex solitons can be stabilized under certain conditions [20].

In 2012, C. Alexeyev discussed the possibility of optical vortices in twisted anisotropic and elliptical fibers with respect to external perturbations independent on longitudinal coordinates [21]. They showed that the topological charge in twisted elliptical and anisotropic fibers proved to be robust with respect to induced material anisotropy [21]. By contrast, optical vortices and topological charges were unstable with

respect to induced z-independent ellipticity of the transverse cross-section of the fiber. In this case, optical vortices were found to invert their initial topological charge with propagation [21].

The effect of spatial coherence on determining the topological charge of a vortex beam was investigated in 2012 by C. Zhao and others [22]. It is possible to determine the topological charge of a vortex beam based on the Fourier transform of its intensity. Based on that finding, the authors demonstrated both theoretically and experimentally that this method was invalid for determining the topological charge of a vortex beam with low coherence. Furthermore, they proposed a method to determine the topological charge of a vortex beam with low coherence based on its complex degree of coherence [22].

P. Vaity and R. Singh discussed the topological charge dependent propagation of optical vortices under quadratic phase transformation in 2012 [23]. The authors made optical vortices of different topological charge and diffracted them through a quadratic phase mask using a spatial light modulator. This phase mask showed the diffraction in which the positive diffracted order performed different dynamics than the negative diffracted order [23]. The diffraction pattern and its orientation were found dependent on the charge of the vortex and its sign. The experimental results were verified and compared with exact analytical results with acceptable agreements [23].

In late 2012, J. Demas et al. studied the possibility of sensing with optical vortices in photonic-crystal fibers [24]. The authors demonstrated optical polarization vortex generation in a photonic-crystal fiber by a CO_2 laser long period grating. Vortices were a special subclass of fiber modes that result in polarization-insensitive resonances even when grating perturbations were asymmetric [24]. The physics of vortex generation

combined with the use of structural perturbations alone in single-material fibers opened up a new schematic for realizing harsh-environment sensors. The authors showed that the temperature and polarization stability of vortex devices was maintained for prolonged periods of time at temperatures exceeding 1000°C [24].

Investigations about the propagation of a Lorentz-Gauss vortex beam through a paraxial ABCD optical system were described by Y. Ni and G. Zhou in 2013 [25]. An analytical expression of a general Lorentz–Gauss vortex beam passing through a paraxial ABCD optical system was derived. Numerically, the normalized intensity distribution, the phase distribution and the orbital angular momentum density distribution of Lorentz-Gauss vortex beams propagating in free space were graphically demonstrated [25]. The influences of Gaussian waist, the width parameters of Lorentzian part, the topological charge on the normalized intensity distribution, the phase distribution and the orbital angular momentum density distribution of Lorentz–Gauss vortex beams propagating in free space were discussed in detail [25].

Also in 2013, the propagation of an Airy vortex beam in uniaxial crystals was explained by D. Deng and others [26]. The propagation dynamics of an Airy beam superimposed with a unit topological charge optical vortex was investigated. The study showed analytical and numerical details in uniaxial crystals orthogonal to the optical axis [26]. Upon propagation, the Airy vortex beam was mainly dependent on the ratio of the extraordinary refractive index to the ordinary refractive index [26]. Due to the anisotropic effect of the crystals, the acceleration was more rapid with an Airy vortex beam in the transversal direction along the optical axis compared to that in the other transversal direction [26].

By means of several computer simulations, X. Li et al. explained the propagation properties of optical vortices in a random speckle field based on the Fresnel diffraction scheme in 2013 [27]. Furthermore, vortex distribution, phase distribution and the zero-crossing lines of the real and imaginary parts of the optical field were analyzed comparatively in 2D space [27]. The evolution of optical vortices was studied along propagation direction and the relation between vortex density and the distance was analyzed [27].

In another 2013 study, P. Jia and others investigated the sidelobe-modulated optical vortices for free-space communication [28]. The authors proposed and experimentally demonstrated a new type of free-space optical communication method. The transmitter encodes data into a composite computer-generated hologram which the receiver then decodes through a retrieved array of sidelobe-modulated optical vortices [28]. By employing this generation and detection technique, the usual stringent alignment and phase-matching requirement of the detection of optical vortices was released. Due to the orbital angular momentum multiplexing and spatial paralleling, this communication method possessed the ability to greatly increase the capacity of data transmission [28].

Analytical and numerical investigations for the propagation of a stationary pulse were discussed in 1995 by A. Buryak and N. Akhmediev [29]. The fiber arrays were assumed to be nonlinear in a circular symmetry which showed many types of stationary pulse-like stationary waves [29].

In 2003, J. Yang and Z. Musslimani reported the existence of fundamental and vortex solitons in two-dimensional optically induced waveguide arrays [30]. They found that fundamental solitons are largely confined to one lattice site in the strong localization

regime. However, fundamental and vortex solitons were spread over many lattices in the strong localization regime [30].

T. Alexander et al. revealed, in 2004, the existence of asymmetric vortex solitons in ideally symmetric periodic lattices [31]. Asymmetric vortex solitons are expected to exist in different nonlinear lattice systems [31].

The observation of discrete vortex solitons in optically induced photonic lattices was presented in 2004 by D. Neshev et al. [32]. This investigation was experimentally completed and demonstrated strong stabilization by the lattice in a self-focusing nonlinear medium [32].

In 2005, C. Chen et al. performed a number of experiments on Gaussian beams and vortices in optically induced photonic lattices [33]. They investigated the vortex-lattice interactions in a nonlinear medium and observed lattice twisting due to transfer of the angular momentum carried by the vortex beam [33].

The dynamics of vector solitons and vortices in two-dimensional photonic lattices were investigated by M. Rodas-Verde et al. in 2006 [34]. Discrete vortex solitons were studied with Kerr nonlinearity charge flipping instability. They discussed novel types of stable, incoherently coupled dipoles and vortex-soliton complexes that can be excited by Gaussian beams [34].

In 2008, B. Terhalle et al. observed multi-vortex solitons in photonic lattices [35]. These were topologically stable and spatially localized in optically induced hexagonal lattices. Experimental results confirmed numerical simulations for the propagation of beams in weakly deformed lattice potentials [35].

Moreover, B. Terhalle et al., in 2009, performed experimental investigations to

examine double-charge discrete vortex solitons in hexagonal lattices [36]. Vortices were found to be stable and induced in self-focusing nonlinear media where single-charge vortex solitons are unstable [36].

In 2009, K. Law and P. Kevrekidis studied the stable properties of higher-charge discrete vortices in hexagonal optical lattices [37]. They found that double-charge discrete vortices may be completely stable whereas single-charge vortices may exhibit some dynamical instability [37].

Laboratory experiments are carried out in 2010 by K. Murphy et al. to detect optical vortices using a Shack-Hartmann wavefront sensor to measure the slopes of the wavefront surface [38]. The use of the slope technique greatly improved the detection rate of vortices in an experimental setup [38].

In 2012, C. Huang et al. proposed a method for realizing high-spatial-resolution detection of singularity points in optical vortex beams [39]. Using a Shack–Hartmann wavefront sensor, the position of an optical vortex can be determined [39]. Optical experiments were also carried out to verify the proposed method. The results showed good linearity in detecting the position of singularity points [39].

B. Stoklasa et al. in 2014 showed that the Shack–Hartmann wavefront sensor can be instrumental in reconstructing the complete coherence properties of the signal [40]. They confirmed the calculations with an experimental characterization of partially coherent vortex beams and achieved excellent results [40].

1.2   Research methodology

The research is mainly based on the beam propagation method (BPM) which is a

numerical technique in electromagnetics suitable for examining the spread of light in optical waveguides such as single mode or multimode fibers [41]. Mathematical analysis starts with the Maxwell's Equations and the Helmholtz scalar wave Equation with a paraxial electric field in the form [41]:

$$E(x, y, z) = \phi(x, y, z)e^{-jk_0 n_0 z} \tag{1.1}$$

where, $\phi(x,y,z)$ is a slowly varying complex envelope as a function of position.

The substitution of Equation (1.1) in the wave Equation leads to the derivation of the (2+1)D paraxial Helmholtz Equation or the Schrodinger Equation in the form [42]:

$$\nabla_t^2 \phi - 2jk_0 n_0 \frac{\partial \phi}{\partial z} + k_0^2 (n^2 - n_0^2)\phi = 0 \tag{1.2}$$

where, $\nabla_t^2 = \partial^2/\partial x^2 + \partial^2/\partial y^2$, k_0 and n_0 are the free space wave number and the reference refractive index respectively and n is the refractive index of the medium.

Numerically, the finite difference method is employed to solve Equation (1.2) using the Crank-Nicholson technique for better stability [42]. FORTRAN is the programming language used for coding and executing simulations. GNUPLOT is employed to generate images. In addition, a number of videos are generated for the intensity and phase of the propagating fields based on HDF (Hierarchical Data Format) images.

1.3   Main objectives

The major objectives to be investigated analytically and numerically in this research work are focused on three main goals:

- The study of propagation dynamics of an optical vortex in an optical fiber of certain lengths and sizes. The intention is to find possible changes to the

optical vortex features as it propagates inside these types of optical fibers.

- To achieve the former objective, we investigate the propagation dynamics of an optical vortex in optical fiber arrays of triangular lattices with numerical simulations using various indices of refraction in the core region. Our research aims to look for any alterations in vortex dynamics owing to fiber structures.

- Investigate the propagation of an optical vortex in nonlinear triangular lattices with cores of different arrangements.

In order to achieve these goals, FORTRAN simulation codes have been developed. Output data have been generated with GNUPLOT in various formats including ASCII data for complex field and images stored in HDF (Hierarchical Data Format). The image data have been used to provide videos for visualization of vortex dynamics.

Chapter Two presents the beam propagation method (BPM) used in simulations along with the representation of the optical vortex. Chapter Three discusses the solution of the BPM by finite difference and explains the matrix Equations in addition to the transparent boundary condition (TBC) used in the analysis. Chapter Four presents several simulations for the hexagonal fiber array. It also discusses analytical solutions by coupled mode theory and describes the detection of a vortex field. Next, Chapter Five presents investigations for the triangular lattice and discusses the results of several statistical analyses. Finally, Chapter Six investigates the implementation and application of the fiber lattice with an optical vortex as a sensor using the Shack-Hartmann wavefront sensor.

Chapter 2   Wave Propagation Analyses

Propagation analysis in optical waveguides is of crucial importance in understanding any possible changes to the features and characteristics of light. The most common analytical tool employed by the research community and used in studying the propagation dynamics of light in optical fibers is the beam propagation method. In this chapter, we present this numerical method with its fundamental Equations and then explain the mathematical representation of an optical vortex used in our research.

2.1   The beam propagation method

The beam propagation method (BPM) is a numerical technique used primarily in computational electromagnetics to solve for the propagation of light in optical waveguides under slowly varying envelope approximations [41]. The method usually gives acceptable results in linear and nonlinear media for relatively small longitudinal step size in the direction of propagation in axially varying waveguides [42, 43]. It is widely employed to investigate the analysis and design of different photonic devices such as the inhomogeneous and anisotropic liquid crystals [44].

Several important improvements are introduced to the BPM to enhance the speed of calculations and to reduce generated errors. Diagonalization of the Hermitian operator is proposed to enhance the accuracy of paraxial approximations [45]. In addition, a wide angle finite element scheme for TE and TM mode propagations is used to model step index and bidirectional waveguides with periodic structures with good accuracy [46].

In more recent studies, a 3D full vectorial propagation method with Fourier basis functions in the transverse direction has achieved good accuracy even for complex waveguides [47,48]. In order to speed up the conventional calculations, a BPM in matrix form based on Fourier cosine series or expansions in the azimuthal direction and non-paraxial propagating beams that simplify 3D problems to 2D only has been demonstrated with comparable correctness [49,50,51].

Formulation of the BPM starts with the Maxwell's Equations in a source-free and charge-free medium:

$$\nabla \times \vec{e} = -\mu \frac{\partial \vec{h}}{\partial t} \Leftrightarrow \nabla \times \vec{E} = -j\omega\mu\vec{H}$$

$$\nabla \times \vec{h} = \varepsilon \frac{\partial \vec{e}}{\partial t} \Leftrightarrow \nabla \times \vec{H} = j\omega\varepsilon\vec{E} \qquad (2.1)$$

$$\nabla \cdot \varepsilon\vec{E} = 0$$

$$\nabla \cdot \mu\vec{H} = 0$$

where $j = \sqrt{-1}$, $\omega = 2\pi f$ and f is the frequency, ε and μ are the electric permittivity in F/m and magnetic permeability in H/m respectively, $\vec{e}$ is the time varying electric field intensity vector in V/m and $\vec{h}$ is the time varying magnetic field intensity vector in A/m. Also, $\vec{E}$ and $\vec{H}$ are the electric and magnetic field complex amplitude vectors such that $\vec{e} = \text{Re}\{\vec{E}\exp(j\omega t)\}$ and $\vec{h} = \text{Re}\{\vec{H}\exp(j\omega t)\}$ respectively [42,52].

By taking the curl of the first two Equations in (2.1) and using the relation $\nabla \times \nabla \times \vec{A} = \nabla(\nabla \cdot \vec{A}) - \nabla^2\vec{A}$ for any vector $\vec{A}$ with $\nabla(\nabla \cdot \vec{A}) = 0$, we obtain the Helmholtz scalar wave Equation in frequency domain as [53]:

$$\nabla^2\psi + k_0^2 n^2\psi = 0 \qquad (2.2)$$

where ψ is E_x, E_y, E_z, H_x, H_y or H_z and $k = k_0 n = 2\pi/\lambda$ is the wave number, λ is the

wavelength and n is the refractive index of the medium.

The optical field ψ can be expressed as [54]:

$$\psi = \phi(x, y, z)e^{-jk_0 n_0 z} \tag{2.3}$$

where $\phi(x,y,z)$ is a paraxial slowly varying envelope and $e^{-jk_0 n_0 z}$ is a rapidly varying part for the propagation of a carrier in the substrate or cladding of the optical waveguide with n_0 refractive index. Substituting Equation (2.3) into Equation (2.2) and assuming $\partial^2\phi/\partial z^2 \approx 0$ we get:

$$\frac{\partial\phi}{\partial z} = \frac{-j}{2k_0 n_0}\nabla_t^2\phi - \frac{j}{2n_0}k_0(n^2 - n_0^2)\phi \tag{2.4}$$

where $\nabla_t^2 = \partial^2/\partial x^2 + \partial^2/\partial y^2$ is the transverse Laplacian. This is the paraxial Helmholtz Equation or the Schrodinger Equation in (2+1)D. Both terms on the right side of Equation (2.4) affect the propagation of light simultaneously. The first term with ∇_t^2 represents the diffraction of light and the second term is the potential function set up by a waveguide or a nonlinear medium with n refractive index that allows the interaction of a material or device with the wave [55].

Equation (2.4) can better be expressed in normalized form as a function of (X,Y,Z) defined as X=x/w_0, Y=y/w_0 and Z=z/z_0 where w_0 is the waist radius and $2z_0=2\pi w_0^2/\lambda$ is the depth of focus. In free space where $n=n_0$, Equation (2.4) in normalized form is [56]:

$$\nabla_T^2\Phi - j4\frac{\partial\Phi}{\partial Z} = 0 \tag{2.5}$$

where $\nabla_T^2 = \partial^2/\partial X^2 + \partial^2/\partial Y^2$ and $\Phi(X,Y,Z)$ is the normalized paraxial slowly varying envelope as a function of position. One of the analytical solutions of Equation (2.5) is the Gaussian field as a function of X and Y in the transverse direction and Z in the

longitudinal direction as:

$$\Phi = \frac{1}{1-jZ} e^{-\left(\frac{X^2+Y^2}{1-jZ}\right)} \tag{2.6}$$

Similar to Equation (2.5), the normalized Schrodinger Equation or paraxial Helmholtz Equation in inhomogeneous medium is [57]:

$$\nabla_T^2 \Phi - j4\frac{\partial \Phi}{\partial Z} + k_0^2 w_0^2 \left(n^2 - n_0^2\right)\Phi = 0 \tag{2.7}$$

where the refractive index n of the medium is a function of position as $n(X,Y)$.

If a high intensity optical beam propagates in a waveguide, the refractive index of the medium changes as a function of intensity, i.e. nonlinear effects. In a nonlinear medium where the refractive index of the medium is a function of intensity as $n(I)$, the Schrodinger Equation is nonlinear and can be expressed in as [58,59]:

$$\frac{\partial \phi}{\partial z} = \frac{-j}{2k_0 n_0}\nabla_t^2 \phi - \frac{j}{2n_0}k_0\left(n^2(I) - n_0^2\right)\phi \tag{2.8}$$

where $n(I)=n+n_2 I$, n_2 is the optical Kerr coefficient for a Kerr nonlinear medium, I is the intensity as $I=|\phi|^2/2\eta$ and η is the characteristic impedance. The expression $n^2(I)-n_0^2$ is estimated as $n^2(I)-n_0^2 \approx n^2 n_2 |\phi|^2 / \eta_0$ where η_0 is the characteristic impedance in free space as 120π ohms. Equation (2.8) is normalized as [60]:

$$\nabla_T^2 \Phi - j4\frac{\partial \Phi}{\partial Z} + \frac{w_0^2 n_2 k^2 I_0}{\eta_0}|\Phi|^2 \Phi = 0 \tag{2.9}$$

where I_0 is the peak intensity.

Equation (2.9) is the normalized nonlinear Schrodinger Equation that represents the propagation of light in an optical waveguide and is solved by BPM in this dissertation. An analytical solution for this Equation does not exist but it can be solved numerically

for given boundary conditions [61,62].

2.2 Vortex representation

An optical vortex is defined as a point of zero intensity with a spiral phase change from 0 to 2π around it along the direction of propagation [63,64]. Mathematically, the optical vortex can be expressed as a Laguerre-Gaussian mode of the first order given by [3]:

$$U(\rho,\phi,z) = A\frac{w_0}{w^2}\rho e^{\frac{-\rho^2}{w^2}} e^{-jkz-jk\frac{\rho^2}{2R}-j\phi-2j\zeta} \tag{2.10}$$
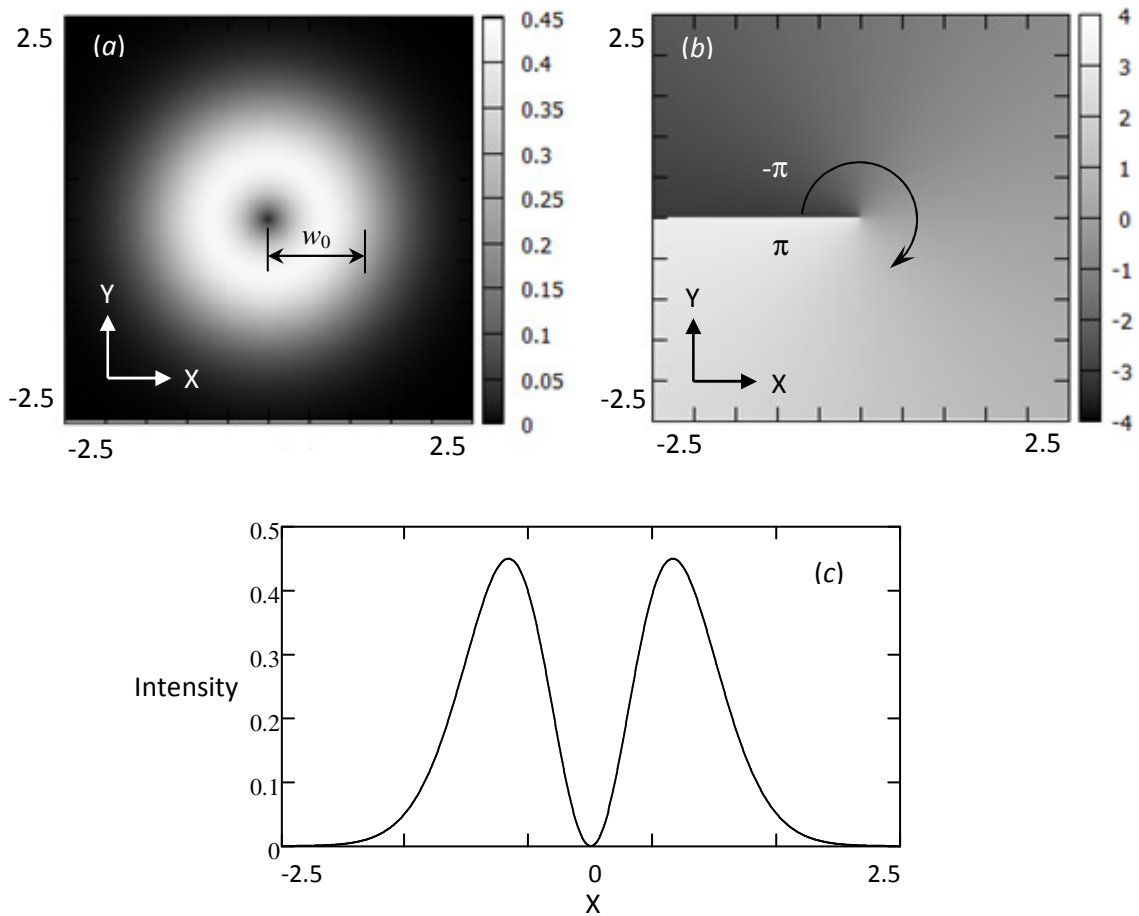
Figure 1 Intensity (*a*), phase (*b*) and intensity at Y=0 (*c*) of an optical vortex.

where $U(\rho,\phi,z)$ is the vortex optical field, A is a constant, $\rho^2=x^2+y^2$, $w^2=w_0^2[1+(z/z_0)^2]$ and w is the beam width, w_0 is the waist radius, $R=z[1+(z_0/z)^2]$ is the radius of curvature, $\phi=\tan^{-1}y/x$, $\zeta=\tan^{-1}z/z_0$, $2z_0=2\pi w_0^2/\lambda$ is the depth of focus, λ is the wavelength and $k=2\pi/\lambda$ is the wave number [5].
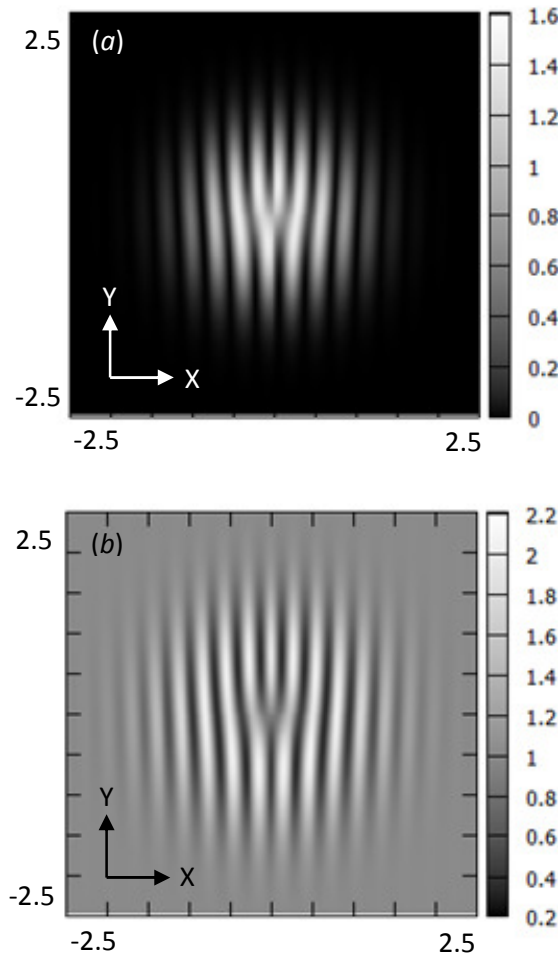
Figure 2 Interference of a vortex with a Gaussian wave (*a*) and a plane wave (*b*).

Figure 1 illustrates an optical vortex calculated with Equation (2.10) at $z=0$ for $w_0=5.0\mu m$ and $\lambda=1.0\mu m$ under a normalized $X=x/w_0$ and $Y=y/w_0$ coordinates with a transverse resolution step of $\Delta=\Delta X=\Delta Y=0.01$. In Figure 1(*a*), the vortex intensity in the

transverse X and Y is shown as a round region of light with its zero intensity point at the center. The vortex phase is plotted in Figure 1(*b*) which demonstrates its change from -π to π around the zero intensity point and along the direction of propagation. At Y=0, the intensity is shown in Figure 1(*c*) with its point of zero intensity at X=0.

The interference of an optical vortex with either a Gaussian wave or a plane wave generates a very clear dislocation in the interference fringes indicating the existence of a zero point optical field. This technique is used to detect any changes that may occur to a propagating optical vortex and provide a clear and obvious method for vortex detection in contrast to intensity measurements [11].

Figures 2(*a*) and 2(*b*) show the interferogram of an optical vortex with a Gaussian wave and a plane wave references respectively at z=0 for w_0=5.0μm, λ=1.0μm with a transverse normalized resolution of Δ=ΔX=ΔY=0.01. The dislocation point at the center in both Figures signifies the location of the optical vortex.

Chapter 3   Numerical Solutions

Simulation of field propagation in optical waveguides based on the beam propagation method is a vital part in our research. Analyses start by defining the numerical method used for solving the partial differential Equations and techniques employed to reach a formulation suitable for coding. In this chapter, we present the finite difference method and its matrix representation. In addition, the general solution structure is discussed and the arrangements of the generated numerical data are shown which signify the shape of the output field image.

3.1   Finite difference method

Here, we start with the (2+1)D normalized linear Schrodinger Equation (2.5) in free space as [65]:

$$\frac{\partial \Phi}{\partial Z} = -\frac{j}{4}\left(\frac{\partial^2}{\partial X^2} + \frac{\partial^2}{\partial Y^2}\right)\Phi = L\Phi \tag{3.1}$$

where L is a normalized differential operator on $\Phi(X,Y,Z)$.

The Crank-Nicholson technique implies a stable formal solution of the form:

$$\Phi(X,Y,Z+\Delta Z) = \Phi(X,Y,Z)e^{L\Delta Z} \tag{3.2}$$

where ΔZ is the longitudinal step in the direction of propagation. This is unconditionally stable for small values of ΔZ [66].

The exponential part can be approximated as:

$$e^{L\Delta Z} \approx 1 + L\Delta Z = 1 - \frac{j}{4}\left(\frac{\partial^2}{\partial X^2} + \frac{\partial^2}{\partial Y^2}\right)\Delta Z \tag{3.3}$$

By employing the discrete steps of $X=X_m=m\Delta X$, $Y=Y_p=p\Delta Y$ and $Z=Z_q=q\Delta Z$ in Equation (3.1) and using Equation (3.2) we get:

$$\Phi_{m,p}^{q+1} = e^{L\Delta Z}\Phi_{m,p}^{q} \tag{3.4}$$

Equation (3.4) states that the transverse distribution of the field as a function of m and p at a longitudinal $q+1$ step can be obtained based on the transverse distribution of the field as a function of m and p at a longitudinal q step previously defined. The exponent employs the differential operator L in Equation (3.3) for very small values of ΔZ. Multiplying both sides of Equation (3.4) by $e^{-L\,\Delta Z/2}$ and using Equation (3.3) we get:

$$\left[1 + \frac{j\Delta Z}{8}\left(\frac{\partial^2}{\partial X^2} + \frac{\partial^2}{\partial Y^2}\right)\right]\Phi_{m,p}^{q+1} = \\ \left[1 - \frac{j\Delta Z}{8}\left(\frac{\partial^2}{\partial X^2} + \frac{\partial^2}{\partial Y^2}\right)\right]\Phi_{m,p}^{q} \tag{3.5}$$

Equation (3.5) forms the basic numerical solution for our problem employing the unconditional stability of the Crank-Nicholson technique. However, it is difficult to deal with numerically due to the two dimensional nature of the differential operators. In order to overcome this difficulty, we split them into two one dimensional operators (one for X direction and another for Y direction) and then implement them in matrix forms [67].

3.1.1   Split Equations

For any functions $f(x)$ and $g(y)$, the finite difference representation for the second order derivatives are defined as:

$$\frac{\partial^2 f(x)}{\partial x^2} = \frac{1}{(\Delta x)^2}\left[f(x+\Delta x) - 2f(x) + f(x-\Delta x)\right] = F \qquad (3.6a)$$

$$\frac{\partial^2 g(x)}{\partial y^2} = \frac{1}{(\Delta y)^2}\left[g(y+\Delta y) - 2g(y) + g(y-\Delta y)\right] = G \qquad (3.6b)$$

Using the formulas in Equations (3.6) in Equation (3.5) we obtain:

$$\left[1 + \frac{j}{8}(F+G)\Delta Z\right]\Phi_{m,p}^{q+1} = \left[1 - \frac{j}{8}(F+G)\Delta Z\right]\Phi_{m,p}^{q} \qquad (3.7)$$

where *F* and *G* are the normalized central difference operators defined in Equations (3.6*a*) and (3.6*b*) [68].

Equation (3.7) is the primary finite difference Equation used to update the original field Φ(*m*,*p*,*q*) on the transverse frame by a step of ΔZ to the field Φ(*m*,*p*,*q*+1). The basic structure of the numerical solution is to express Equation (3.7) in a matrix Equation and solve linear algebraic Equations to find Φ(*m*,*p*,*q*+1). The most numerically intense operation in Equation (3.7) is that both *F* and *G* operators are applied on the field simultaneously as a two dimensional process.

A better manageable solution is to split these operators and only perform a single operator in one direction, either *F* or *G*, at each step in sequence. In that situation, two Equations are generated each with only one difference operator applied on the field instead of one Equation with two simultaneous operators as in Equation (3.7). The split *F* and *G* formulation starts by approximating Equation (3.7) as:

$$\left[1 + \frac{j}{8}F\Delta Z\right]\left[1 + \frac{j}{8}G\Delta Z\right]\Phi_{m,p}^{q+1}$$
$$= \left[1 - \frac{j}{8}F\Delta Z\right]\left[1 - \frac{j}{8}G\Delta Z\right]\Phi_{m,p}^{q} \qquad (3.8)$$

A new operator *U* is then defined such that:

$$\Phi_{m,p}^{q+1} = U\Phi_{m,p}^{q} \tag{3.9}$$

where U is expressed as:

$$U = \left[\frac{1-\dfrac{j}{8}G\Delta Z}{1+\dfrac{j}{8}F\Delta Z}\right]\left[\frac{1-\dfrac{j}{8}F\Delta Z}{1+\dfrac{j}{8}G\Delta Z}\right] \tag{3.10}$$

Using Equation (3.10), Equation (3.9) can be split into two Equations as:

$$\left[1+\frac{j}{8}F\Delta Z\right]\Phi^{*}{}_{m,p}^{q} = \left[1-\frac{j}{8}G\Delta Z\right]\Phi_{m,p}^{q} \tag{3.11a}$$

$$\left[1+\frac{j}{8}G\Delta Z\right]\Phi_{m,p}^{q+1} = \left[1-\frac{j}{8}F\Delta Z\right]\Phi^{*}{}_{m,p}^{q} \tag{3.11b}$$

where Φ^{*} is an intermediate field [69].

Using Equation (3.6) for the central finite difference operators F and G in Equations (3.11a) and (3.11b), we obtain the normalized finite difference solution in spilt X and Y form as:

$$\begin{aligned}
A\Phi^{*}{}_{m,p}^{q} + C\left[\Phi^{*}{}_{m+1,p}^{q} + \Phi^{*}{}_{m-1,p}^{q}\right] \\
= B\Phi_{m,p}^{q} - C\left[\Phi_{m,p+1}^{q} + \Phi_{m,p-1}^{q}\right]
\end{aligned} \tag{3.12a}$$

$$\begin{aligned}
A\Phi_{m,p}^{q+1} + C\left[\Phi_{m,p+1}^{q+1} + \Phi_{m,p-1}^{q+1}\right] \\
= B\Phi^{*}{}_{m,p}^{q} - C\left[\Phi^{*}{}_{m+1,p}^{q} + \Phi^{*}{}_{m-1,p}^{q}\right]
\end{aligned} \tag{3.12b}$$

where $A=1-\alpha$, $B=1+\alpha$, $C=\alpha/2$, $\alpha=j\Delta Z/4\Delta^{2}$ and $\Delta X=\Delta Y=\Delta$.

Equations (3.12a) and (3.12b) are the spilt X and Y form of Equation (3.7) that calculates the transverse distribution of the field in two stages. First, Φ^{*} is found using Equation (3.12a) at the same longitudinal step q at the direction of propagation based on the field from the previous step with index q. Then, Φ^{*} is employed in Equation (3.12b) to obtain the transverse distribution of the field at the next longitudinal step with index

q+1 along the direction of propagation.

3.1.2   Matrix representation

Equations (3.12*a*) and (3.12*b*) can be expressed in matrix form for numerical calculations. The left side of each Equation is a square matrix of known elements which is inverted and multiplied with the vector of known field values on the right side to obtain the vector of unknown field values. Each field vector has lower element indices *m*=1, 2, 3,....., *M* and *p*=1, 2, 3,....., *P* and an upper element index *q*=1, 2, 3,....., *Q*, where *M* and *P* are the number of sampling points on the transverse plane with *M*=*P*=*N* and *Q* is the number of longitudinal steps in Z, the direction of field propagation along the optical waveguide [70].

Matrix representation starts with Equation (3.12*a*) for *p*=1, 2, 3,....., *N* and *q*=1 in the form:

$$
\begin{pmatrix}
A & C & 0 & \cdots & 0 \\
C & A & C & \ddots & \vdots \\
0 & C & A & \ddots & 0 \\
0 & \ddots & \ddots & \ddots & C \\
0 & \cdots & 0 & C & A
\end{pmatrix}_{N\times N}
\begin{pmatrix}
\Phi^{*1}_{1,p} \\
\Phi^{*1}_{2,p} \\
\Phi^{*1}_{3,p} \\
\vdots \\
\Phi^{*1}_{N,p}
\end{pmatrix}_{N\times 1}
=
\begin{pmatrix}
B\Phi^{1}_{1,p} - C[\Phi^{1}_{1,p+1} + \Phi^{1}_{1,p-1}] \\
B\Phi^{1}_{2,p} - C[\Phi^{1}_{2,p+1} + \Phi^{1}_{2,p-1}] \\
B\Phi^{1}_{3,p} - C[\Phi^{1}_{3,p+1} + \Phi^{1}_{3,p-1}] \\
\vdots \\
B\Phi^{1}_{N,p} - C[\Phi^{1}_{N,p+1} + \Phi^{1}_{N,p-1}]
\end{pmatrix}_{N\times 1}
\qquad (3.13a)
$$

and then with Equation (3.12*b*) with *m*=1, 2, 3,....., *N* and *q*=1 in the form:

$$
\begin{pmatrix}
A & C & 0 & \cdots & 0 \\
C & A & C & \ddots & \vdots \\
0 & C & A & \ddots & 0 \\
0 & \ddots & \ddots & \ddots & C \\
0 & \cdots & 0 & C & A
\end{pmatrix}_{N\times N}
\begin{pmatrix}
\Phi^{2}_{m,1} \\
\Phi^{2}_{m,2} \\
\Phi^{2}_{m,3} \\
\vdots \\
\Phi^{2}_{m,N}
\end{pmatrix}_{N\times 1}
=
\begin{pmatrix}
B\Phi^{*1}_{m,1} - C[\Phi^{*1}_{m+1,1} + \Phi^{*1}_{m-1,1}] \\
B\Phi^{*1}_{m,2} - C[\Phi^{*1}_{m+1,2} + \Phi^{*1}_{m-1,2}] \\
B\Phi^{*1}_{m,3} - C[\Phi^{*1}_{m+1,3} + \Phi^{*1}_{m-1,3}] \\
\vdots \\
B\Phi^{*1}_{m,N} - C[\Phi^{*1}_{m+1,N} + \Phi^{*1}_{m-1,N}]
\end{pmatrix}_{N\times 1}
\qquad (3.13b)
$$

The initial field Φ^{1} in Equation (3.13*a*) is used to find the intermediate field Φ^{*1} and

then Equation (3.13*b*) is used to find the field Φ^2 after one ΔZ step in the direction of propagation. To simplify, all transverse field values in both Equations out of the computational range of *m* and *p* such as $\Phi_{0,1}^{*1}$ or $\Phi_{1,0}^{1} = 0$ are assumed to be zero [71].

```
                    ┌──────────┐
                    │  START   │
                    └────┬─────┘
                         ▼
                  ┌───────────────┐
                  │  Declarations │
                  └───────┬───────┘
                          ▼
              ┌───────────────────────┐
              │  Define Φ¹ initial field │
              └───────────┬───────────┘
                          ▼
              ┌───────────────────┐      Call
              │  Calculate Φ*q     │◄────────────┐
              └─────────┬─────────┘             │
                        ▼                        │
              ┌───────────────────┐      Call    │
              │  Calculate Φq+1    │◄────────┐   │
              └─────────┬─────────┘         │   │
         No             ▼              ┌──────────────┐
    ┌────────────◄  q=Q?               │ Tri-diagonal │
    │                   │              │  solution    │
    │                  Yes             └──────────────┘
    │                   ▼
    │         ┌───────────────────┐
    │         │     Data file     │
    │         └─────────┬─────────┘
    │                   ▼
    │             ┌──────────┐
    │             │   END    │
    │             └──────────┘
```
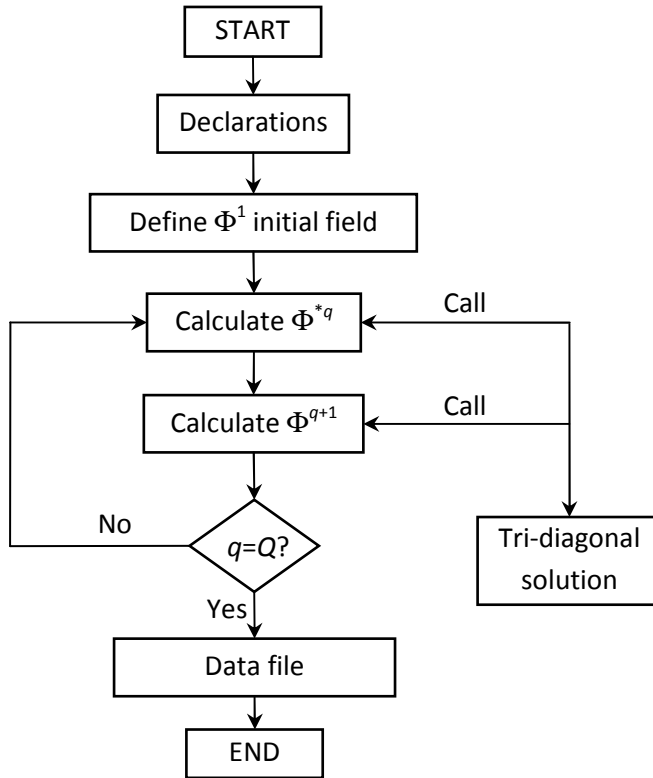
Figure 3 Basic solutions structure in a flow chart outline.

3.2 Programming and coding

The simulation program used to solve the propagating optical field is based on the matrix Equations (3.13*a*) and (3.13*b*) written in FORTRAN. Figure 3 illustrates the basic flow chart of the solution structure with the main processing functions [72].

In both Equations (3.13*a*) and (3.13*b*) we have a tri-diagonal square matrix where its

solution is coded only once as a subroutine but is called when required by the main program as shown in Figure 3. The solution for a tri-diagonal matrix Equation in the form:

$$
\begin{pmatrix}
b_1 & c_1 & 0 & \cdots & 0 \\
a_2 & b_2 & c_2 & \ddots & \vdots \\
0 & a_3 & b_3 & \ddots & 0 \\
0 & \ddots & \ddots & \ddots & c_{N-1} \\
0 & \cdots & 0 & a_N & b_N
\end{pmatrix}_{N \times N}
\begin{pmatrix}
x_1 \\
x_2 \\
x_3 \\
\vdots \\
x_N
\end{pmatrix}_{N \times 1}
=
\begin{pmatrix}
d_1 \\
d_2 \\
d_3 \\
\vdots \\
d_N
\end{pmatrix}_{N \times 1}
\tag{3.14}
$$

can be implemented easily in FORTRAN with Equation (3.14):

$$
c_i' = \begin{cases}
\dfrac{c_1}{b_1} & i = 1 \\[2ex]
\dfrac{c_i}{b_i - c_{i-1}' a_i} & i = 2,3,\ldots,n-1
\end{cases}
$$

$$
d_i' = \begin{cases}
\dfrac{d_1}{b_1} & i = 1 \\[2ex]
\dfrac{d_i - d_{i-1}' a_i}{b_i - c_{i-1}' a_i} & i = 2,3,\ldots,n
\end{cases}
\tag{3.15}
$$

$$
x_i = \begin{cases}
d_n' & i = n \\
d_i' - c_i' x_{i+1} & i = n-1, n-2,\ldots,2,1
\end{cases}
$$

GNUPLOT is used to plot and process the data in the output file [73]. The shape and arrangement of the objects on the transverse plane are shown in Figure 4. The computational area is designed in rectangular coordinates with normalized X and Y boundaries. The index of refraction is n_0 in the entire computational area except for the fiber array circular region which has a refractive index of $n(X,Y)$ at the center of the rectangular area with a normalized radius R.

The fiber core shown in Figure 4 is the numerical solution for the normalized Schrodinger Equation or paraxial Helmholtz Equation in inhomogeneous medium given in Equation (2.7). In addition to the numerical solutions presented in sections 3.1 and 3.2,

$k_0^2 w_0^2 (n^2 - n_0^2) \Phi$ is a new expression that should be included with the Equations which account for the existence of the core material with $n=n(X,Y)$.
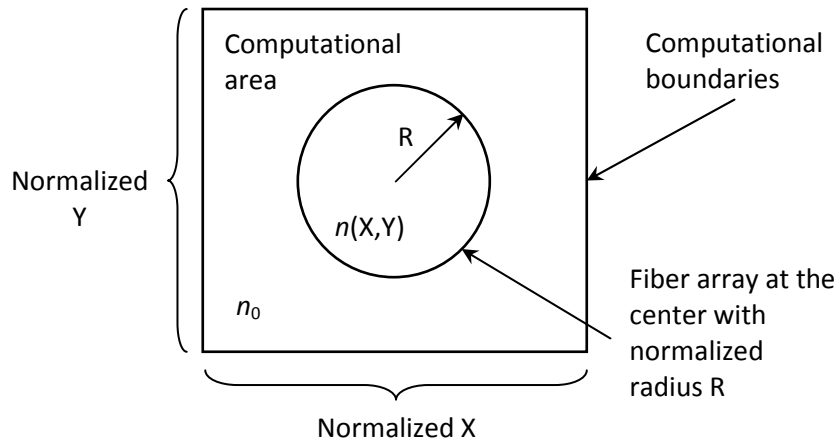
Figure 4 Image parts and arrangements.

Hence, Equations (3.12*a*) and (3.12*b*) should be modified to:

$$A\Phi^{*q}_{m,p} + C\left[\Phi^{*q}_{m+1,p} + \Phi^{*q}_{m-1,p}\right]$$
$$= B\Phi^{q}_{m,p} - C\left[\Phi^{q}_{m,p+1} + \Phi^{q}_{m,p-1}\right] \quad (3.16a)$$

$$A\Phi^{q+1}_{m,p} + C\left[\Phi^{q+1}_{m,p+1} + \Phi^{q+1}_{m,p-1}\right]$$
$$= \left\{B\Phi^{*q}_{m,p} - C\left[\Phi^{*q}_{m+1,p} + \Phi^{*q}_{m-1,p}\right]\right\}e^{-\frac{jT\Delta Z}{4}} \quad (3.16b)$$

where $T = k_0^2 w_0^2 (n^2(X,Y) - n_0^2)$ represents the inhomogeneity or nonlinearity of the fiber material and $n(X,Y)$ is the distribution of the refractive index of the core in the normalized transverse dimension.

Notice that Equations (3.12*a*) and (3.16*a*) are identical. Nevertheless, the effect of inhomogeneous core material appears only in Equation (3.16*b*). If the fiber core is only

one type of material, then $n(X,Y)=n$ as shown in Figure 4. All later derivations of the matrix Equations should include the effect of material properties by modifying T.
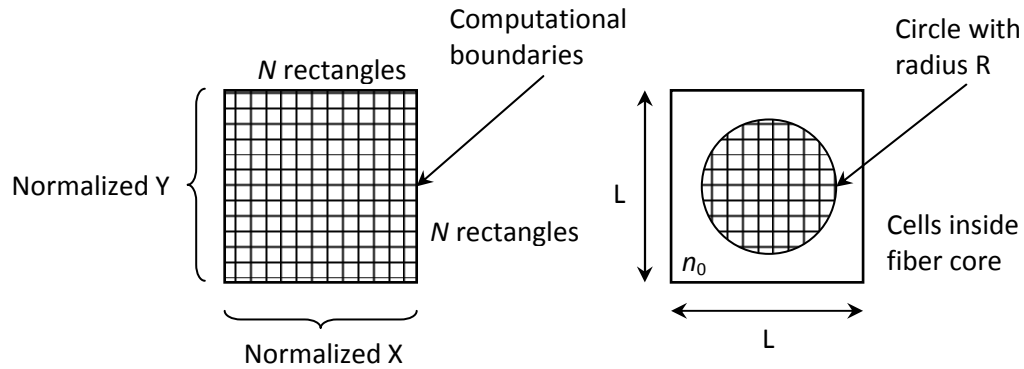
Figure 5 Meshes of $N\times N$ rectangles.

Using the same techniques, the nonlinear normalized Schrodinger Equation given in Equation (2.9) can be solved numerically and Equations (3.12a) and (3.12b) should be in the form:

$$A\Phi^{*q}_{m,p} + C\left[\Phi^{*q}_{m+1,p} + \Phi^{*q}_{m-1,p}\right] = B\Phi^{q}_{m,p} - C\left[\Phi^{q}_{m,p+1} + \Phi^{q}_{m,p-1}\right] \tag{3.17a}$$

$$A\Phi^{q+1}_{m,p} + C\left[\Phi^{q+1}_{m,p+1} + \Phi^{q+1}_{m,p-1}\right] = \left\{B\Phi^{*q}_{m,p} - C\left[\Phi^{*q}_{m+1,p} + \Phi^{*q}_{m-1,p}\right]\right\}e^{-\frac{jT\Delta Z}{4}}e^{-\frac{jS\Delta Z}{4}} \tag{3.17b}$$

where $S = I_0 k_0^2 w_0^2 n_2 \left|\Phi^{q}_{m,p}\right|^2 / \eta_0$ is the influence of the nonlinearity of the material.

The numerical distribution of the refractive index for the fibers is possible when a circle is defined with a normalized radius R with its center located at (X_c,Y_c) point. As clearly illustrated in Figure 4, all sampling points outside the circular boundary but inside

the computational area should have a refractive index of n_0=1.0. However, all other points inside the circle boundary should have $n(X,Y)$ as the refractive index of the fiber array.

The assignment of the refractive index numerical values for the randomly distributed optical fiber array is different. The technique employed is shown in Figure 5 by allocating a grid on the entire computational area with rectangular cells of normalized size D=d/w_0 where d is the actual length of the rectangular side in micrometers. For the X or Y axis normalized length L of the computational boundary, L=$N \times D$ where N is an integer and N^2 is the total number of the rectangular cells each with a normalized area of D^2 in the whole computational region as in Figure 5. The refractive index is then randomly or periodically assigned for each rectangular cell as $n=n_1$ or $n=n_2$ and the refractive index is set to n_0=1.0 for regions outside the circular boundary.

3.3 Transparent boundary condition

Optical waves examined by the beam propagation method exhibit reflections problems by the computational boundaries as revealed in Figure 4. Reflections of radiated optical waves may interact with the original propagating field corrupting final results. In order to overcome this problem, waves reaching the boundaries are assumed to be radiating out of the computational area in a plane wave form. This approximation technique is known as the transparent boundary condition (TBC) [74,75,76].

For the right boundary radiating wave, the computation of the finite difference field values in the current step are based on the propagating constant from those of the previous longitudinal step. Mathematically, this can be expressed as [77,78]:

$$\frac{\Phi_{M,p}^{q}}{\Phi_{M-1,p}^{q}} = \frac{\Phi_{M,p}^{q+1}}{\Phi_{M-1,p}^{q+1}} = e^{jk_x\Delta X} \tag{3.18}$$

where k_x is the wave number for a plane wave radiating in the X direction. The method assumes the same exponential dependence between the previous step q and the next step $q+1$. From the previous step, the wave number k_x can be determined and then used to find the field of the next step as in Equation (3.18).

The TBC of Equation (3.18) is applied to all computational boundaries and then included in Equations (3.16a) and (3.16b) and later in the corresponding matrix Equations for programming in the FORTRAN codes. Appendices A and B present the codes for the linear and nonlinear BPM with TBC solutions respectively.

Chapter 4   Modeling

The focus of our research is to find out any alterations to the features of the applied initial fields after some distance and explain the dynamics of the optical vortex propagation. All results shown and discussed in this chapter are either semi-analytical solutions from coupled mode Equations or numerical simulations from our BPM programs.

4.1   Simulation data

Simulation programs are coded in FORTRAN as discussed in Chapter 3 and designed to have a number of input parameters and output data files containing the calculated numerical values. Images are generated by GNUPLOT using the data files with the arrangements shown in Figure 5. Numbers are computed in double-precision for more accuracy and written in data files as tables suitable for data entering and processing for GNUPLOT and HDF.

From Equation (3.16) discussed earlier, the transverse plane sampling intervals, ΔX and ΔY, and the number of longitudinal steps are inputted through the `parameters` statement in our program. The image resolution and the size of the square matrix as in Equation (3.13) is determined by the transverse plane sampling intervals which are set to $\Delta=\Delta X=\Delta Y$ in our program.

Furthermore, the number of longitudinal calculation steps is implemented as a `do-loop` in the FORTRAN code and it indicates how many ΔZ the field is propagated in the Z direction. An acceptable estimate through computer simulations for the longitudinal

calculation step could be $\Delta Z \sim \Delta/100$ in order to keep possible numerical errors to an acceptable level.
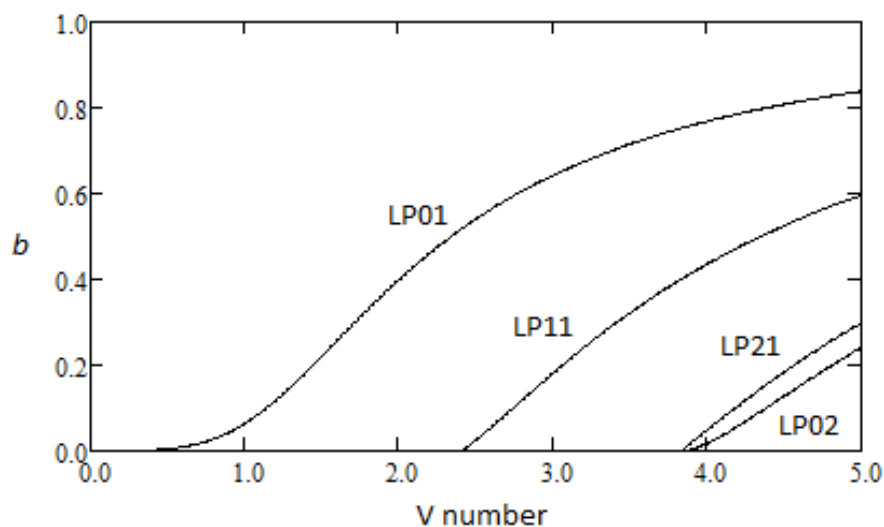
Figure 6 Linearly polarized modes versus *V* number [79].
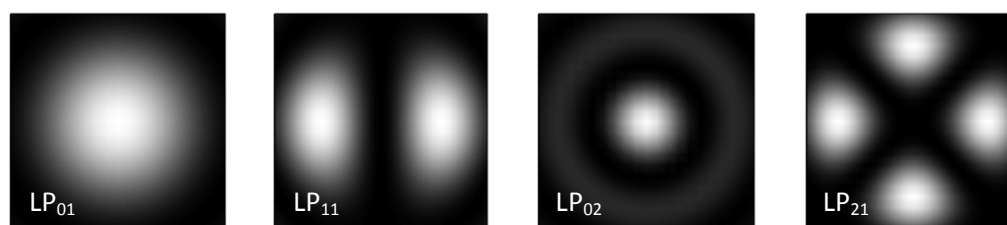
Figure 7 LP modes intensity distributions [79].

Simulation data are visualized by generating the transverse image of the field intensity and phase as well as the transverse interferogram with a reference Gaussian beam and the distribution of the index of refraction in the entire computational area. As explained earlier, several types of optical fibers are investigated: the multimode fiber and the triangular lattice array of fiber cores in different periodic arrangements.

The number of optical modes *V* that propagate in an optical fiber can be calculated from the relation:

$$V = \frac{2\pi}{\lambda} r \, NA \qquad (4.1)$$

where λ is the wavelength, *r* is the core radius and *NA* is the numerical aperture obtained as $NA = \sqrt{n_{core}^2 - n_{cladding}^2}$ such that n_{core} and $n_{cladding}$ are the index of refraction for core and cladding respectively.

Figure 6 illustrates the linearly polarized ($LP_{l,m}$) modes that can propagate in a step index optical fiber [79]. LP_{01} is the first propagating mode for the single mode fiber where $V \leq 2.405$. On the vertical axis, *b* is the normalized modal propagation constant and the *V* number is on the horizontal axis. The transverse distribution of the LP modes intensity is also shown in Figure 7 for mode indices *l,m* equal to 01,11,02 and 21 respectively [79].

4.2 Multimode fiber

When the *V* number is greater than or equal to 2.405 ($V \geq 2.405$), the fiber is known as a multimode fiber and there should be several modes of light fields that can exist and propagate in that fiber.

For simulations, let's assume that we select the beam width $w_0 = 40\mu m$, fiber core radius $r = 60\mu m$, $n_{core} = 1.47$, $n_{cladding} = 1.0$, numerical aperture $NA = 1.08$, transverse plane sampling interval $\Delta = 0.01$, normalized transverse lengths of X=Y=5.0 with a matrix size and a resolution of 500×500 (*N*=500) and a wavelength of $\lambda = 633nm$ for the He-Ne laser source.

The longitudinal calculation step is set to $\Delta Z=0.0001$ for $z_0=7.941$mm. Gaussian and optical vortex initial fields are simulated with various input parameters such as eccentricity with respect to the core center and angle of incidence with respect to the fiber core surface.

Figure 8(a) shows the distribution of the refractive index and the boundary between the core centered at the origin and the computational area. Figure 8(b) is the Gaussian beam centered at the origin (X=0,Y=0) in free space after a distance of $1.0z_0=7.941$mm for comparisons and Figure 8(c) shows the intensity of the beam in the multimode fiber after the same distance.

Light fields demonstrates more confinement inside the core circular boundary where the index of refraction changes from $n_0=1$ to $n_{core}=1.47$ as seen in Figure 8(c).
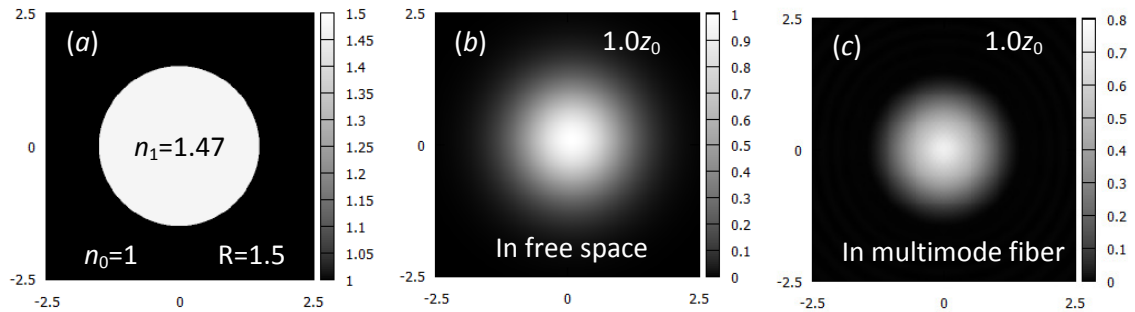
Figure 8 Index of refraction (a), Gaussian beam (b) and field at $1.0z_0$ in a multimode fiber (c).

Furthermore, Figure 9 shows the field distribution at propagation distance of $1.5z_0$ and $2.0z_0$ with a Gaussian initial field. Images are computed for a multimode fiber with the same parameters except for a resolutions of 250×250 and a transverse calculation step of $\Delta=0.02$. The intensity is higher in the region with a large index of refraction n_{core} where light is confined by the core.
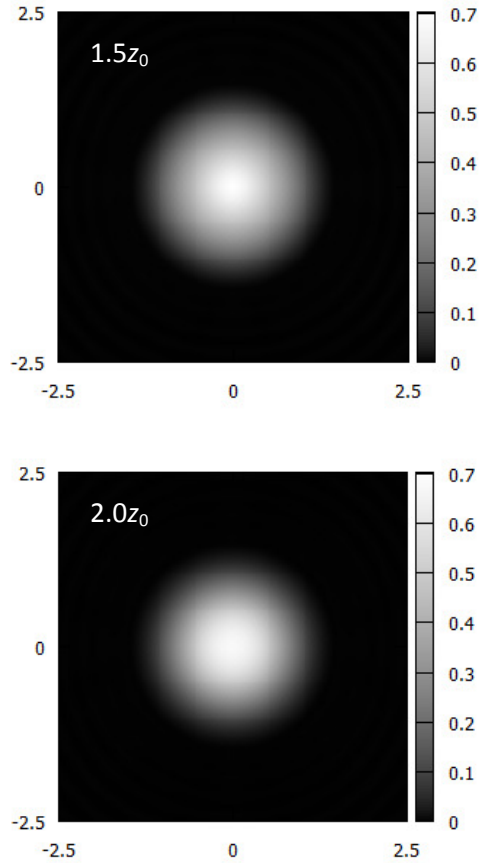
Figure 9 Field intensity distributions at $1.5z_0$ and $2.0z_0$ in a multimode fiber.

To investigate if the propagation of an optical vortex in a multimode fiber has different dynamics from the Gaussian beam, we perform additional simulations. The goal is to track the coordinates of the point of zero intensity or the point of dislocation where the phase spirals from $-\pi$ to π. The optical vortex intensity and phase was explained earlier and plotted in Figure 2.

For the same fiber used in Figure 8 we input a vortex beam. Figure 10(a) illustrates the intensity of the optical vortex propagating in the multimode fiber of Figure 8(a). Its phase is displayed in Figure 10(b). Its interferometry with a Gaussian beam at an angle of $\pi/4$ is also illustrated in Figure 10(c).
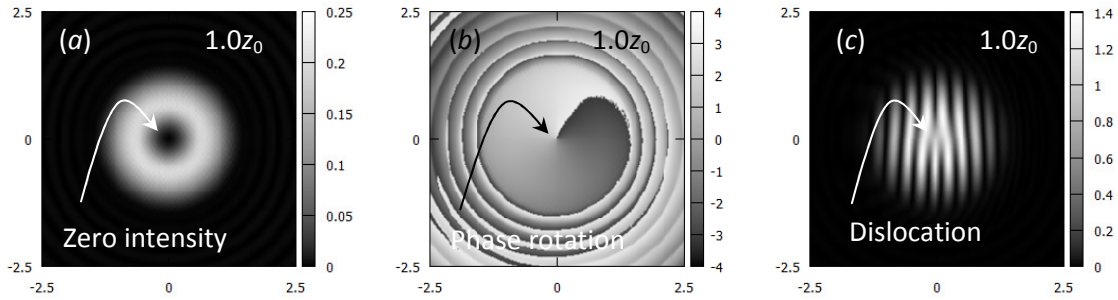
Figure 10 Vortex at $1.0z_0$ in a multimode fiber (a), phase (b) and interferogram (c).
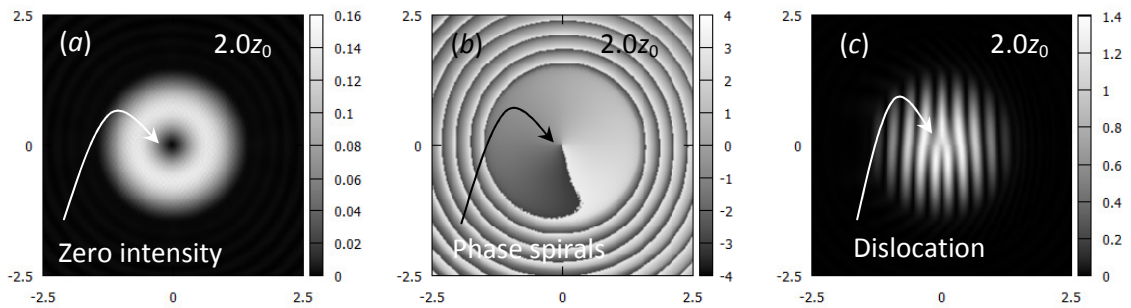
Figure 11 Vortex at $2.0z_0$ in a multimode fiber (a), phase (b) and interferogram (c).

At a resolution of 250×250, Figure 11(a) illustrates the vortex field intensity at $2.0z_0$ in a multimode fiber. The corresponding phase and interferogram are depicted in Figures 11(b) and 11(c) respectively. Simulations demonstrate that the vortex is guided inside the fiber core with its zero point intensity moved to the core center. Although spirals of the vortex phase and the dislocation point are distorted, they still can be recognized.

4.3   Hexagonal fiber array

This type of fiber array has more than one hundred single mode cores in a hexagonal arrangement. The cores are designed very close to each other with n_{core} and $n_{cladding}$ indices of refractions set in free space of $n_0 = 1.0$ for $\Delta n = n_{core} - n_{cladding} < 0.005$ with

V<2.405 for single mode operation according to Equation (4.1).
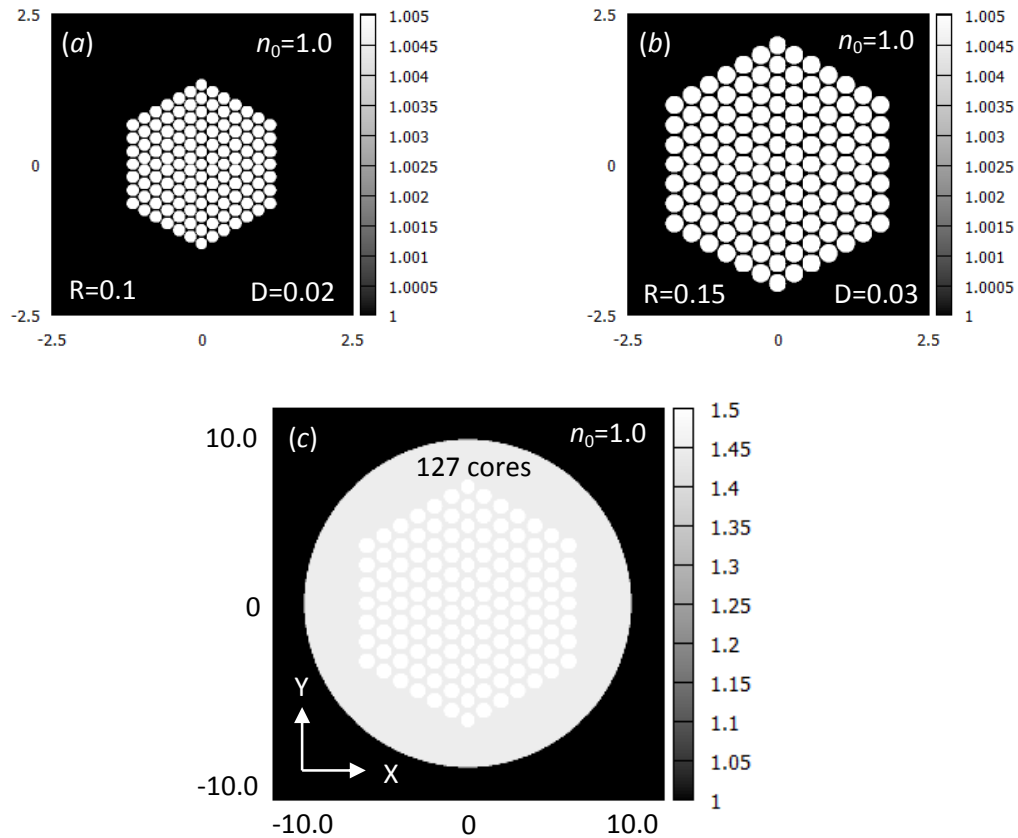
Figure 12 Hexagonal 127 cores *n*(X,Y) for n_{core}=1.005, R=0.1, D=0.02 (*a*), n_{core}=1.005, R=0.15,

D=0.03 (*b*) and n_{core}=1.5, $n_{cladding}$=1.45, R=0.29, D=0.22 with cladding in air (*c*).

An arrangement with an equal distance between any adjacent elements is selected since it can greatly simplify the calculations. All single mode cores are closely packed in order for light travelling along the propagation axis to be coupled among them. Figure 12 shows the overall *n*(X,Y) with 127 single mode cores in a hexagonal arrangement with a resolution of 500×500, a transverse plane sampling interval of Δ=0.01 and w_0=50μm.

Figures 12(*a*) and 12(*b*) show two configurations of fiber array with different normalized core radius R=0.1, 0.15 and different normalized distance between cores of

D=0.02, 0.03 respectively. Figure 12(*c*) is the arrangement used in this dissertation with cladding in air for R=0.29, D=0.22, n_{core}=1.5 and $n_{cladding}$=1.45.
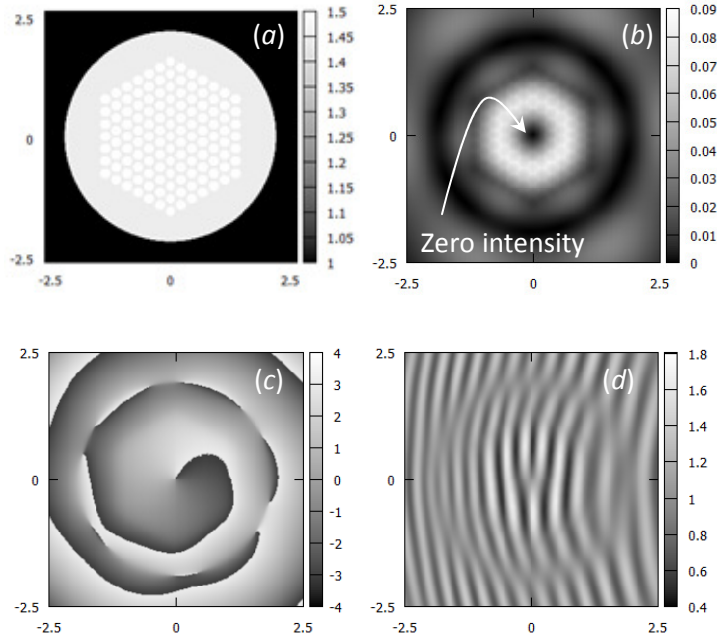
Figure 13 Vortex field at 1.0z_0, n(X,Y) for 127 cores, R=0.1, D=0.02, n_{core}=1.5 and $n_{cladding}$=1.45 (*a*), intensity (*b*), phase (*c*) and interferogram (*d*).

Figure 13(*b*) shows the optical field intensity when a vortex beam propagates in the fiber array with 127 cores in a hexagonal arrangement in Figure 13(*a*) for R=0.1, D=0.02, n_{core}=1.5 and $n_{cladding}$=1.45. The optical field is calculated at 1.0z_0 and a longitudinal calculation step of ΔZ=0.001 with w_0=50μm and λ=633nm. The point of zero intensity can be located at the central core.

Figures 13(*c*) and 13(*d*) show the phase and interferogram of the vortex beam with a plane wave at 1.0z_0. We can see that the original vortex still exists and the dislocation point can be observed in the middle by examining the phase and interferogram. In

addition, a number of new vortices are generated in this structure with a phase change from $-\pi$ to π as clearly shown in Figures 13(*c*) and 13(*d*). New vortices are formed in pairs with opposite charges. Thus, the overall charge on the transverse plane is conserved.

The simulation is adapted to work with matrices of different sizes such as 250×250, 500×500 and 1000×1000. A larger matrix generates improved resolution of images but may need more time to find the results. Image resolution is nearly satisfactory with a matrix size of 1000×1000 for magnifying reasons. All images have almost the same quality such as Figures 8, 9, 10 and 11.

4.4   Analytical solutions

The analytical solution for the hexagonal arrangement can be obtained by employing the coupled mode theory as a simplified approximation. The basic assumption is to consider that the mode of each single mode waveguide is obtained individually with amplitude as if there is no neighboring waveguide. With consideration of interactions with modes from neighboring waveguides, only the mode amplitudes vary with propagation distance.

The total electric field can be represented as a superposition of core modes as:

$$E(x, y, z) = \sum_m a_m(z) u_m(x, y) e^{-j\beta_m z} \tag{4.2}$$

where m is the index for the core element with the maximum value being equal to the number of cores, $a_m(z)$ is the amplitude as a function of z for element m, $u_m(x,y)$ is the transverse distribution and β_m is the constant of propagation for core m.

Taking into consideration the coupling among neighboring cores where coupling is strong owing to their close proximity and β_m is the same for all cores, the amplitudes $a_m(z)$ can be calculated with the following differential Equations:

$$\frac{da_m(z)}{dz} = \sum c_n a_n(z) \tag{4.3}$$

where $a_n(z)$ are the mode amplitudes for all nearest cores to the mth core with mode amplitude of $a_m(z)$ and c_n are their coupling factors.
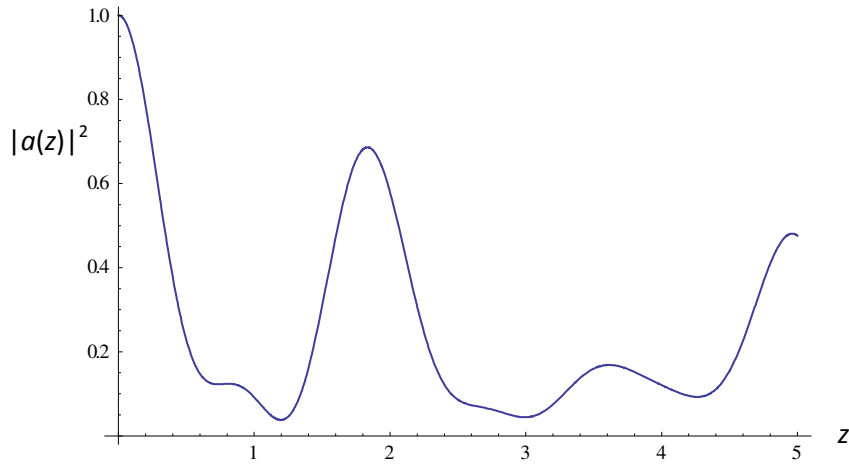
Figure 14 $|a(z)|^2$ for the middle core of Figure 13(*a*).

Figure 14 is a plot of the analytical solution of Equations (4.3) for the changes of $|a(z)|^2$ of the middle element located at the origin for the arrangement shown in Figure 13(*a*) for R=0.1, D=0.02, n_{core}=1.5 and $n_{cladding}$=1.45. The assumed initial conditions are $|a(z=0)|^2$=1.0 for the middle core at the origin but zero for all other cores.

4.5 Vortex detection

The method for vortex detection can be understood by referring to the optical vortex Equation (2.10) that is repeated here in another mathematical form as [83,84,85]:

$$U = V(x,y)e^{-jkz} \tag{4.4}$$

where $V(x,y)$ is a wave function with real and imaginary parts as:

$$V(x, y) = V_r(x, y) + jV_i(x, y) \tag{4.5}$$

Thus, vortices should lie on the zero crossings of both the real part $V_r(x,y)=0$ and the imaginary part $V_i(x,y)=0$ since the wave function $V(x,y)$ is single valued in the entire computational region. All such zero crossings should also show a phase change from $-\pi$ to π as explained before.
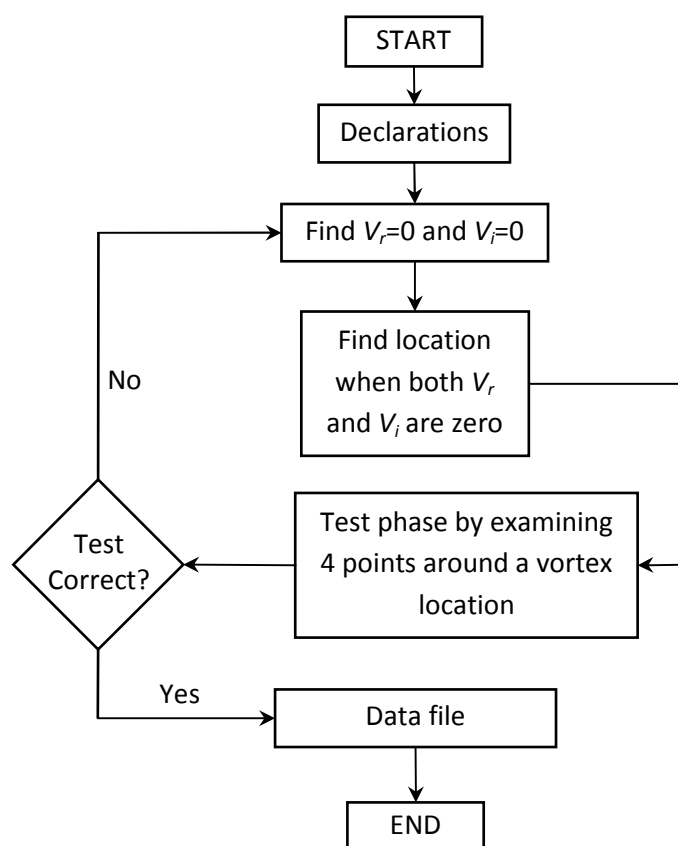
Figure 15 Zero crossings and phase change code outline.

Figure 15 is a flowchart for the FORTRAN program code used in our simulation that demonstrates how to determine the zero crossing points and phase change in any fiber arrangement based on Equation (4.4). $V_r(x,y)$ and $V_i(x,y)$ are assumed to be zero when

their amplitude is less than 1% of their peak value in Equation (4.5). In order to test the location of a vortex, the phase is tested at four points around the expected location. If the phase varies from $-\pi$ to π or from π to $-\pi$, then that location is considered a point of zero intensity with phase singularity with a polarity of ±1.

4.6   Coupling

An optical field $\psi(r)$ propagating in an optical single mode fiber is given by:

$$\psi(r) = \begin{cases} AJ_0(pr) & r \leq a \\ BK_0(qr) & r > a \end{cases} \tag{4.6}$$

where A and B are constants, $J_0(x)$ and $K_0(x)$ are the Bessel functions of the first and second kind with order zero and argument x respectively, p and q are real numbers and a is the radius of the fiber core.
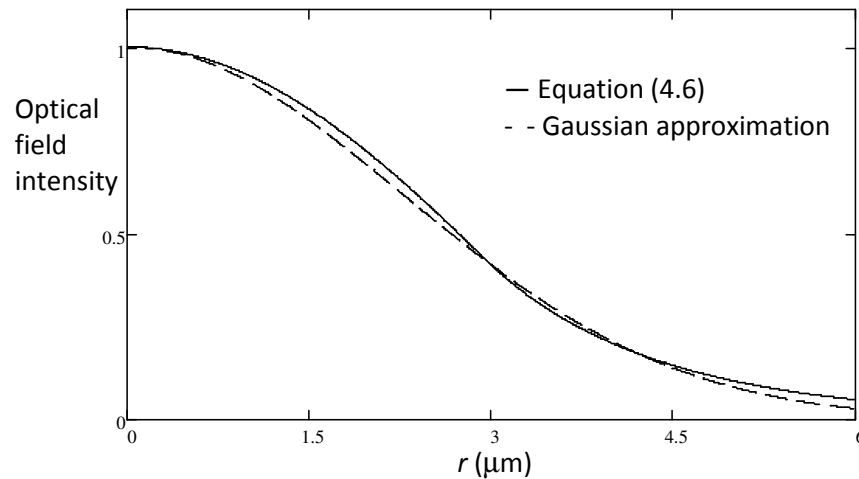
Figure 16 Gaussian field approximation.

At the fiber core boundary for $r=a$, Equation (4.6) is used to find the relations:

$$AJ_0(pa) = BK_0(qa) \tag{4.7}$$

$$ApJ_1(pa) = BqK_1(qa) \tag{4.8}$$

Substituting Equation (4.7) into Equation (4.8) gives the relation:

$$\frac{pJ_1(pa)}{J_0(pa)} = \frac{qK_1(qa)}{K_0(qa)} \tag{4.9}$$

Equation (4.9) is then solved numerically to obtain p and q previously shown in Equation (4.6) above.
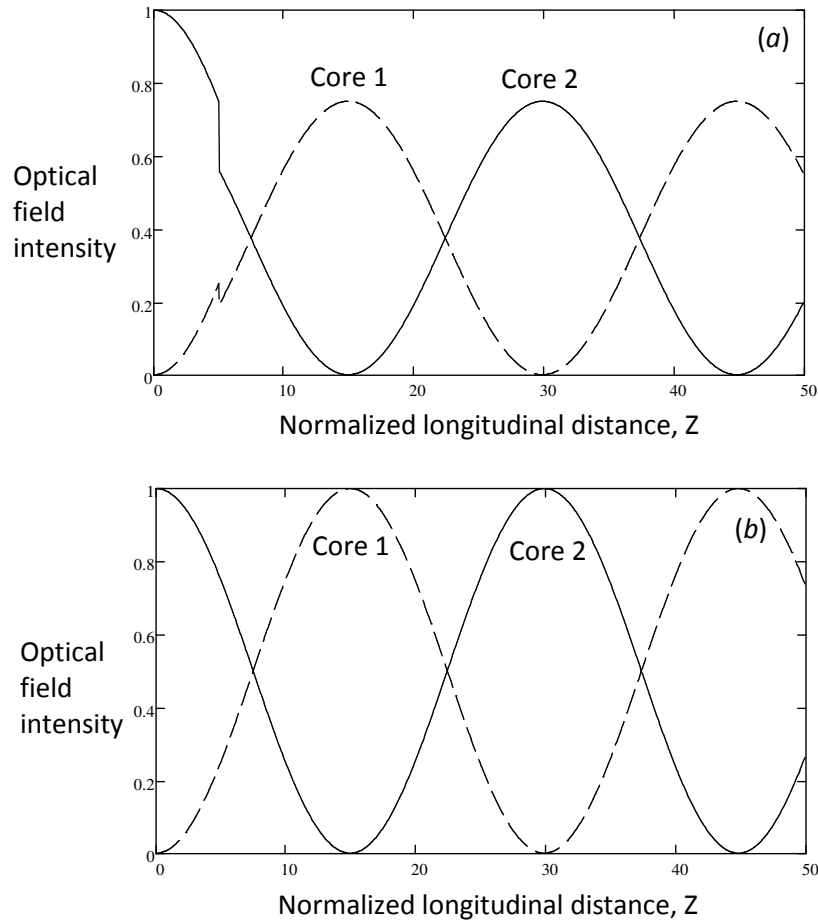
Figure 17 Coupling in two cores using beam propagation (*a*) and mode coupling (*b*) methods.

For the special case of p=0.557, q=0.574, A=1.0 and B=2.572, Equation (4.6) can be

easily plotted. The objective is to approximate the Gaussian field with a width of w_0 using the single mode field in Equation (4.6). Figure 16 illustrates a good approximation between both fields for w_0=5.4μm and a=3μm.

The coupling of the optical field intensity between two cores is shown in Figure 17 using BPM and coupling methods respectively. Figures 17(*a*) and 17(*b*) demonstrate excellent agreements between both techniques. Calculations are obtained for a Gaussian initial field, w_0=5.4μm, λ=1.5μm, R=0.92, D=2.0, n_{core}=1.5 and Z=50.

As notices in Figure 17(*a*), the Gaussian approximations obtained from Equation (4.9) and presented in Figure 16 causes little reflections and loss of energy until field coupling is established at just about Z=5.

As a consequence, the former derivation for the propagating optical field employing the BPM is an acceptable numerical technique for investigating the propagation in optical fibers.

Chapter 5 Triangular Lattice Fiber Array

Further investigations can be achieved for any core array arrangement in the optical waveguide. In addition to core radius, distances and angles between cores could be varied and may have different effects on the propagating optical field. In this chapter, we discuss the triangular lattice of fiber array as a generalization to any core array assembly. We also present the dynamics of a propagating optical vortex in this structure with different array parameters.

5.1 Basic arrangement

In geometry, a triangular lattice is a two dimensional array of discrete points or cores described by the position vector $\vec{R}$ as:

$$\vec{R} = c_1 \vec{a}_1 + c_2 \vec{a}_2 \tag{5.1}$$

where c_1 and c_2 are integer constants and $\vec{a}_1$ and $\vec{a}_2$ are primitive vectors such that any choice of the position vector $\vec{R}$ can generate a periodic lattice by varying c_1 and c_2 [82].
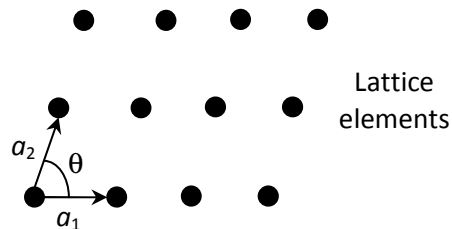
Figure 18 Two dimensional triangular lattice parameters.

Table 1 Parameters of the fundamental lattices [82].
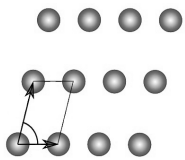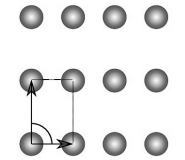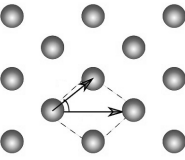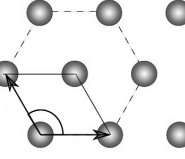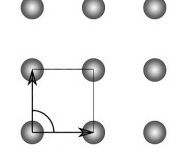
Lattice type	Primitive vectors	Angle	Geometry
Oblique	$\left\|\vec{a}_1\right\| \neq \left\|\vec{a}_2\right\|$	$\theta \neq 90^{\circ}$	
Rectangular	$\left\|\vec{a}_1\right\| \neq \left\|\vec{a}_2\right\|$	$\theta = 90^{\circ}$	
Centered rectangular	$\left\|\vec{a}_1\right\| \neq \left\|\vec{a}_2\right\|$	$\theta \neq 90^{\circ}$	
Hexagonal	$\left\|\vec{a}_1\right\| = \left\|\vec{a}_2\right\|$	$\theta = 120^{\circ}$	
Square	$\left\|\vec{a}_1\right\| = \left\|\vec{a}_2\right\|$	$\theta = 90^{\circ}$	

Figure 18 illustrates the triangular lattice arrangement with the vectors $\vec{a}_1$ and $\vec{a}_2$ expressed in Equation (5.1) with an angle θ between them. There are five fundamental shapes that can be derived from Figure 18 known as oblique, rectangular, centered rectangular, hexagonal and square. For more details, Table 1 shows the parameters for

every fundamental lattice type and its geometrical form [85].

Investigations for the propagation dynamics of an optical vortex in a triangular lattice is carried out according to the hexagonal arrangement shown in Figure 18.

5.2   Two-core array

The simplest form for any array type shown in Figure 18 or Table 1 contains only two cores each with a normalized radius R and a normalized distance D between them. The primary objective is to investigate the propagation dynamics of an optical vortex in a dual core waveguide and look for any possible changes in the original field or newly generated vortices.

Numerical simulations are performed for an array with R=0.4, D=0.1, n_{core}=1.05, $n_{cladding}$=1.04, and a beam with a width of w_0=5.0μm and wavelength of λ=1.5μm, i.e. $z_0 = \pi w_0^2 / \lambda \approx 52.36$μm. In order to increase coupling between the cores, the distance D is assumed to be very small and a very high Δn=0.01 is considered.

Figure 19 shows a sequence of images for the intensity and phase of an optical vortex beam propagating in a two core linear fiber array. The original optical vortex remains in its place and keeps its sense of rotation with new vortices generated at the boundaries of the cores. Conservation of charge is maintained as two new vortices with opposite spiral directions are generated keeping the overall polarity to +1.

The intensity sequence of images reveals that the optical fields are more coupled to the cores as the vortex propagates. The phase images show that the original vortex continues in the same location. However, new vortices bounce at the cores boundaries.

Intensity Sequence, X:-3 to 3, Y:-3 to 3   Phase Sequence, X:-3 to 3, Y:-3 to 3

Z=10.0

Original vortex

Z=12.0

New vortices

Z=13.0

Z=15.0

Z=17.0

Original vortex in same position

Z=18.0
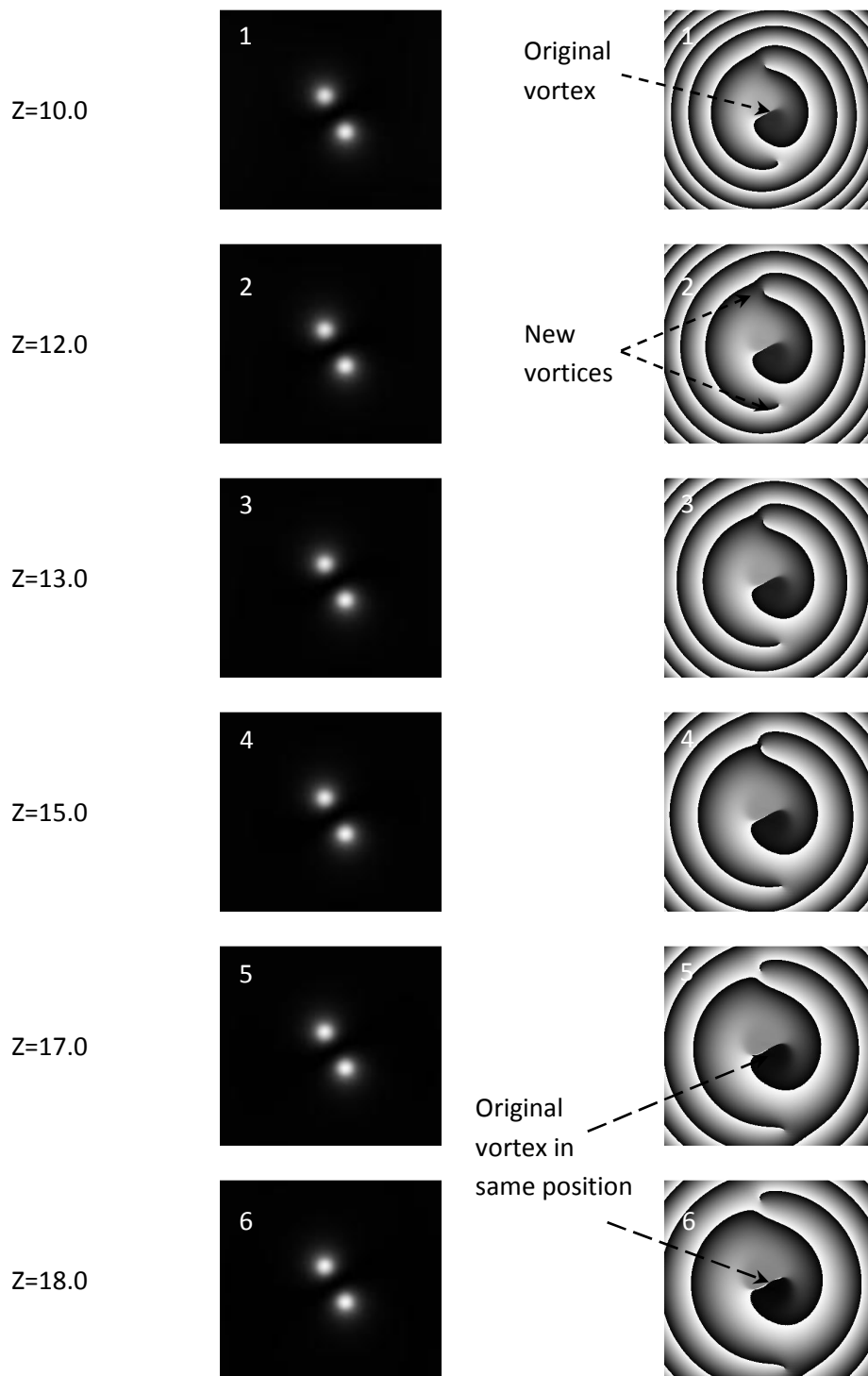
Figure 19 Image sequences (intensity and phase) showing creation of vortices in linear 2 cores

fiber array for R=0.4, D=0.1, n_{core}=1.05 and $n_{cladding}$=1.04.

Intensity Sequence, X:-3 to 3, Y:-3 to 3   Phase Sequence, X:-3 to 3, Y:-3 to 3

Z=10.0

Original
vortex

Z=12.0

New
vortices

Z=13.0

Z=15.0

Z=17.0

Original
vortex in
same position

Z=18.0
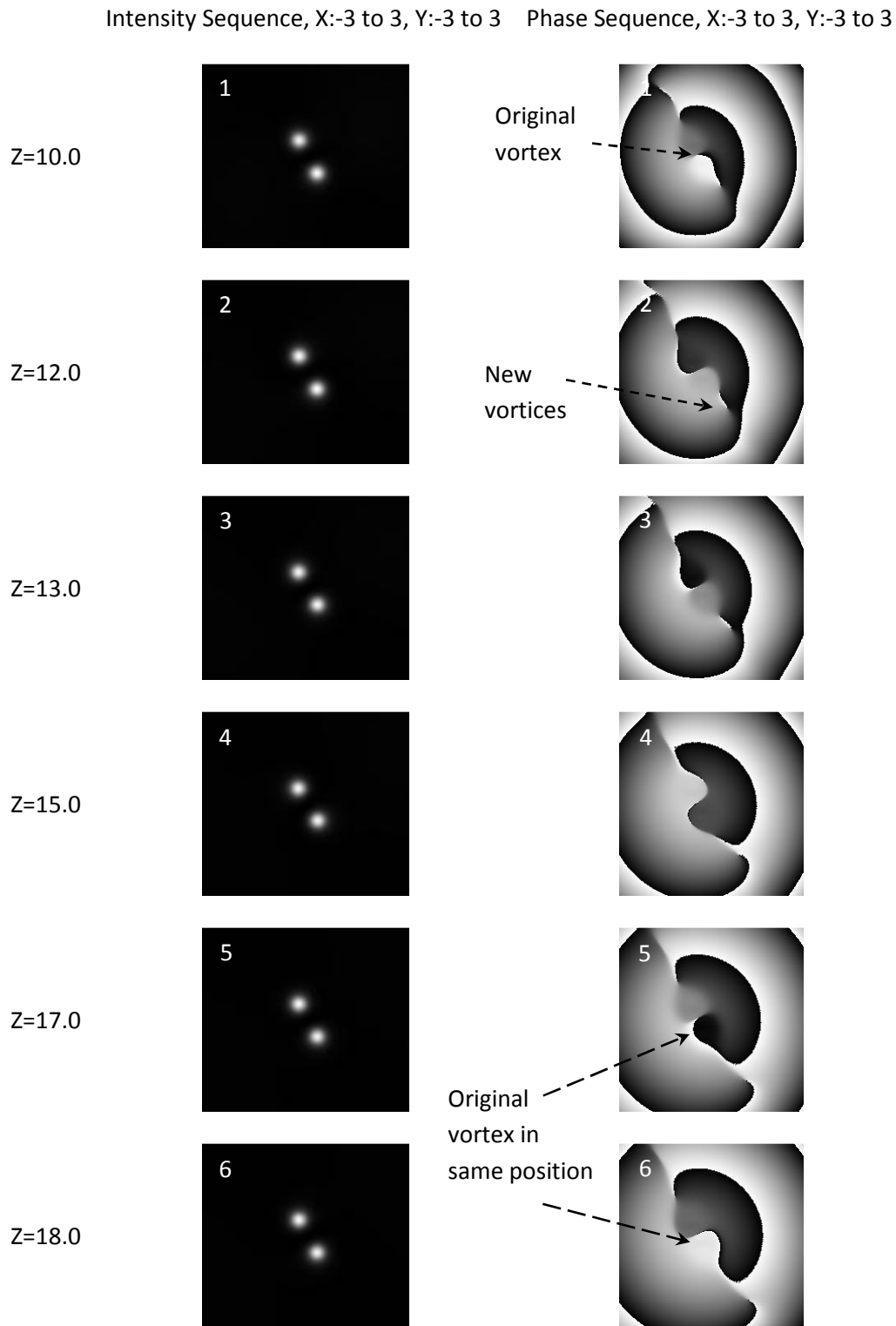
Figure 20 Image sequences (intensity and phase) showing creation of vortices in nonlinear 2

cores fiber array for R=0.4, D=0.1, n_{core}=1.05, $n_{cladding}$=1.04 and $n_2 I_0$=0.001.

The sequence of images for the intensity and phase for the nonlinear propagation in a two-core array is shown in Figure 20. Numerical simulations are carried out for nonlinearity n_2I_0=0.001 and Δn=0.01. Figure 20 shows almost the same features and results obtained from Figure 19.

5.3   Multi-core array

The approach discussed in earlier chapters and the methods used to produce field distributions are employed to investigate the propagation of an optical vortex in triangular lattices. Both linear and nonlinear lattices with the fiber array arrangements shown in Figure 21 are modeled with Equations (2.7) and (2.9) respectively.
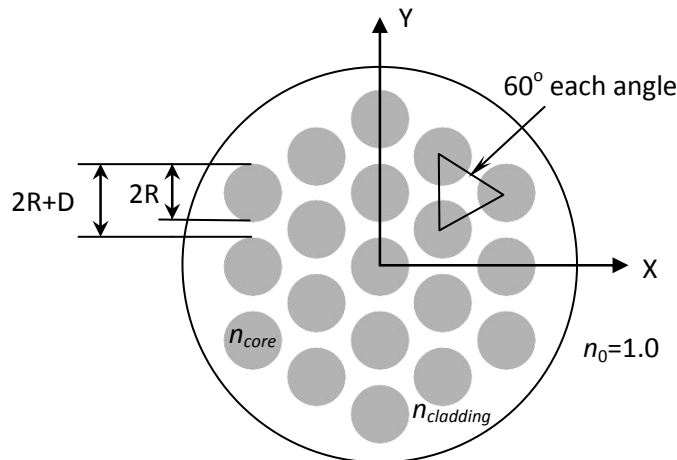
Figure 21 Lattice structure with an array of 19 cores in a hexagonal arrangement.

An example for the triangular lattice structure is shown in Figure 21 for a 19 core arrangement in a normalized rectangular coordinates, X=x/w_0 and Y=y/w_0, with a normalized radius of each core as R=r/w_0 and a normalized distance between cores as

$D=d/w_0$ where w_0 is the beam width and r and d are in µm. The index of refraction of each core is assumed to be very close to that of free space with a difference of $n_{core} - n_{cladding} = \Delta n \approx 0.005$ approximately and n_0=1.0 for free space [84].

5.3.1 Linear lattices

Numerical solutions are performed using Equation (2.7) for n_{core}=1.5, $n_{cladding}$=1.495, Δn=0.005, beam width of w_0=5.0µm and wavelength of λ=1.5µm with $z_0 = \pi w_0^2 / \lambda \approx$ 52.36µm. Single mode cores are assumed with a V number as $V = 2\pi r NA / \lambda < 2.405$ where $NA = \sqrt{n_{core}^2 - n_{cladding}^2} \approx 0.12$ is the optical numerical aperture.

The linear propagation of an optical vortex field in 61 cores in a hexagonal array with R=0.4 (r=Rw_0=2.0µm), D=0.2 (d=Dw_0=1.0µm) at Z=8 (z=Zz_0=418.88µm) is shown in Figure 22 for a resolution of N=1000 for the transverse plane of Δ=0.02 and longitudinal step size of ΔZ=0.005.

Figure 22 (*b*) is n(X,Y) and Figure 22(*a*) is a magnified image of the field intensity with spots of light in some cores. Since the cores are very close to each other at a constant distance, the field is coupled between them as it propagates. The phase of the propagated vortex field with charges of +1 or -1 of newly generated vortices is shown as a magnified image in Figure 22(*c*) where they demonstrate a phase change from –π to π. The total charge or polarity of vortices should be conserved to +1 which is the charge of the initial transmitted optical vortex field. New optical vortices are generated in pairs but then annihilate as they propagate inside the optical fiber array [87].
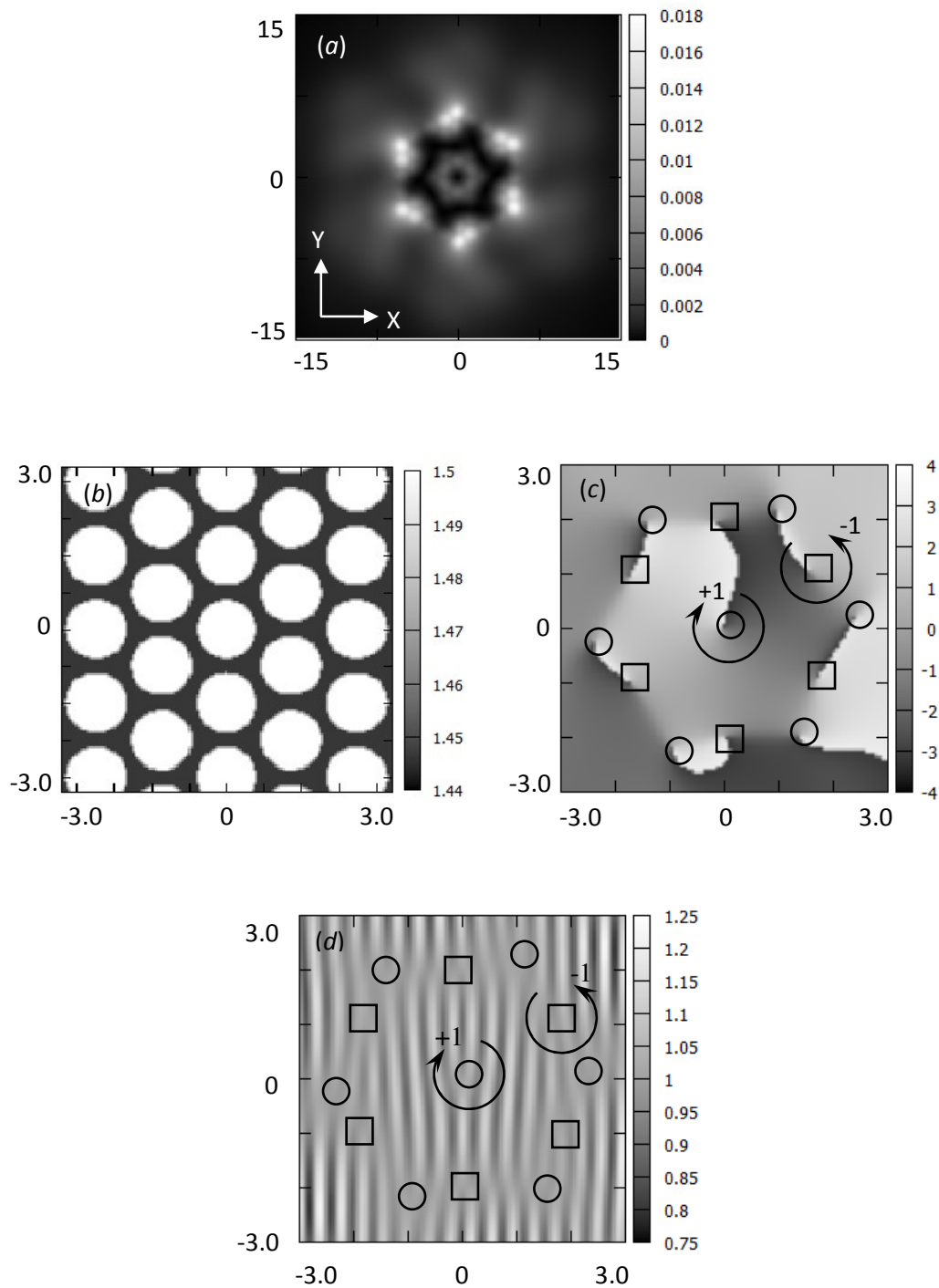
Figure 22 Intensity (a), n(X,Y) (b), phase (c) and interferogram (d) for 61 cores array with □=-1

charge and ○=+1 charge for n_{core}=1.5, $n_{cladding}$=1.495, Z=8, R=0.4 and D=0.2.
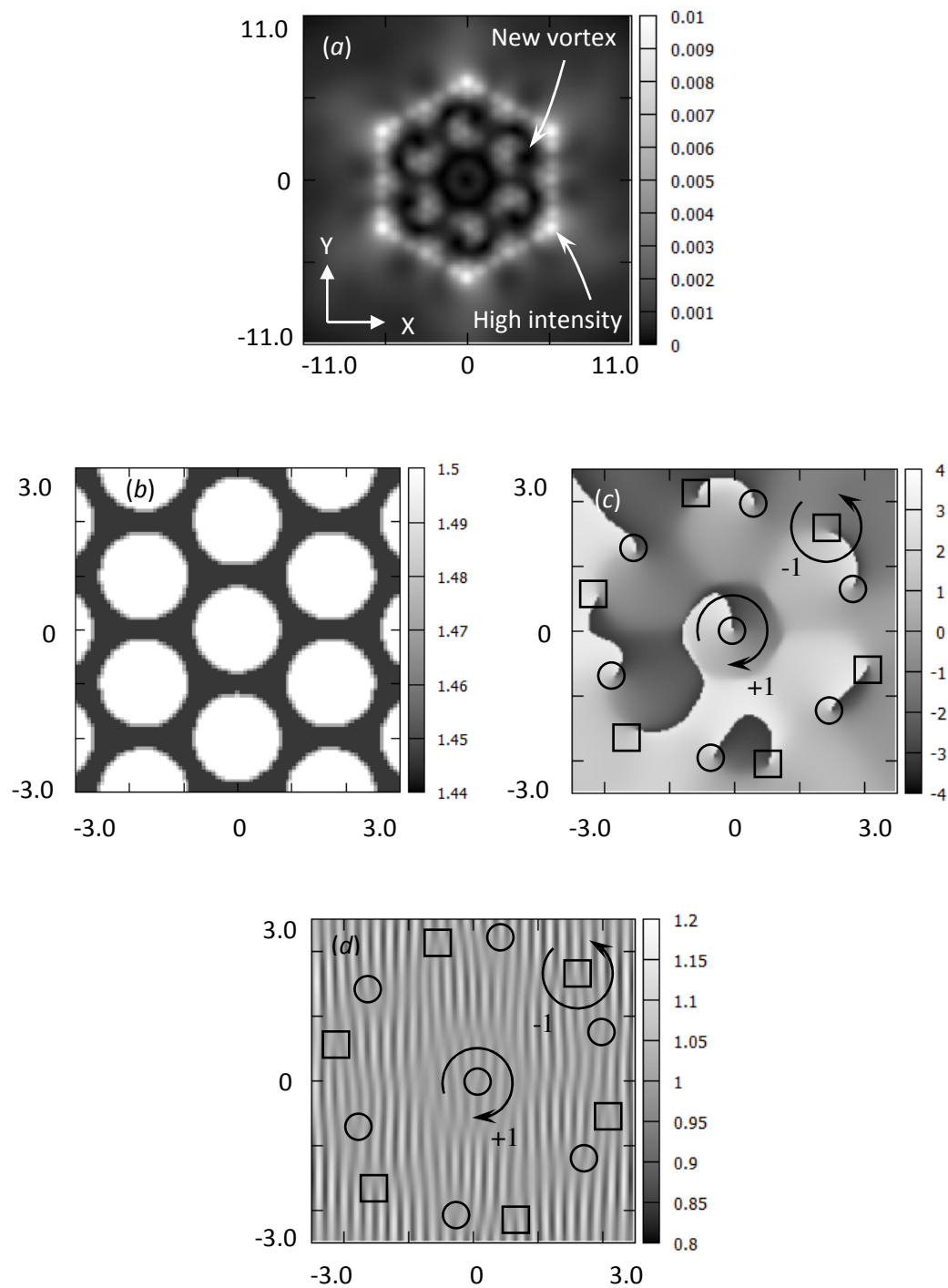
Figure 23 Intensity (a), *n*(X,Y) (*b*), phase (*c*) and interferogram (*d*) for 61 cores array with □=-1

charge and ○=+1 charge for n_{core}=1.5, $n_{cladding}$=1.495, Z=11, R=0.4 and D=0.2.

Topological charge should be always conserved when new vortices are formed and then annihilated in pairs with opposing charges. In Figure 22, conservation of charge is confirmed as 7*(+1)+6*(-1)=+1 where there are 7 vortices with +1 charge and 6 vortices with -1 charge. Figure 22(*d*) is the magnified image of the interferogram with a plane wave reference at an angle of π/4 with respect to the X axis which displays the dislocation points of new vortices at similar locations to that shown in Figure 22(*c*).

Table 2 New vortices at various Z's for R=0.4 and D=0.2 (polarities are in parentheses).

Z	37 cores	61 cores	91 cores	127 cores
0.0	1(+1)	1(+1)	1(+1)	1(+1)
1.0	9(+5,-4)	11(+6,-5)	15(+8,-7)	21(+11,-10)
2.0	11(+6,-5)	21(+11,-10)	35(+18,-17)	41(+21,-20)
3.0	13(+7,-6)	23(+12,-11)	31(+16,-15)	41(+21,-20)
4.0	11(+6,-5)	23(+12,-11)	35(+18,-17)	41(+21,-20)
5.0	21(+11,-10)	31(+16,-15)	39(+20,-19)	49(+25,-24)
6.0	21(+11,-10)	29(+15,-14)	37(+19,-18)	49(+25,-24)
7.0	19(+10,-9)	29(+15,-14)	37(+19,-18)	49(+25,-24)
8.0	25(+13,-12)	35(+18,-17)	45(+23,-22)	53(+27,-26)
9.0	23(+12,-11)	33(+17,-16)	47(+24,-23)	53(+27,-26)
10.0	29(+15,-14)	39(+20,-19)	49(+25,-24)	57(+29,-28)
11.0	27(+14,-13)	39(+20,-19)	49(+25,-24)	57(+29,-28)
12.0	25(+13,-12)	37(+19,-18)	47(+24,-23)	57(+29,-28)
13.0	35(+18,-17)	41(+21,-20)	53(+27,-26)	61(+31,-30)
14.0	37(+19,-18)	47(+24,-23)	55(+28,-27)	65(+33,-32)
15.0	41(+21,-20)	49(+25,-24)	57(+29,-28)	69(+35,-34)
16.0	41(+21,-20)	49(+25,-24)	61(+31,-30)	69(+35,-34)
17.0	45(+23,-22)	57(+29,-28)	69(+35,-34)	73(+37,-36)
18.0	49(+25,-24)	59(+30,-29)	69(+35,-34)	79(+40,-39)
19.0	55(+28,-27)	63(+32,-31)	71(+36,-35)	81(+41,-40)
20.0	59(+30,-29)	69(+35,-34)	79(+40,-39)	87(+44,-43)

Moreover, Figure 23 shows the propagated optical vortex field at Z=11 for 127 linear cores array with R=0.4, D=0.2, a resolution of *N*=1000 with Δ=0.016 and

longitudinal step size ΔZ=0.005. Figure 23(*b*) is *n*(X,Y) and Figure 23(*a*) is a magnified image of the field intensity with the spots of light coupled and spread in more near cores compared to the case in Figure 22(*a*). The corresponding phase from –π to π is shown in Figure 23(*c*) with 6 new pairs of vortices around the first vortex at the origin. Again, the conservation of charge holds. Figure 23(*d*) shows the interferogram of the vortex field with a plane wave reference at an angle of π/4 with respect to the X axis that reveals the points of dislocations for each created vortex.

Figure 24 vortex density with respect to Z for different number of cores for n_{core}=1.5, $n_{cladding}$=1.495, R=0.4 and D=0.2.

The approach used to generate Figures 22 and 23 is employed to investigate the generation of new vortices with respect to Z when the number of cores, core radius R and distance D are varied. Some results are listed in Table 2 for Z from 0.0 to 20.0 when the number of cores is 37, 61, 91 and 127 respectively and visualized as vortex density in

Figure 24 for R=0.4 and D=0.2 with the same number of cores. The vortex density is defined as the number of vortices per unit area of the fiber array. Polarities (either + or -) of newly generated vortices are also recorded in Table 2 which clearly demonstrate and confirm the conservation of charge.

Table 3 New vortices at various R's for Z=8.0 and D=0.2 (polarities are in parentheses).

R	37 cores	61 cores	91 cores	127 cores
0.2	21(+11,-10)	27(+14,-13)	39(+20,-19)	47(+24,-23)
0.3	23(+12,-11)	31(+16,-15)	43(+22,-21)	51(+26,-25)
0.4	25(+13,-12)	35(+18,-17)	45(+23,-22)	53(+27,-26)
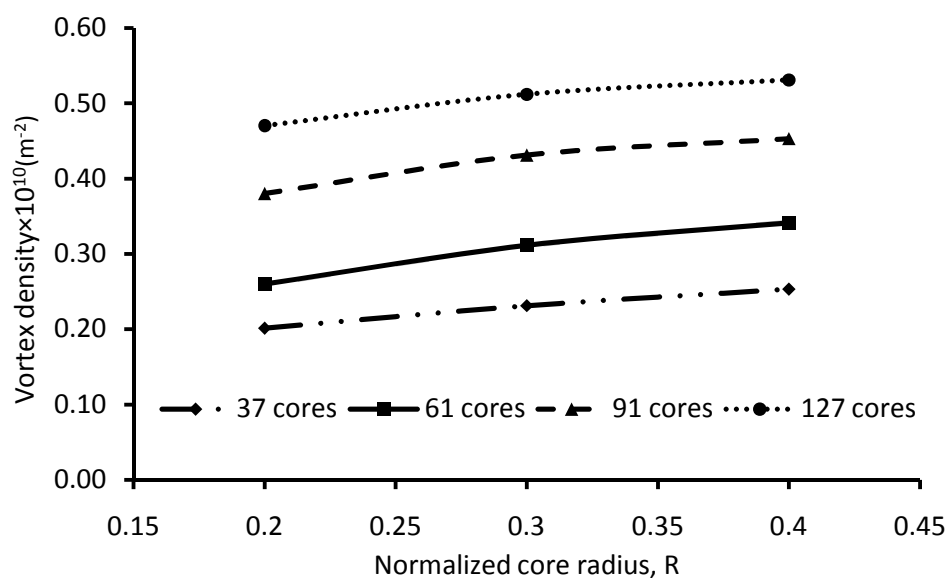
Figure 25 Vortex density with respect to R for different number of cores for n_{core}=1.5, $n_{cladding}$=1.495, Z=8.0 and D=0.2.

As revealed by these Figures, the generation of new vortices is very dynamic and varies widely with respect to Z and the number of cores. More vortices are created as the number of cores increases and the beam propagates to longer distances. However, new

vortices may not exist continually and may possibly vanish with other new vortices generated at different locations.

Table 4 New vortices at various D's for Z=8.0 and R=0.4 (polarities are in parentheses).

D	37 cores	61 cores	91 cores	127 cores
0.2	25(+13,-12)	35(+18,-17)	45(+23,-22)	53(+27,-26)
0.3	23(+12,-11)	31(+16,-15)	41(+21,-20)	51(+26,-25)
0.4	21(+11,-10)	31(+16,-15)	41(+21,-20)	51(+26,-25)

Figure 26 Vortex density with respect to D for different number of cores for n_{core}=1.5, $n_{cladding}$=1.495, Z=8.0 and R=0.4.

Table 2 shows the data at Z=8.0 with differences in the number of new vortices as the number of cores is varied. Core radius may also affect the number of newly generated vortices as illustrated in Table 3 and visualized as vortex density in Figure 25 for R=0.2, 0.3 and 0.4, Z=8.0 and D=0.2 for the same number of cores.

The generation of new vortices is very sensitive to the core radius particularly when

there are more cores. In addition, variation of the distance between cores could show some changes in the number of new vortices as shown in Table 3 and visualized as vortex density in Figure 26 for various D's when 0.4, R=0.4 and Z=8.0.

5.3.2   Nonlinear lattices

Numerical solutions are obtained using the normalized nonlinear Schrodinger Equation (2.9) for a positive nonlinearity n_2I_0=0.0001 and $\Delta n = 0.005$. Simulations are evaluated for n_{core}=1.5, $n_{cladding}$=1.495, beam width of w_0=5.0μm and wavelength of λ=1.5μm with $z_0 = \pi w_0^2/\lambda \approx 52.36$μm. Single mode cores are also assumed with a *V* number as $V = 2\pi r NA/\lambda < 2.405$ where $NA = \sqrt{n_{core}^2 - n_{cladding}^2} \approx 0.12$ is the numerical aperture.

The propagation of the optical vortex field in this nonlinear medium is shown in Figure 27 at Z=8 (*z*=Zz_0=418.88μm) for 61 cores in a hexagonal arrangement array with R=0.4 (*r*=Rw_0=2.0μm), D=0.2 (*d*=Dw_0=1.0μm), a resolution of *N*=1000 with Δ=0.02 and longitudinal steps size ΔZ=0.005. Figure 27(*b*) shows *n*(X,Y). Figure 27(*a*) is a magnified image of the field intensity showing the spots of light in some cores. The optical field is coupled among them as it propagates in the array because the cores are very close to each other. The corresponding phase of the vortex field changing from –π to π corresponding to charges of +1 or -1 is shown in Figure 27(*c*). Similar to the linear medium, the topological charge should be always conserved when new optical vortices are formed and then annihilated in pairs with opposing charges. In this case, conservation is confirmed as 3*(+1)+2*(-1)=+1 where there are 3 vortices with +1 charge and 2 vortices with -1 charge.
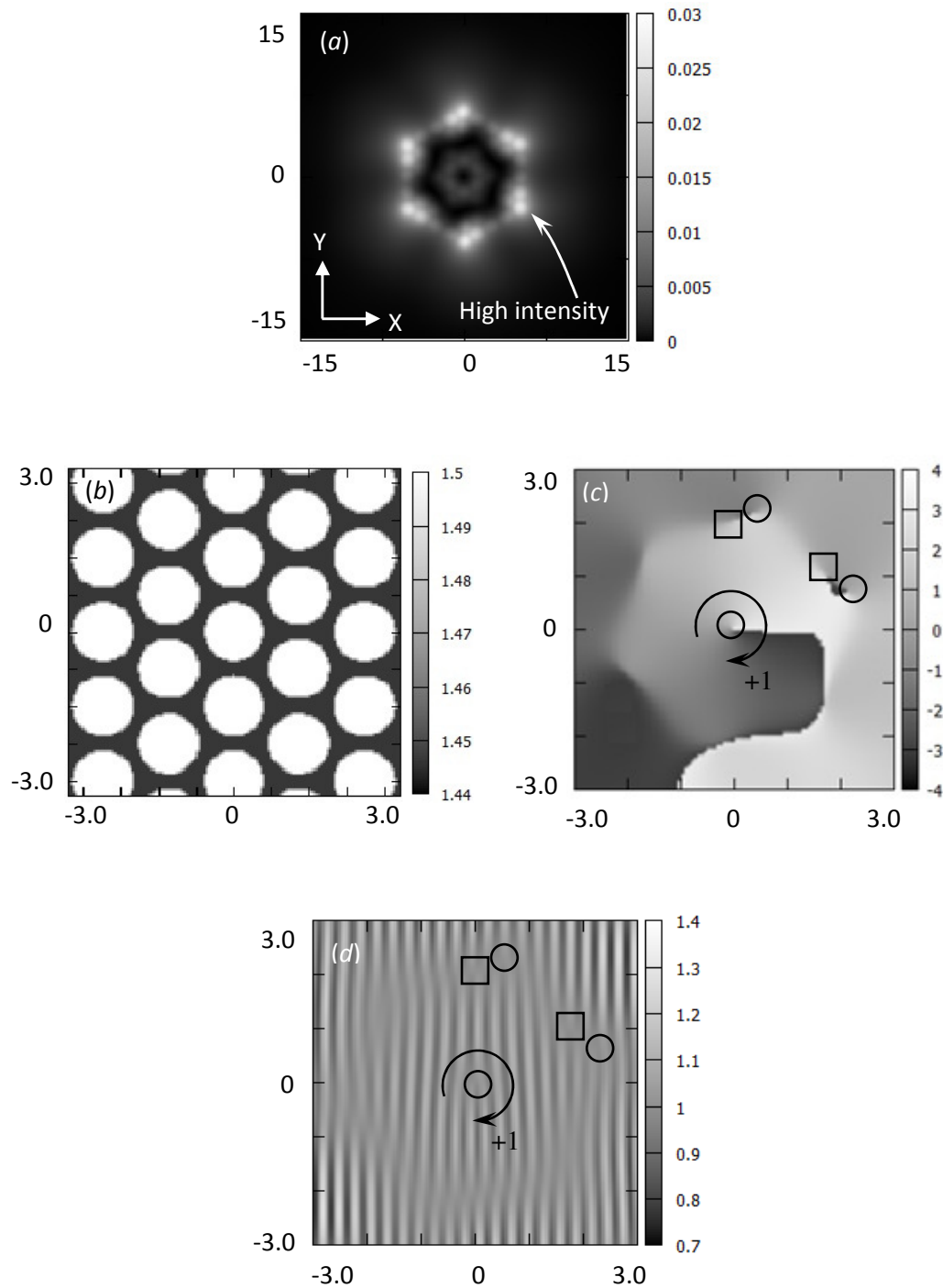
Figure 27 Intensity (*a*), *n*(X,Y) (*b*), phase (*c*) and interferogram with a plane wave reference (*d*)

for 61 cores array with □=-1 charge and ○=+1 charge at Z=8.0.

Figure 28 Intensity (*a*), *n*(X,Y) (*b*), phase (*c*) and interferogram with a plane wave reference (*d*)

for 127 cores array with □=-1 charge and ○=+1 charge at Z=11.

Figure 27(*d*) is the interferogram with a plane wave reference at an angle of π/4 with respect to the X axis with the dislocation points of individual new optical vortices at comparable locations to that shown in Figure 27(*c*).

Table 5 New vortices at various Z's for R=0.4 and D=0.2 (polarities are in parentheses).

Z	37 cores	61 cores	91 cores	127 cores
0.0	1(+1)	1(+1)	1(+1)	1(+1)
1.0	9(+5,-4)	11(+6,-5)	15(+8,-7)	21(+11,-10)
2.0	13(+7,-6)	21(+11,-10)	37(+19,-18)	41(+21,-20)
3.0	13(+7,-6)	23(+12,-11)	33(+17,-16)	43(+22,-21)
4.0	13(+7,-6)	23(+12,-11)	37(+19,-18)	43(+22,-21)
5.0	21(+11,-10)	31(+16,-15)	41(+21,-20)	51(+26,25)
6.0	21(+11,-10)	29(+15,-14)	37(+19,-18)	51(+26,25)
7.0	21(+11,-10)	31(+16,-15)	37(+19,-18)	51(+26,25)
8.0	27(+14,-13)	35(+18,-17)	47(+24,-23)	55(+28,-27)
9.0	25(+13,-12)	35(+18,-17)	47(+24,-23)	55(+28,-27)
10.0	31(+16,-15)	39(+20,-19)	51(+26,25)	59(+30,-29)
11.0	29(+15,-14)	41(+21,-20)	51(+26,25)	59(+30,-29)
12.0	31(+16,-15)	39(+20,-19)	49(+25,-24)	59(+30,-29)
13.0	37(+19,-18)	43(+22,-21)	55(+28,-27)	63(+32,-31)
14.0	37(+19,-18)	49(+25,-24)	57(+29,-28)	67(+34,-33)
15.0	41(+21,-20)	51(+26,25)	59(+30,-29)	71(+36,-35)
16.0	43(+22,-21)	51(+26,25)	63(+32,-31)	71(+36,-35)
17.0	47(+24,-23)	59(+30,-29)	69(+35,-34)	75(+38,-37)
18.0	51(+26,25)	59(+30,-29)	69(+35,-34)	79(+40,-39)
19.0	57(+29,-28)	65(+33,-32)	73(+37,-36)	83(+42,-41)
20.0	61(+31,-30)	71(+36,-35)	81(+41,-40)	87(+44,43)

Furthermore, Figure 28 shows the optical vortex field at Z=11 for 127 cores array with R=0.4, D=0.2, *N*=1000 resolution with Δ=0.04 and ΔZ=0.005. Figure 28(*b*) shows *n*(X,Y). Figure 28(*a*) is a magnified image of the optical field intensity with the spots of light coupled into cores and spreading more to neighboring cores compared to the case shown in Figure 27(*a*). The phase of the field from –π to π is shown as in Figure 28(*c*)

with new pairs of vortices forming around the first vortex at the origin. Figure 28(*c*) again demonstrates the conservation of charge. Figure 28(*d*) also shows the interferogram of the vortex field with a plane wave reference at an angle of $\pi/4$ with respect to the X axis that shows the points of dislocation for each new vortex.
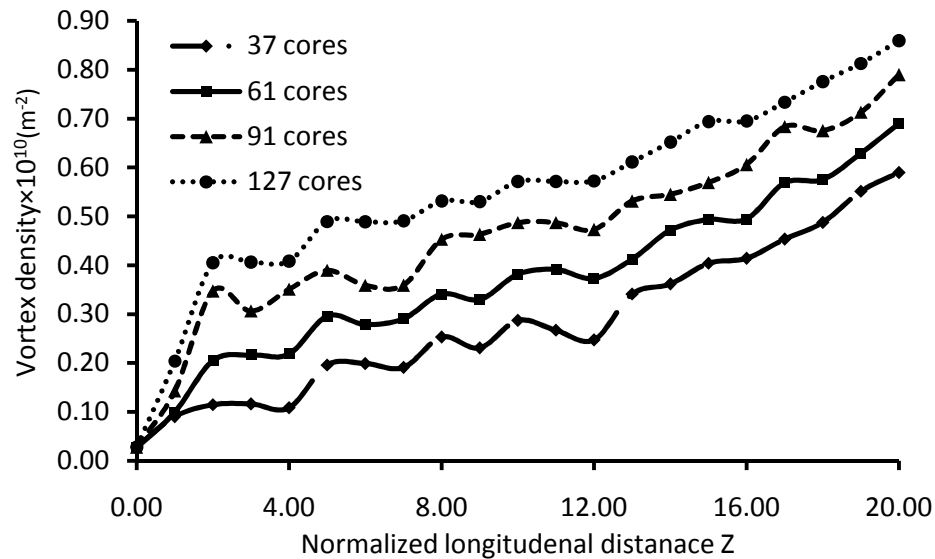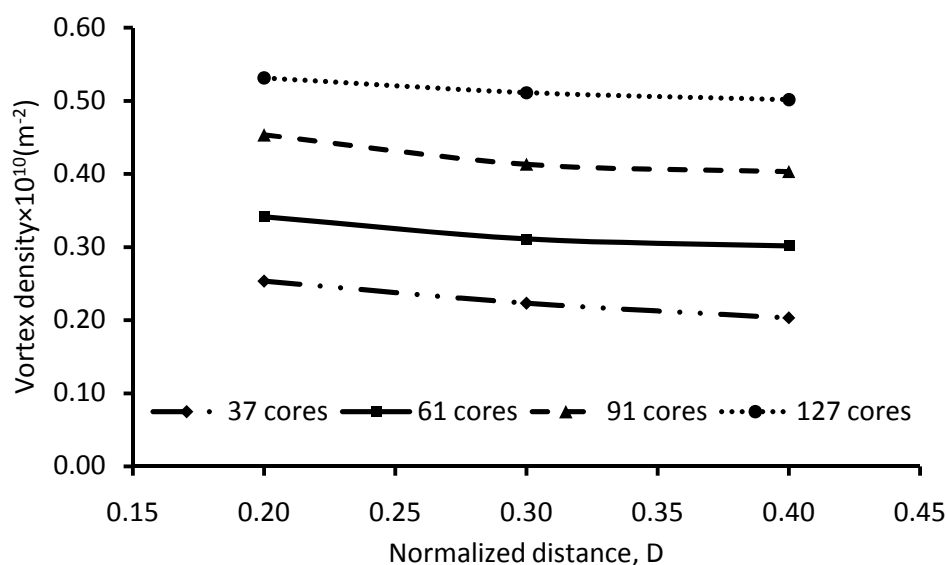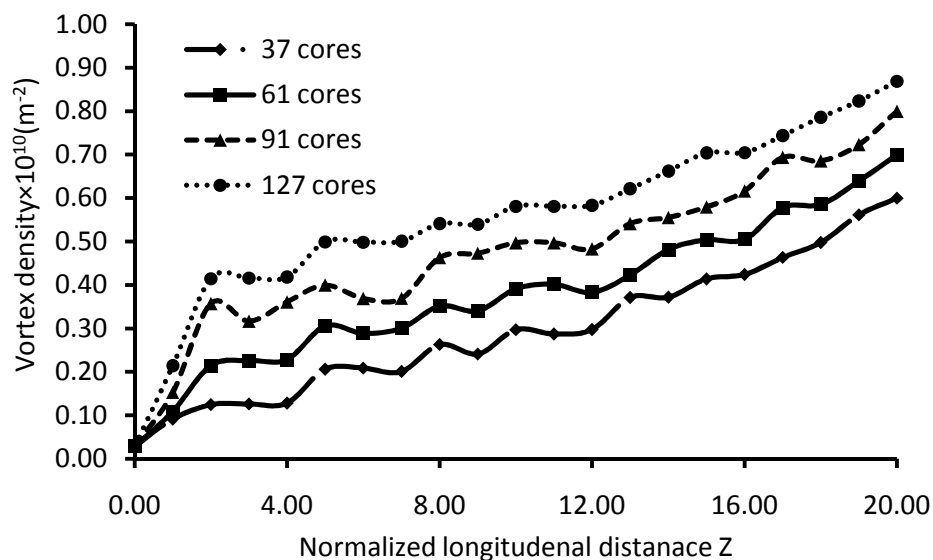

Figure 29 vortex density with respect to Z for different number of cores for n_{core}=1.5,

$n_{cladding}$=1.495, R=0.4 and D=0.2.

The method for the generation of Figures 27 and 28 is employed to investigate the change in vortex density with respect to Z when the number of cores, core radius R and distance D are varied. Some results are listed in Table 5 for Z from 0 to 20.0 when the number of cores is 37, 61, 91 and 127 respectively and visualized as vortex density in Figure 29 for R=0.4 and D=0.2 for the same number of cores. Polarities (either + or -) of newly generated vortices are also recorded in Table 5 which clearly demonstrates and confirms the conservation of charge.

As illustrated in Table 5, the production of new vortices is extremely dynamic with respect to Z and the number of cores. More vortices are created as the number of cores increases and the beam propagates to farther distances. New vortices start to appear at shorter propagation distance but even more new vortices are produced when the number of cores is higher. However, new vortices may not exist all the time and could disappear with other new vortices generated at different sites.

Table 6 New vortices at various R's for Z=8.0 and D=0.2 (polarities are in parentheses).

R	37 cores	61 cores	91 cores	127 cores
0.2	19(+10,-9)	25(+13,-12)	37(+19,-18)	45(+23,-22)
0.3	23(+12,-11)	31(+16,-15)	41(+21,-20)	51(+26,-25)
0.4	27(+14,-13)	35(+18,-17)	47(+24,-23)	55(+28,-27)

Figure 30 Vortex density with respect to R for different number of cores for n_{core}=1.5, $n_{cladding}$=1.495, Z=8.0 and D=0.2.

As in Table 5, the longitudinal distance at Z=8.0 shows differences in the number of

new vortices as the number of cores is varied. Core radius may also affect the number of newly generated vortices as listed in Table 6 and depicted in Figure 30 for various R at Z=8.0 and D=0.2 for the same number of cores.

The generation of new vortices is sensitive to the core radius such as the sharp change from one vortex to 7 vortices for 61 cores. Figure 30 shows a general tendency of an increase in the number of vortices as the core radius increases. In addition, the variation of the distance between cores could show some changes in the number of new vortices as listed in Table 7 and visualized in Figure 31 for various D for R=0.4 and Z=8.0. This parameter may have a decreasing effect as the distance increases.

Table 7 New vortices at various D's for Z=8.0 and R=0.4 (polarities are in parentheses).

D	37 cores	61 cores	91 cores	127 cores
0.2	27(+14,-13)	35(+18,-17)	47(+24,-23)	55(+28,-27)
0.3	25(+13,-12)	31(+16,-15)	43(+22,21)	51(+26,-25)
0.4	21(+11,-10)	29(+15,-14)	33(+17,-16)	49(+25,-24)
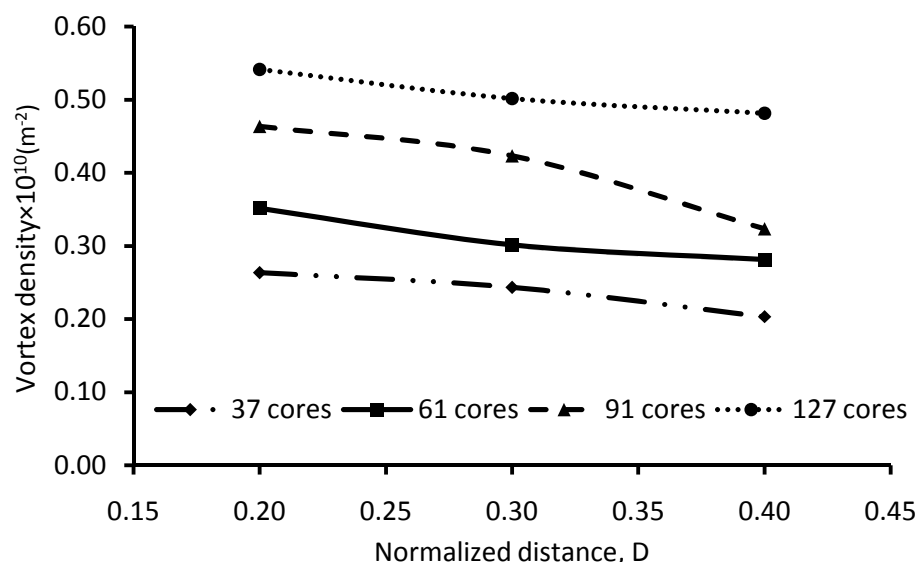
**Figure 31** Vortex density vs. D for n_{core}=1.5, $n_{cladding}$=1.495, Z=8.0 and R=0.4.
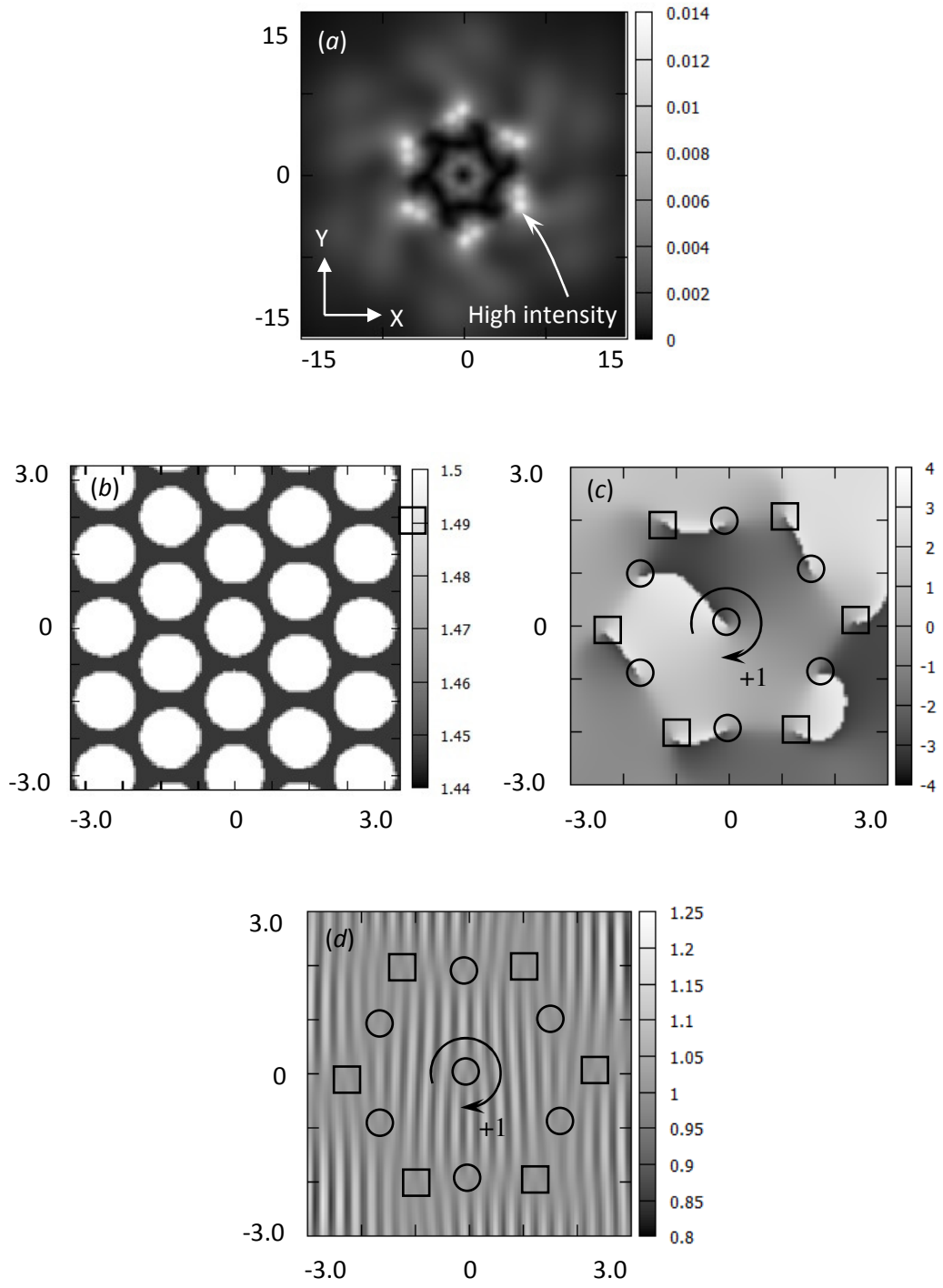
Figure 32 Intensity (*a*), *n*(X,Y) (*b*), phase (*c*) and interferogram with a plane wave reference (*d*)

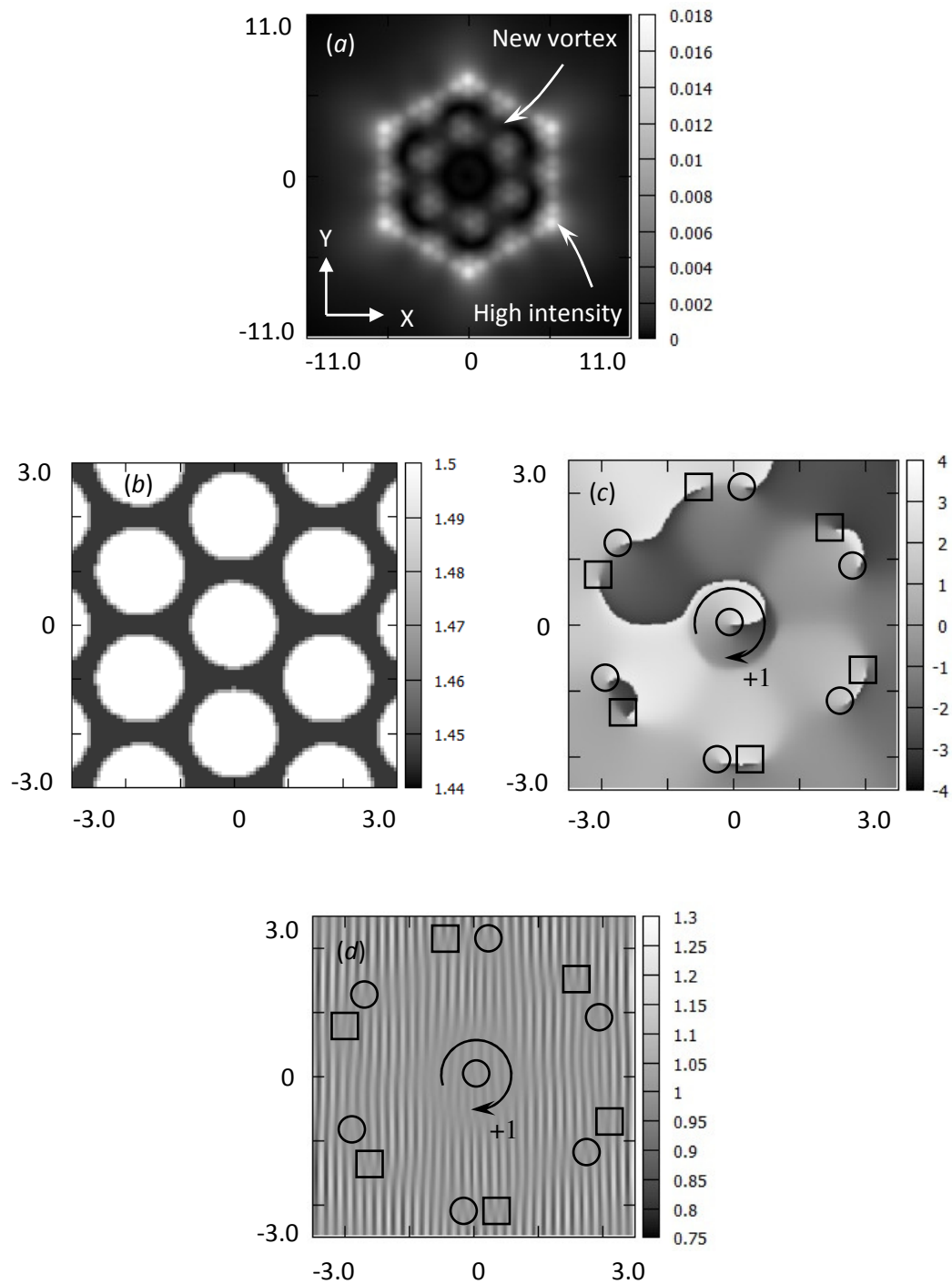for 61 cores array with □=-1 charge and ○=+1 charge.
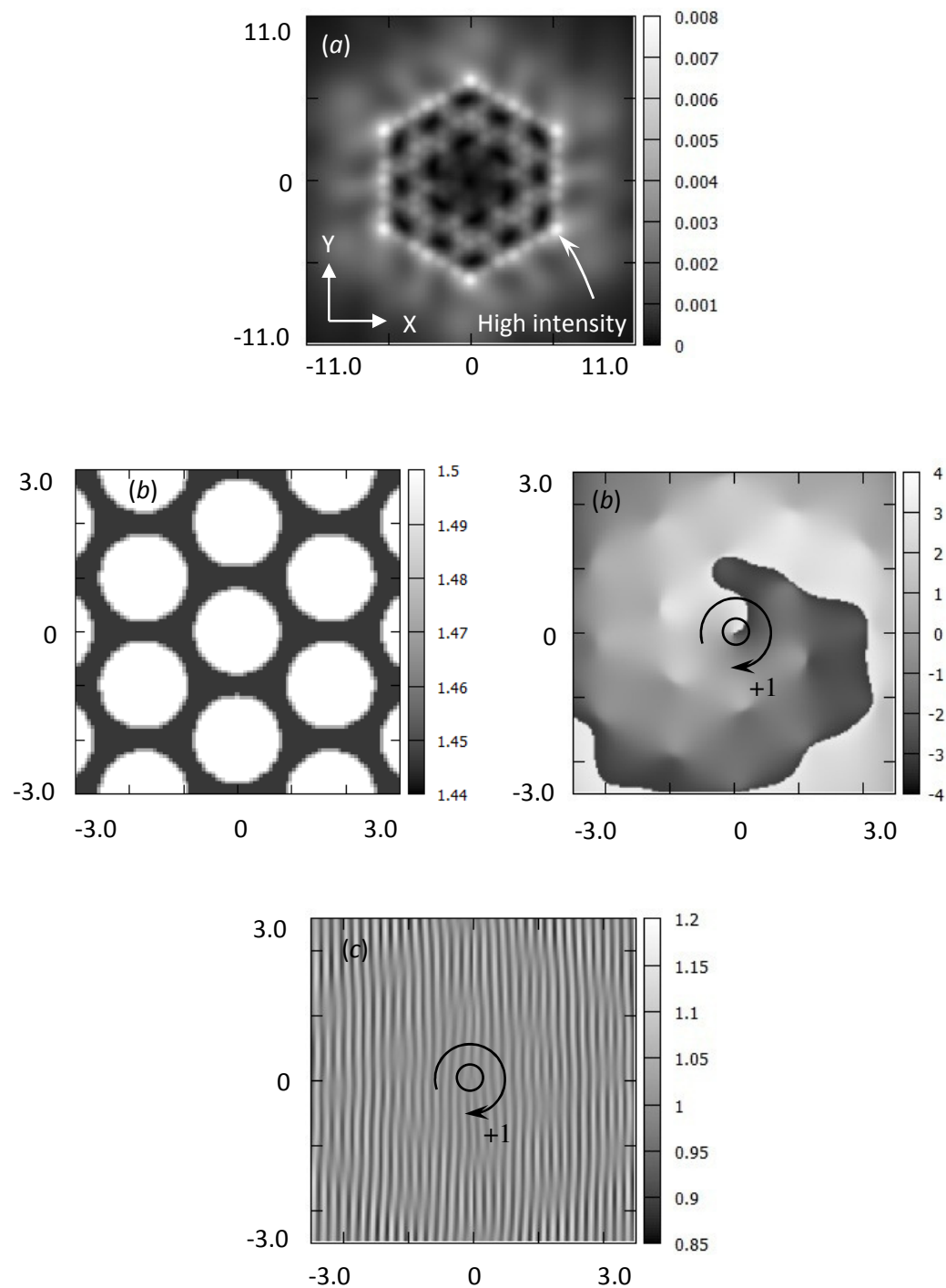
Figure 33 Intensity (*a*), *n*(X,Y) (*b*), phase (*c*) and interferogram with a plane wave reference (*d*)

for 127 cores array with □=-1 charge and ○=+1 charge.

The same analyses are also repeated for a negative nonlinearity of n_2I_0=-0.0001 and Δn=0.005. The propagated optical vortex field in this nonlinear medium is shown in Figure 32 at Z=8 for an array of 61 cores in hexagonal arrangement with R=0.4, D=0.2, a resolution of N=1000 and transverse and longitudinal calculation steps of Δ=0.02 and ΔZ=0.01 respectively. Figure 32(b) is n(X,Y).

Figure 32(a) is a magnified image of the optical intensity that demonstrates spots of light in some cores. As expected, the optical field is coupled among cores as it propagates because the cores are very close to each other. The phase of the vortex field with charges of +1 or -1 is also shown in Figure 32(c).

As stated before, the topological charge should be always conserved when new optical vortices are formed and then annihilated in pairs with opposing charges. In this case, conservation is confirmed as 7*(+1)+6*(-1)=+1 where there are 7 vortices with +1 charge and 6 vortices with -1 charge.

Figure 32(d) shows the interferogram of the vortex beam with a plane wave reference at π/4 with respect to the X axis. The dislocation points of new optical vortices are found at comparable locations to that shown in Figure 32(c).

In addition, Figure 33 shows the propagated optical vortex field at Z=8 for 127 cores array with R=0.4, D=0.2, a resolution of N=1000 with Δ=0.016 and ΔZ=0.005. Figure 33(b) shows n(X,Y) and Figure 33(a) is a magnified image of the optical field intensity with the spots of light spread in more near cores compared to the case shown in Figure 32(b). The phase of the field from $-\pi$ to π is also shown as a magnified image in Figure 33(c) with new pairs of vortices around the vortex at the origin which confirm the conservation of charge.

In addition, Figure 33(*d*) shows the interferogram with a plane wave reference at $\pi/4$ with respect to the X axis that shows the points of dislocations for each new vortex.

**Table 8** New vortices at various Z's for R=0.4 and D=0.2 (polarities are in parentheses).

Z	37 cores	61 cores	91 cores	127 cores
0.0	1(+1)	1(+1)	1(+1)	1(+1)
1.0	9(+5,-4)	11(+6,-5)	17(+9,-8)	23(+12,-11)
2.0	13(+7,-6)	23(+12,-11)	37(+19,-18)	43(+22,-21)
3.0	15(+8,-7)	25(+13,-12)	35(+18,-17)	41(+21,-20)
4.0	15(+8,-7)	25(+13,-12)	37(+19,-18)	41(+21,-20)
5.0	27(+14,-13)	33(+17,-16)	41(+21,-20)	51(+26,-25)
6.0	23(+12,-11)	31(+16,-15)	39(+20,-19)	51(+26,-25)
7.0	23(+12,-11)	33(+17,-16)	37(+19,-18)	53(+27,-26)
8.0	25(+13,-12)	37(+19,-18)	49(+25,-24)	55(+28,-27)
9.0	27(+14,-13)	37(+19,-18)	49(+25,-24)	55(+28,-27)
10.0	31(+16,-15)	39(+20,-16)	51(+26,-25)	59(+30,-29)
11.0	29(+15,-14)	43(+22,-21)	51(+26,-25)	59(+30,-29)
12.0	33(+17,-16)	39(+20,-19)	49(+25,-24)	59(+30,-29)
13.0	39(+20,-16)	43(+22,-21)	57(+29,-28)	65(+33,-32)
14.0	39(+20,-16)	49(+25,-24)	61(+31,-30)	71(+36,-35)
15.0	47(+24,-23)	55(+28,-27)	61(+31,-30)	73(+37,-36)
16.0	47(+24,-23)	55(+28,-27)	67(+34,-33)	75(+38,-37)
17.0	49(+25,-24)	61(+31,-30)	73(+37,-36)	77(+39,-38)
18.0	53(+27,-26)	61(+31,-30)	73(+37,-36)	81(+41,-40)
19.0	57(+29,-28)	69(+35,-34)	77(+39,-38)	93(+47,-46)
20.0	63(+32,-31)	71(+36,-35)	91(+46,-45)	97(+49,-48)

As before, the method for generation of Figures 32 and 33 is used to examine the creation of new vortices with respect to Z when the number of cores, core radius R and distance D are modified. Several results are listed in Table 8 for Z from 0.0 to 20.0 when the number of cores is 37, 61, 91 and 127 respectively and at R=0.4 and D=0.2. Polarities (both + or -) of new vortices are also recorded in Table 8 to demonstrate and verify the conservation of charge.

As shown in Figure 33, the creation of new vortices is highly dynamic with respect to Z and the number of cores. Propagating further, vortices are formed proportional to the number of cores. As in former cases, new vortices could not survive continually and might vanish while other new vortices are generated in other sites.
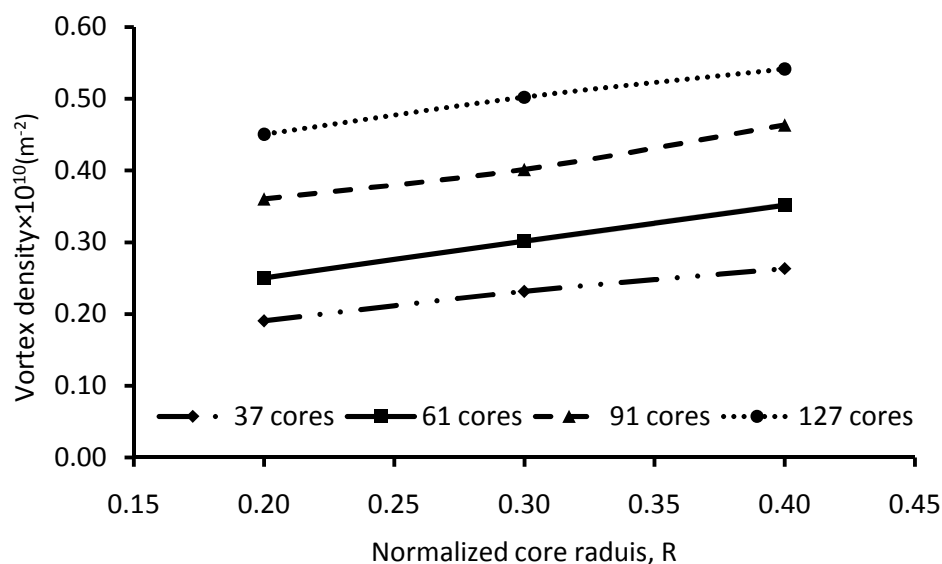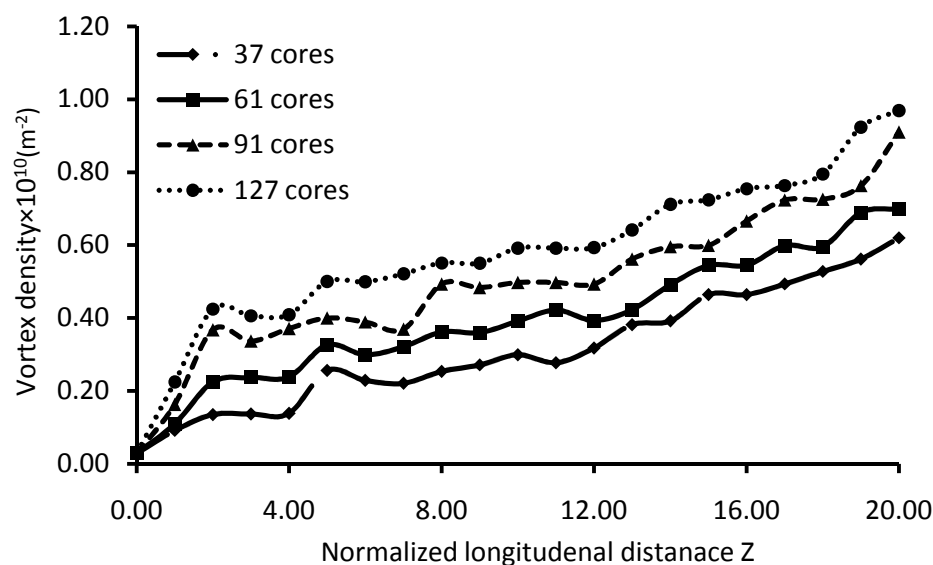

Figure 34 vortex density with respect to Z for different number of cores for n_{core}=1.5, $n_{cladding}$=1.495, R=0.4 and D=0.2.

As shown in Table 8, the longitudinal distance at Z=8.0 illustrates the trend for the number of new vortices as the number of cores is changed. Core radius also have an effect on the number of generated vortices as listed in Table 9 and presented as vortex density in Figure 35 for various R at Z=8.0 and D=0.2 with the same number of cores. Figure 35 confirms a tendency of the increase in the number of vortices (or vortex density) as the core radius increases.

Table 9 New vortices at various R's for Z=8.0 and D=0.2 (polarities are in parentheses).

R	37 cores	61 cores	91 cores	127 cores
0.2	21(+11,-10)	31(+16,-15)	41(+21,-20)	51(+26,-25)
0.3	23(+12,-11)	33(+17,-16)	45(+23,-22)	53(+27,-26)
0.4	25(+13,-12)	37(+19,-18)	49(+25,-24)	55(+28,-27)
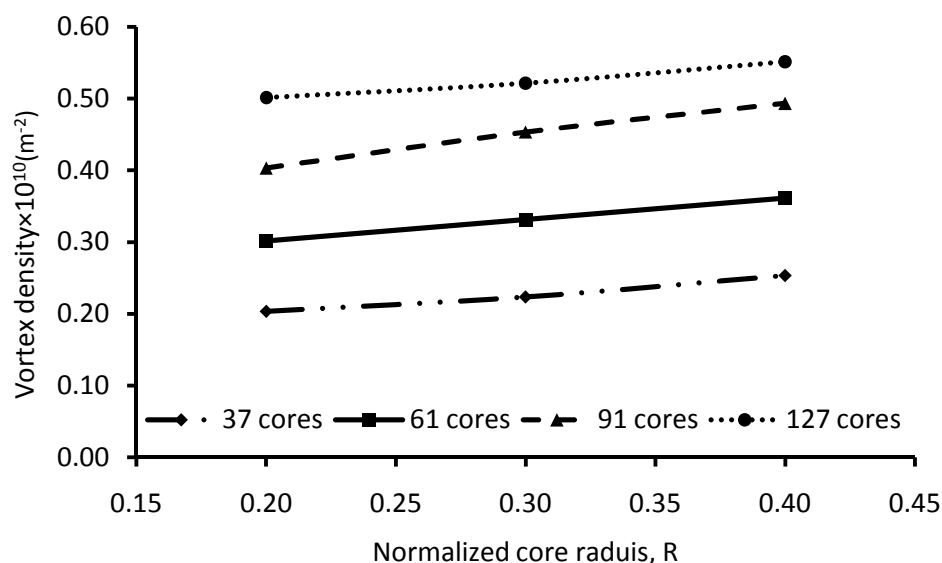
Figure 35 Vortex density with respect to R for different number of cores for n_{core}=1.5,

$n_{cladding}$=1.495, Z=8.0 and D=0.2.

Table 10 New vortices at various D's for Z=8.0 and R=0.4 (polarities are in parentheses).

D	37 cores	61 cores	91 cores	127 cores
0.2	25(+13,-12)	37(+19,-18)	49(+25,-24)	55(+28,-27)
0.3	23(+12,-11)	33(+17,-16)	45(+23,-22)	53(+27,-26)
0.4	21(+11,-10)	31(+16,-15)	41(+21,-20)	51(+26,-25)

In addition, variation of the distance between cores could affect the number of new vortices as listed in Table 10 and presented as vortex density in Figure 36 for various D for R=0.4 and Z=8.0. Figure 36 confirms the tendency of the decrease in the number of vortices as the distance between cores increases.
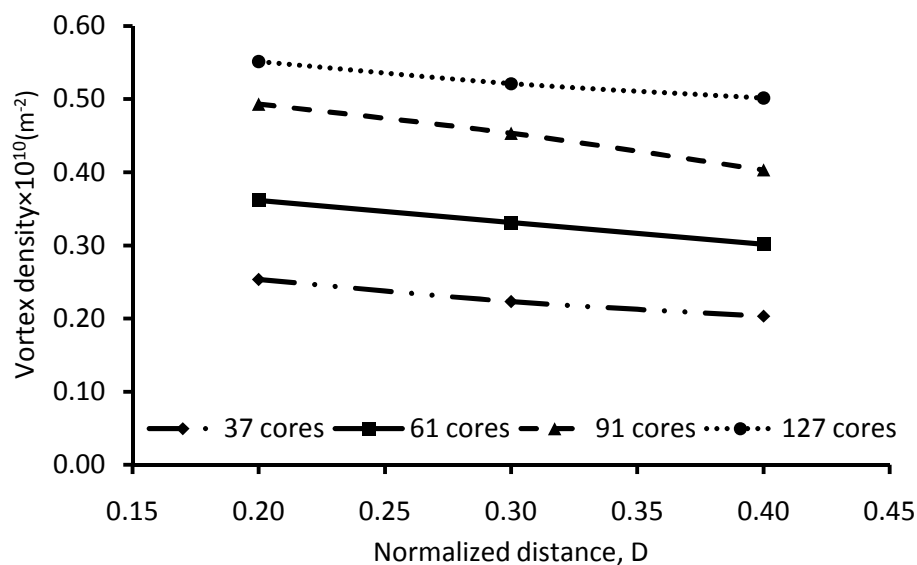
Figure 36 Vortex density with respect to D for different number of cores for n_{core}=1.5,

$n_{cladding}$=1.495, Z=8.0 and R=0.4.

5.4 Phase effects

In order to study the generation of new vortices in linear and nonlinear arrays, several image sequences were built for both the intensity and the phase. At Z=10, Figures 37 and 38 present these image sequences for 127 linear and nonlinear cores respectively.

The array shown in Figures 37 and 38 are for 127 cores with a normalized radius of R=0.4 and a normalized distance of D=0.2. Calculations are performed for a beam width of w_0=5μm and a wavelength of λ=1.5μm. A sequence of six images of the field intensity and phase are shown in Figure 37 for the linear array in order to trace the formation of new vortices. As the optical field propagates inside the array, mode coupling between the cores occurs and several points of zero intensity are created.

The rotation of the phase and its spiral progression along the direction of

propagation can generate local phase change around some points of zero intensity resulting in the creation of new vortices. Since the optical coupling among the cores is very dynamic with many variations along the direction of propagation, the locations of points of zero intensity are also changed accordingly. Any further effects of the phase rotation around the new locations of the zero intensity points will generate new vortices at new locations. On that basis, previously appearing vortices are vanished as a result of these modifications and vortices are usually generated at the core boundaries.

The behavior of the optical vortex propagation in a nonlinear array shown in Figure 38 is found to be similar to Figure 37 for a positive nonlinearity of $n_2 I_0$=0.0001 and Δn=0.005. Similarities are explained before based on Figures 29 and 34 that demonstrate the unstable trend for the formation of new vortices. Unstable means that new vortices tend to change or collapse continually as the original optical vortex field remains at the center. Changes in the number of new vortices and their locations in the transverse plane have been observed. By contrast, the original vortex, as shown in Figures 37 and 38, keeps its location and charge as it propagates in the optical array. Variations are obvious in the surroundings with changes in newly formed vortices locations while the total charge is conserved.

The sequence of images shown in Figures 39 and 40 are for an off-center vortex started at X=Y=1.0 for 127 cores with R=0.4 and D=0.2. The vortex is actually located at the next core with n_{core}=1.5. Computations are performed for a beam width of w_0=5μm and a wavelength of λ=1.5μm for comparisons to Figures 37 and 38. Figure 39 illustrates the intensity and phase sequences of images for the vortex propagation in the linear array that indicates continuous spawning of new vortices.

Intensity Sequence, X:-10 to 10, Y:-10 to 10   Phase Sequence, X:-10 to 10, Y:-10 to 10

Z=10.0

Original vortex

Z=10.1

New vortices

Z=10.2

Z=10.3

Z=10.4

Original vortex in same position

Z=10.5
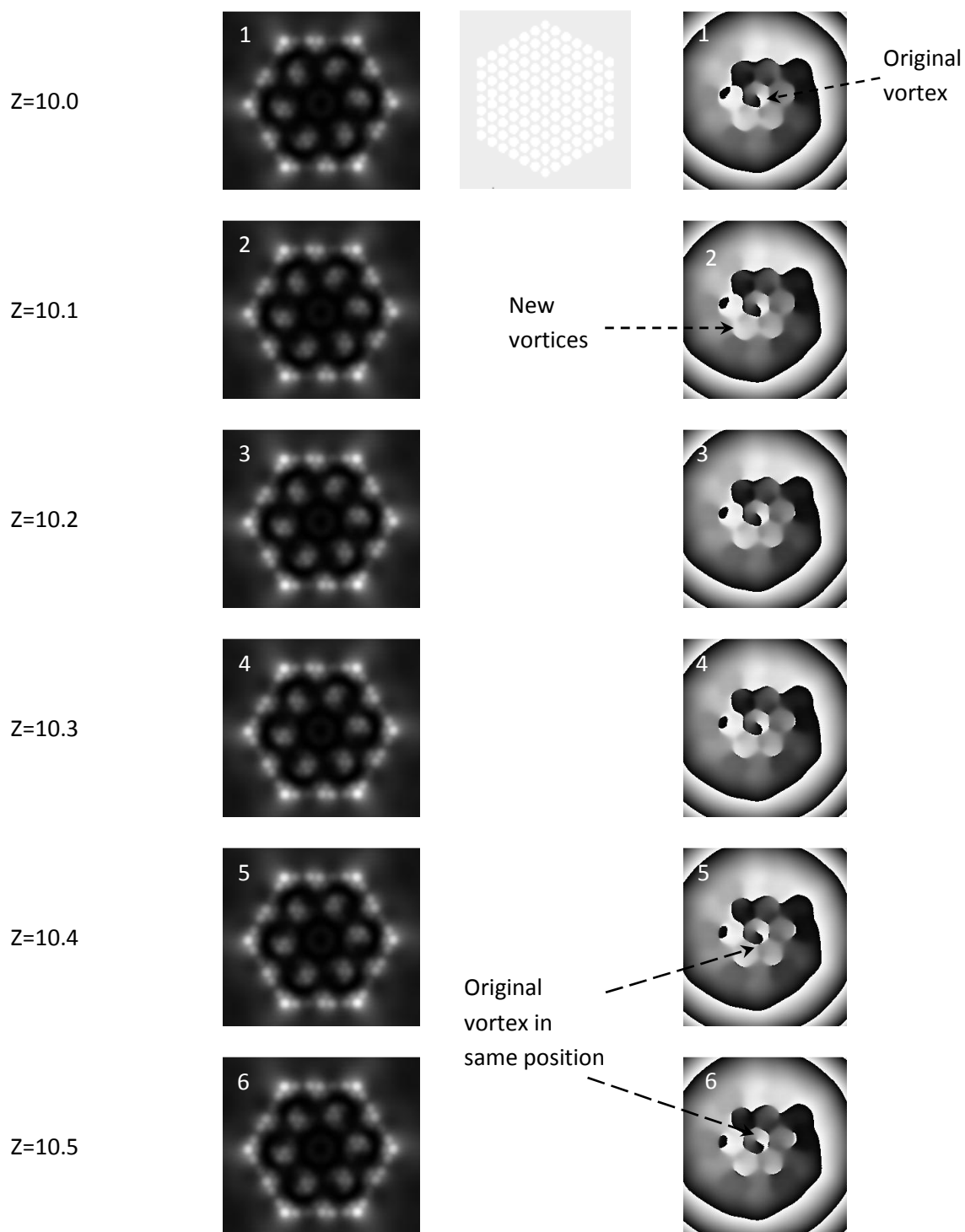
Figure 37 Image sequences for the creation of vortices in a 127 linear cores for n_{core}=1.5,

$n_{cladding}$=1.495, Z=10, R=0.4 and D=0.2.

Intensity Sequence, X:-10 to 10, Y:-10 to 10   Phase Sequence, X:-10 to 10, Y:-10 to 10

Z=10.0

Original vortex

Z=10.1

Z=10.2

New vortices

Z=10.3

Z=10.4

Original vortex in same position

Z=10.5

Figure 38 Image sequences for the creation of vortices in 127 non-linear cores for n_{core}=1.5,

$n_{cladding}$=1.495, Z=10, R=0.4 and D=0.2.

Intensity Sequence, X:-10 to 10, Y:-10 to 10   Phase Sequence, X:-10 to 10, Y:-10 to 10

Z=1.0

Z=5.0

Z=7.5

Z=10.0

Z=15.0

Z=20.0

Original vortex

New vortices

Original vortex in a different position

Figure 39 Image sequences for a 1.0 off-center vortex in 127 linear cores for n_{core}=1.5,

$n_{cladding}$=1.495, Z=10, R=0.4 and D=0.2.

Intensity Sequence, X:-10 to 10, Y:-10 to 10   Phase Sequence, X:-10 to 10, Y:-10 to 10

Z=1.0

Original vortex

Z=5.0

Z=7.5

Z=10.0

New vortices

Z=15.0

Original vortex in a different position

Z=20.0

Figure 40 Image sequences for a 1.0 off-center vortex in 127 non-linear cores for n_{core}=1.5,

$n_{cladding}$=1.495, Z=10, R=0.4 and D=0.2.

The off-set vortex has returned its position to the central core due to field coupling among the cores but keeps the same charge. Additional new vortices are also generated around the original vortex as it relocates. Similar results are noticed in Figure 40 for the nonlinear array with a positive nonlinearity of n_2I_0=0.0001 and Δn=0.005.

As a vortex propagates in the waveguide, points of zero intensity are first generated due to optical field coupling among the cores. The spiral influences of the original vortex phase and its rotation property may create additional new vortices at those points. All vortices, including the original one, exhibit constant change in their behavior on the transverse plane where their positions vary repeatedly in X and Y coordinates.

In both Figures 39 and 40, the formation of new vortices is noticed at Z=7.5 under the influences of the phase and the structure modulation. Intensity and phase changes are only observed inside the array as a consequence of the variations of the spatial frequency due to Δn=0.005. More new vortices are produced at Z=10, 15 and 20 respectively. The intensity of light is not symmetric with respect to the array structure as shown in the intensity image sequence of Figures 39 and 40. This situation is enhanced by repeated internal reflections among the cores in addition to coupling and results in a bouncy vortex unlike the case shown in Figures 37 and 38 above.

More investigations on the off-center vortex field are presented in Figures 41, 42 and 43 for X=Y=0.5 and Figures 44, 45 and 46 for X=Y=0.3 respectively for w_0=5μm and λ=1.5μm. Linear propagation in an array with R=0.4 and D=0.2 where the vortex is first located between cores at X=Y=0.5 is shown as image sequences in Figure 41 for Z=1, 5, 7.5, 15 and 20. The optical vortex started to couple to the central core near Z=7.5 and new vortices began to form around it at longer distances.

Intensity Sequence, X:-10 to 10, Y:-10 to 10   Phase Sequence, X:-10 to 10, Y:-10 to 10

Z=1.0

Original vortex

Z=5.0

Z=7.5

Z=10.0

New vortices

Z=15.0

Original vortex in a different position

Z=20.0
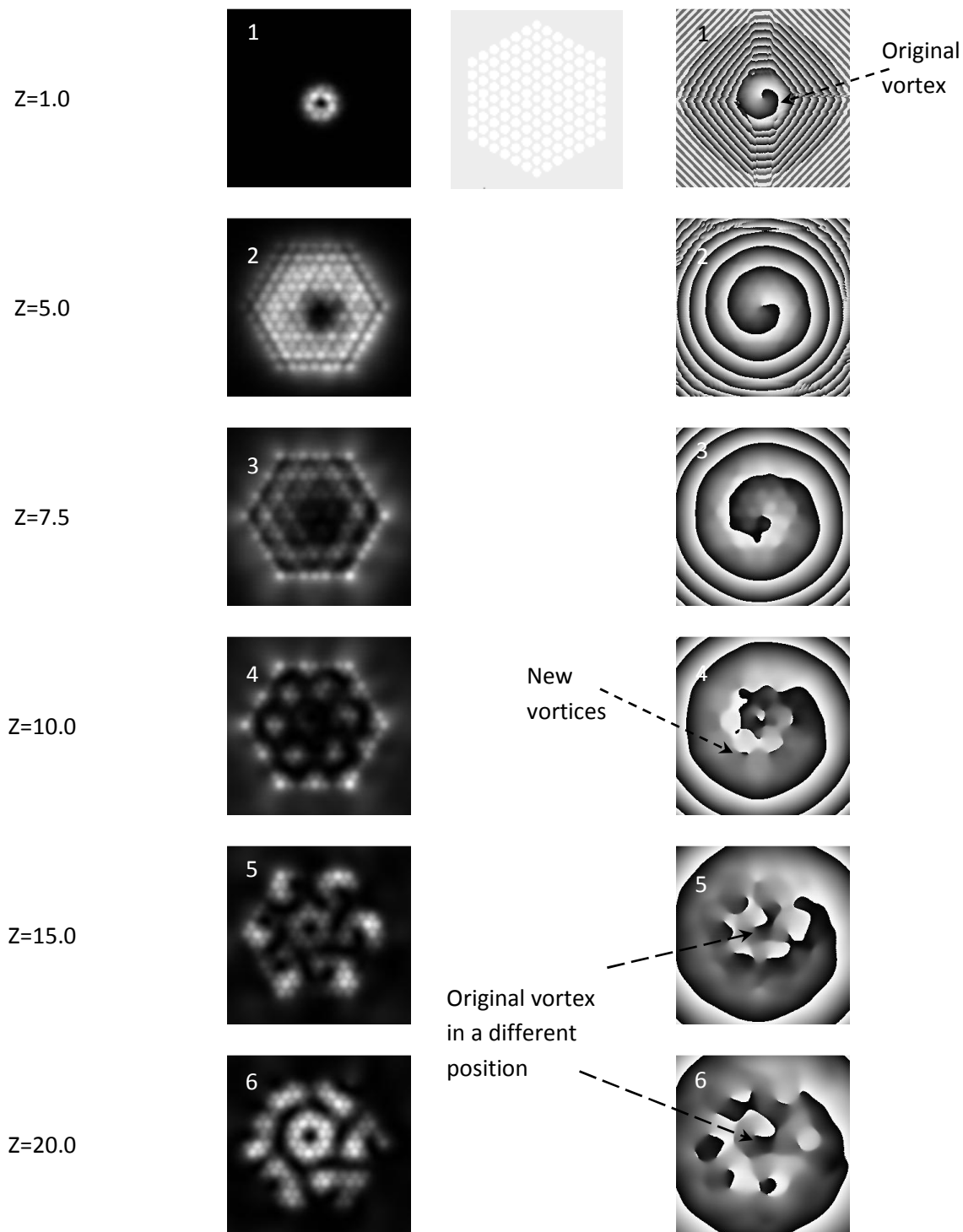
Figure 41 Image sequences for a 0.5 off-center vortex in 127 linear cores for n_{core}=1.5, $n_{cladding}$=1.495, Z=10, R=0.4 and D=0.2.

Intensity Sequence, X:-10 to 10, Y:-10 to 10   Phase Sequence, X:-10 to 10, Y:-10 to 10

Z=1.0

Z=5.0

Z=7.5

Z=10.0

Z=15.0

Z=20.0

Original vortex

New vortices

Original vortex in a different position

Figure 42 Image sequences for a 0.5 off-center vortex in positive 127 non-linear cores for

n_{core}=1.5, $n_{cladding}$=1.495, Z=10, R=0.4 and D=0.2.

Intensity Sequence, X:-10 to 10, Y:-10 to 10   Phase Sequence, X:-10 to 10, Y:-10 to 10
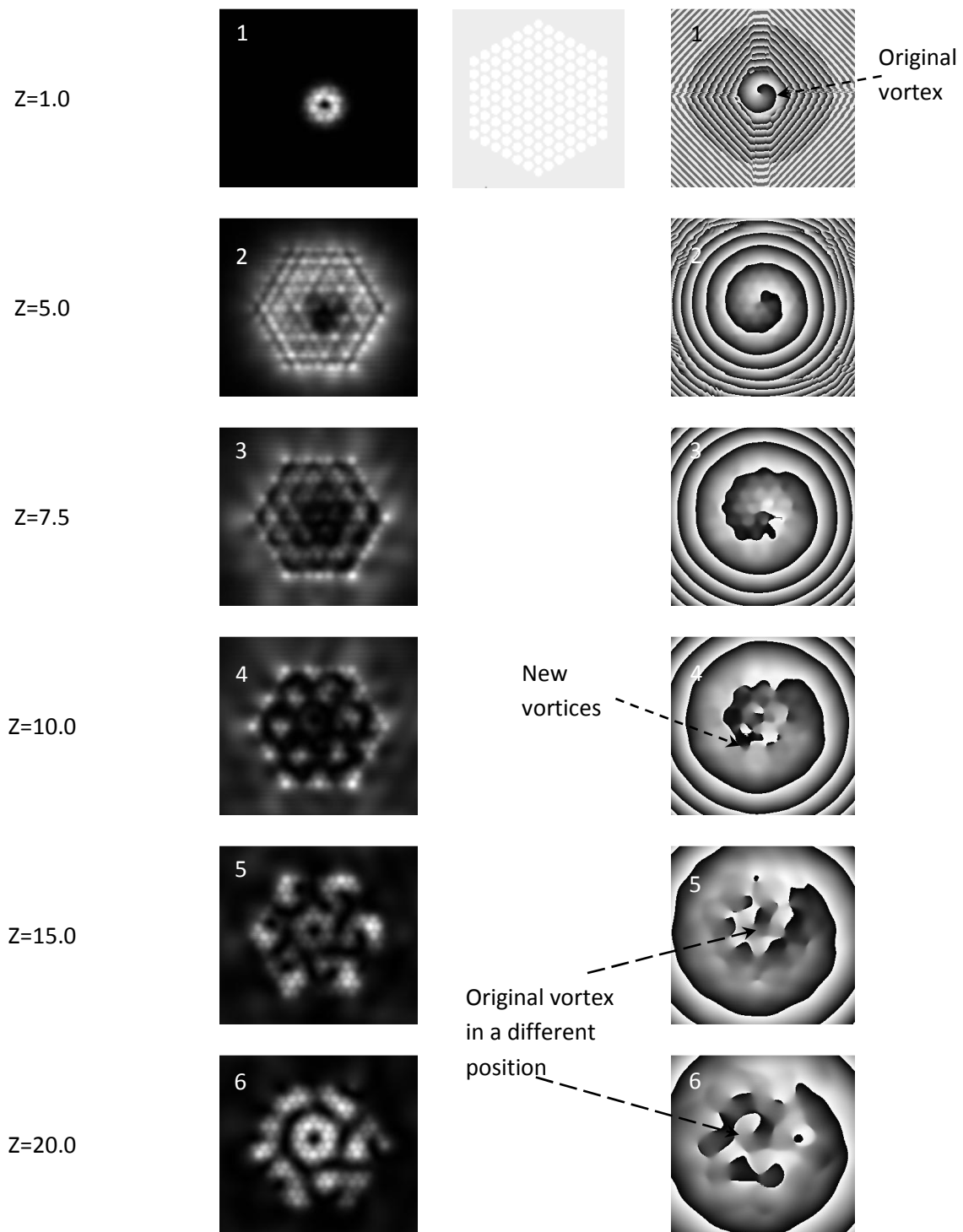
Figure 43 Image sequences for a 0.5 off-center vortex in negative 127 non-linear cores for

n_{core}=1.5, $n_{cladding}$=1.495, Z=10, R=0.4 and D=0.2.

Intensity Sequence, X:-10 to 10, Y:-10 to 10   Phase Sequence, X:-10 to 10, Y:-10 to 10

Z=1.0

Original vortex

Z=5.0

Z=7.5

New vortices

Z=10.0

Z=15.0

Original vortex still in central core

Z=20.0

Figure 44 Image sequences for a 0.3 off-center vortex in 127 linear cores for n_{core}=1.5,

$n_{cladding}$=1.495, Z=10, R=0.4 and D=0.2.

Intensity Sequence, X:-10 to 10, Y:-10 to 10   Phase Sequence, X:-10 to 10, Y:-10 to 10

Z=1.0

Original vortex

Z=5.0

Z=7.5

Z=10.0

New vortices

Z=15.0

Original vortex still in central core

Z=20.0
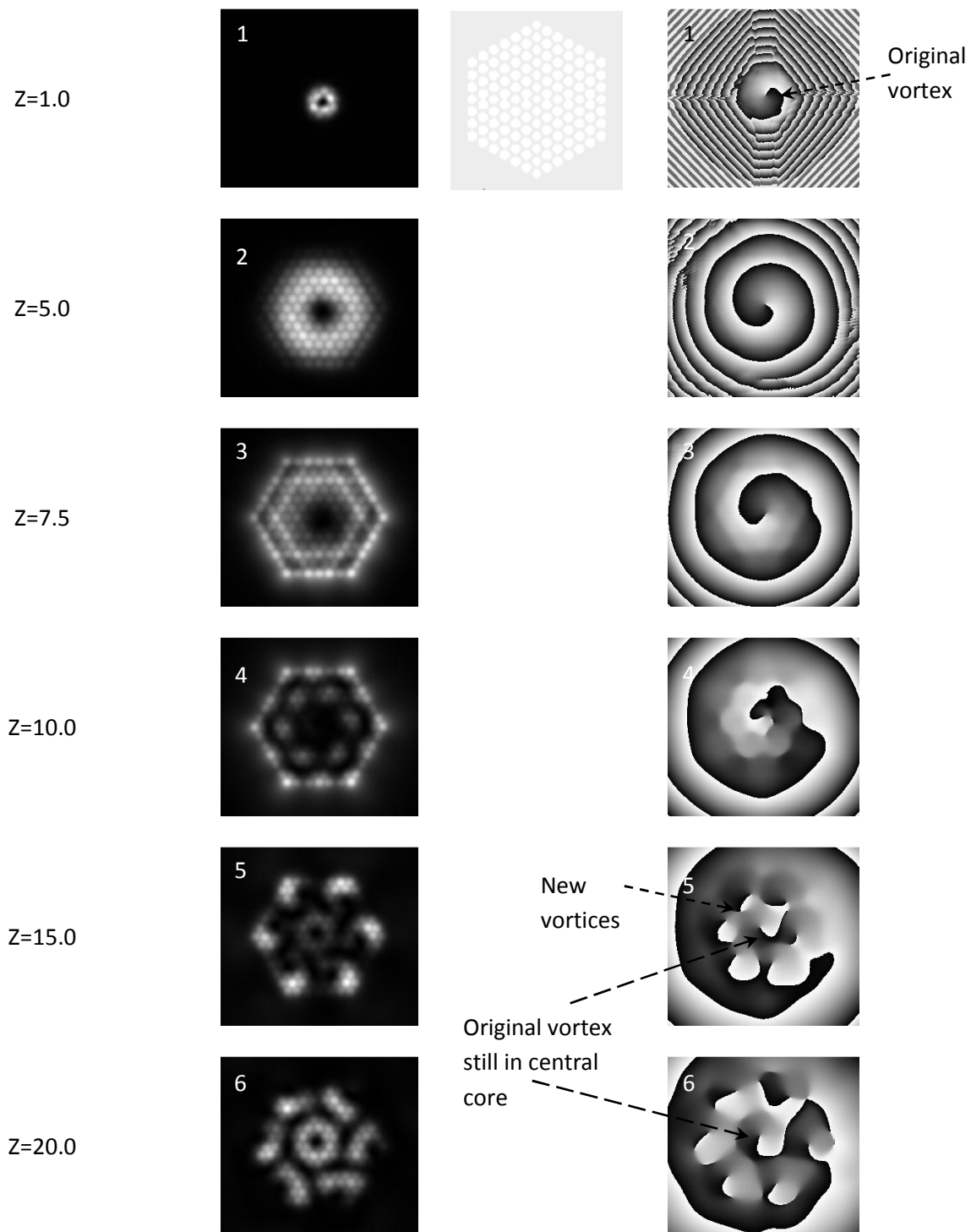
Figure 45 Image sequences for a 0.3 off-center vortex in positive 127 non-linear cores for

n_{core}=1.5, $n_{cladding}$=1.495, Z=10, R=0.4 and D=0.2.

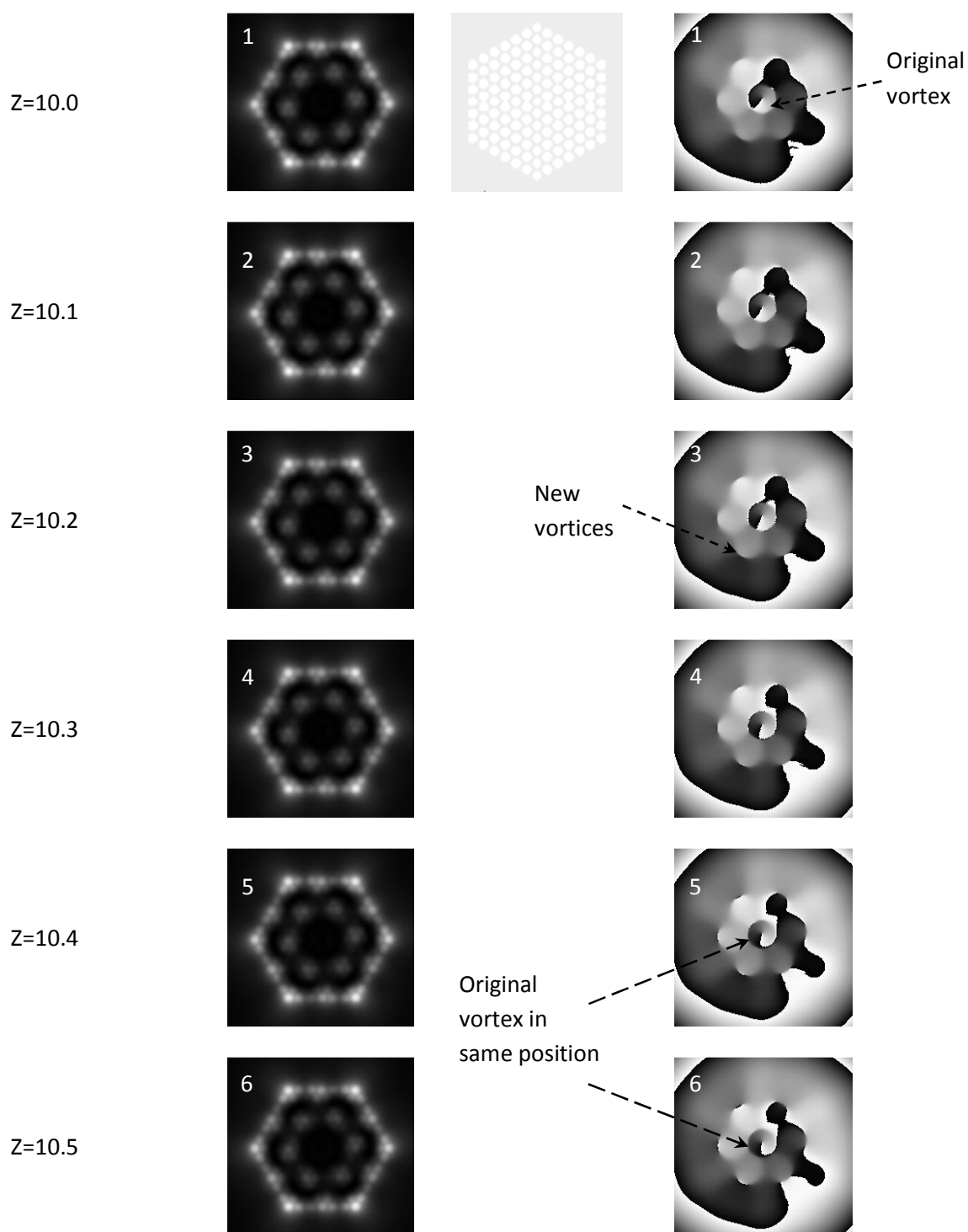Intensity Sequence, X:-10 to 10, Y:-10 to 10   Phase Sequence, X:-10 to 10, Y:-10 to 10

Z=1.0

Z=5.0

Z=7.5

Z=10.0

Z=15.0

Z=20.0

Original vortex

New vortices

Original vortex still in central core
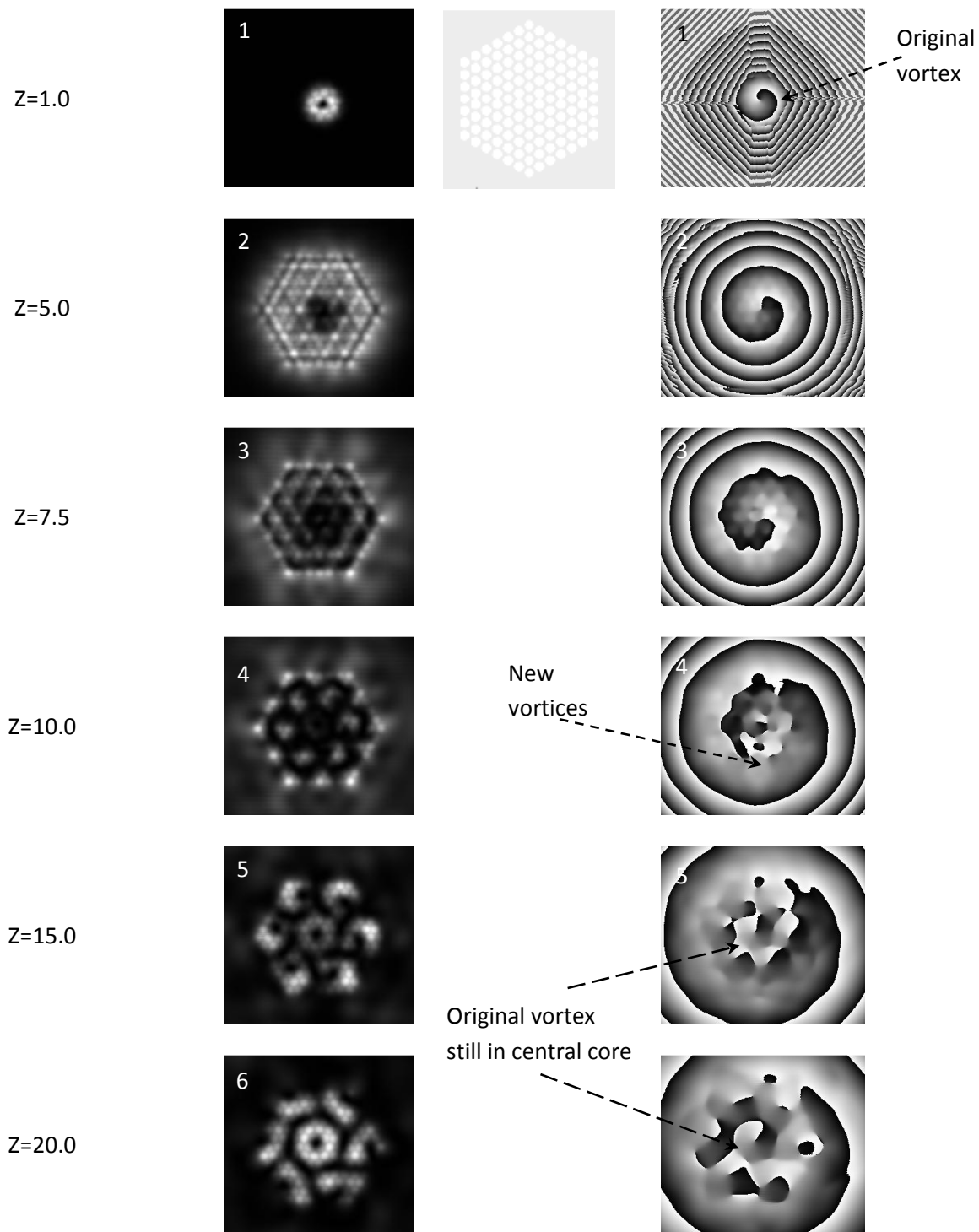
Figure 46 Image sequences for a 0.3 off-center vortex in negative 127 non-linear cores for

n_{core}=1.5, $n_{cladding}$=1.495, Z=10, R=0.4 and D=0.2.

The propagation of a vortex beam in a nonlinear array is shown in Figures 42 and 43 for n_2I_0=0.0001 and n_2I_0=-0.0001 respectively. Results similar to those of the linear array in Figure 41, however, are observed and new vortices are created as Z increases.

The situation where the vortex field is off-centered by X=Y=0.3 is shown in Figures 44, 45 and 46. The vortex is initially inside the central core but is shifted slightly from its central point. As illustrated in these Figures, the vortex re-positions itself to the center of the central core at certain Z for both linear and nonlinear cases. As the propagation distance increases, the original vortex does not change its location with respect to the array structure. New vortices are created in the same process as discussed earlier where points of zero intensity are first formed due to light coupling and then the phase rotation interacts to generate vortices at these locations.

As discussed earlier, when the original vortex field starts inside the central core, it continues to propagate inside that core. In spite of that, new vortices are dynamically generated in pairs away from the central core at different locations near core boundaries on the transverse plane.

In addition, when the vortex field starts in a different core other than the central one, it never couples to the central core but keeps changing its location inside other cores as it propagates in the optical array. A critical starting point could be at the exact boundary of the central core. Figures 47 and 48 demonstrate the propagation and coupling dynamics of an optical vortex when it is first positioned at the central core boundary for a linear and nonlinear array respectively for w_0=5μm and λ=1.5μm.

Intensity Sequence, X:-10 to 10, Y:-10 to 10   Phase Sequence, X:-10 to 10, Y:-10 to 10

Z=5.0

Z=7.5

Z=8.5

Z=10.0

Z=15.0

Z=20.0

Original vortex

New vortices

Original vortex coupled to central core
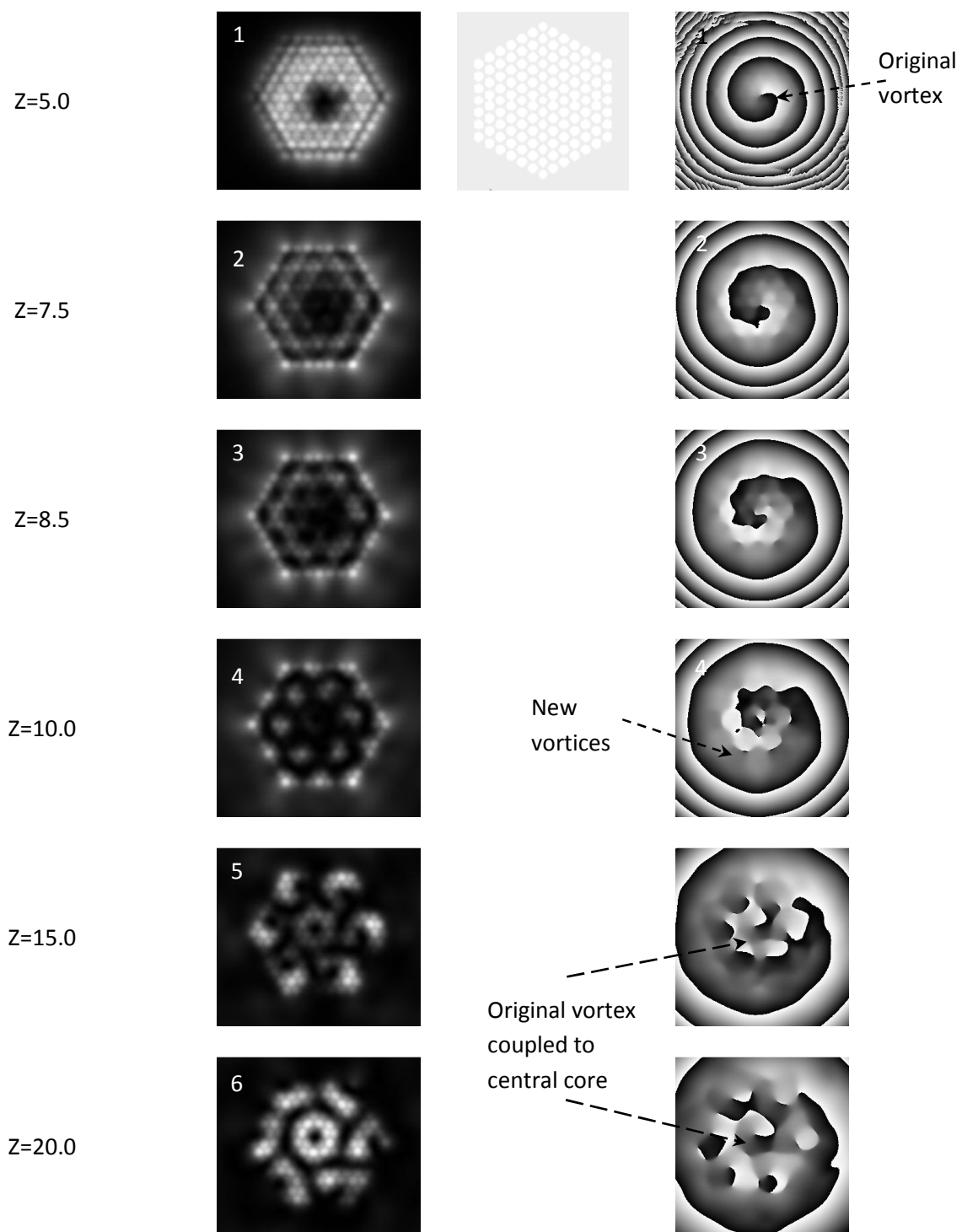
Figure 47 Image sequences for a vortex at the central core boundary in 127 linear cores for

n_{core}=1.5, $n_{cladding}$=1.495, Z=10, R=0.4 and D=0.2.

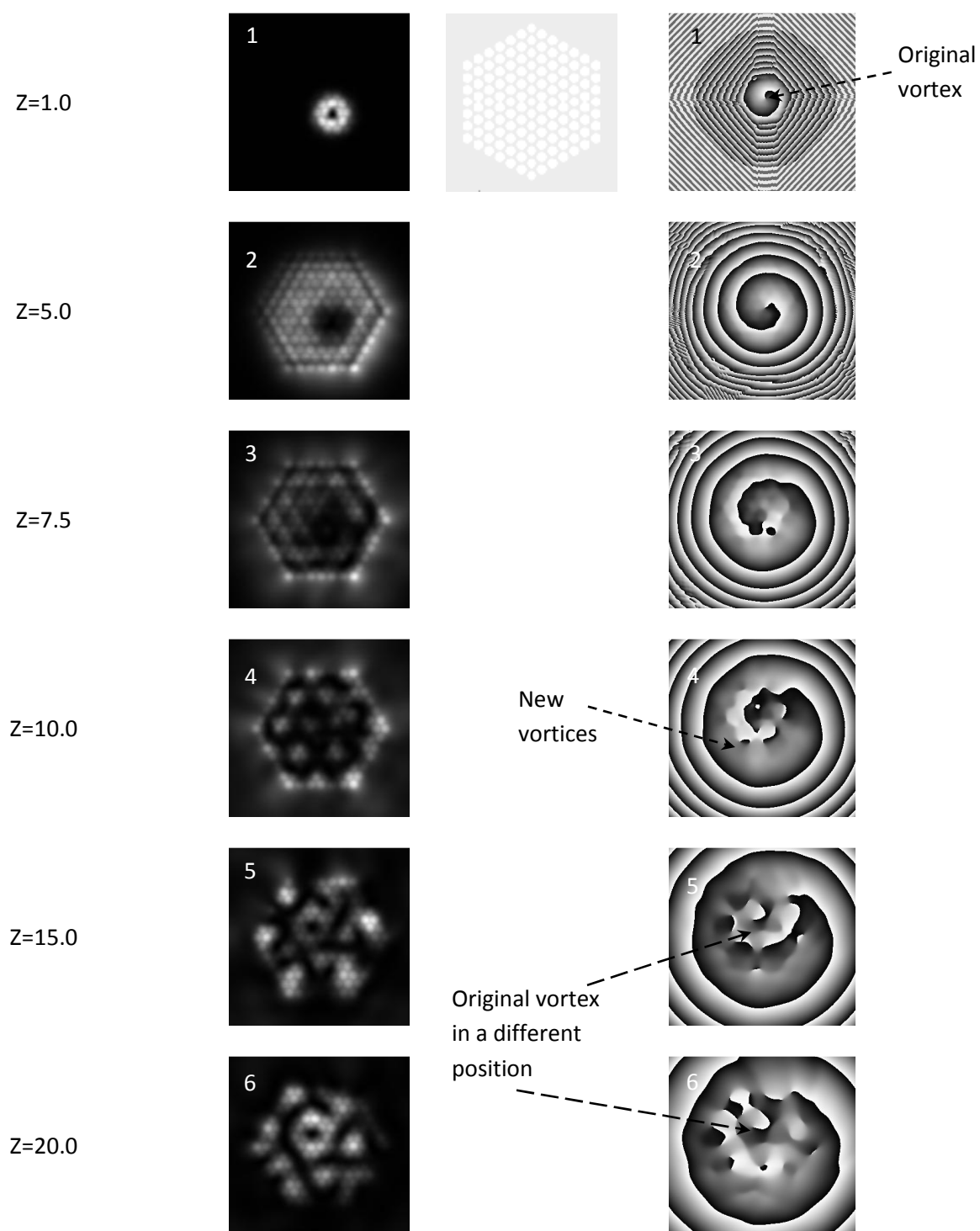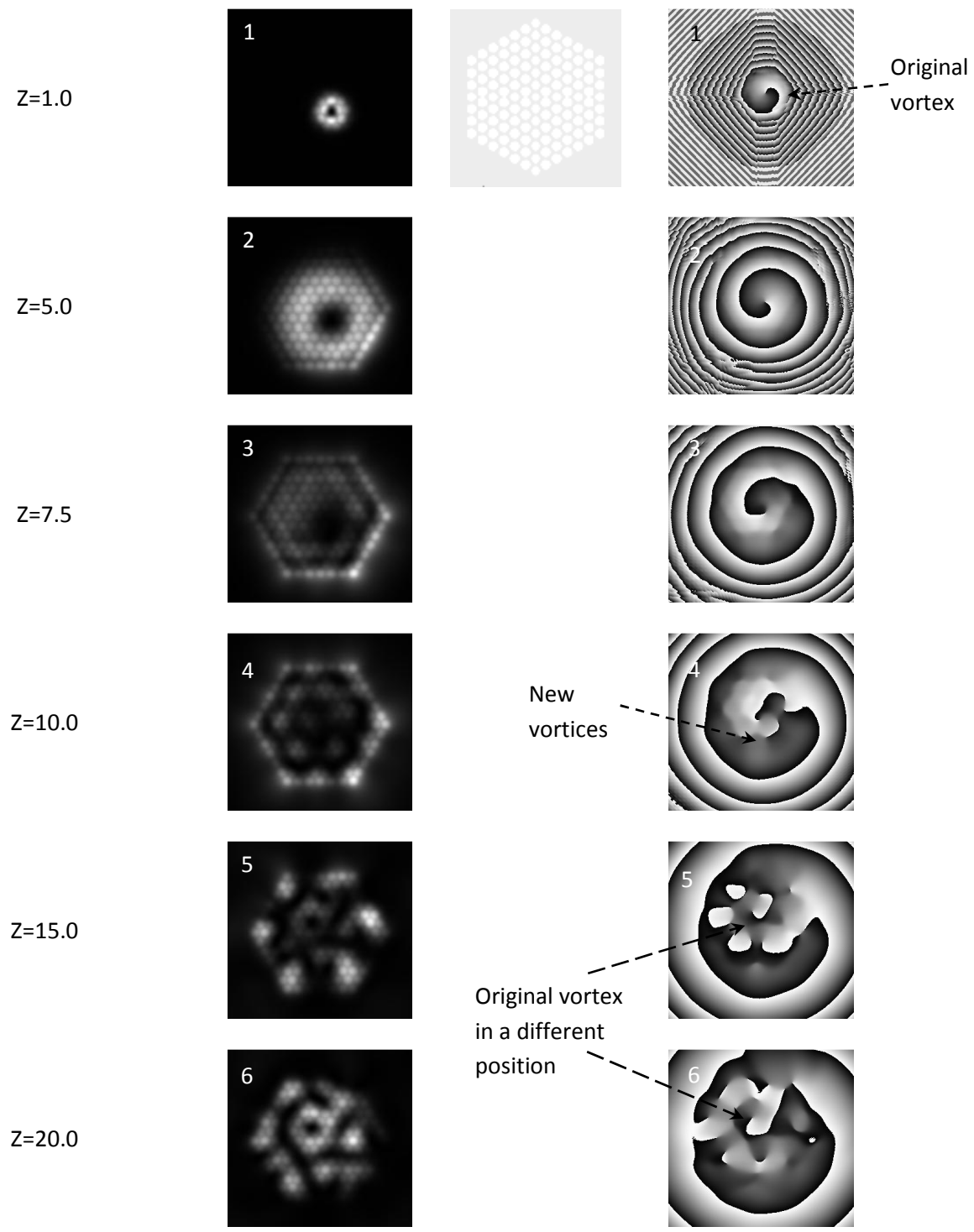Intensity Sequence, X:-10 to 10, Y:-10 to 10   Phase Sequence, X:-10 to 10, Y:-10 to 10

Z=5.0

Original vortex

Z=7.5

Z=10.0

Z=12.0

New vortices

Z=15.0

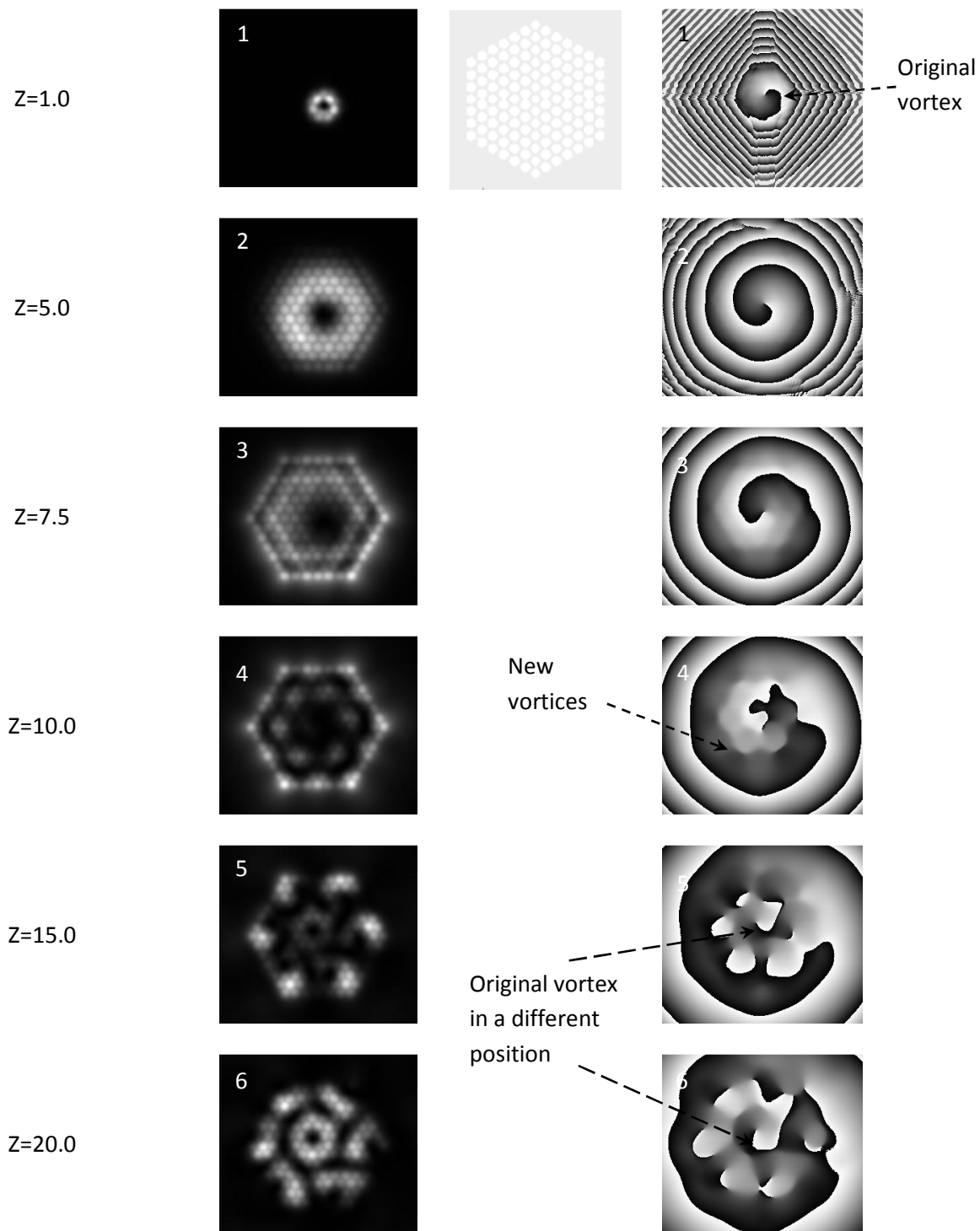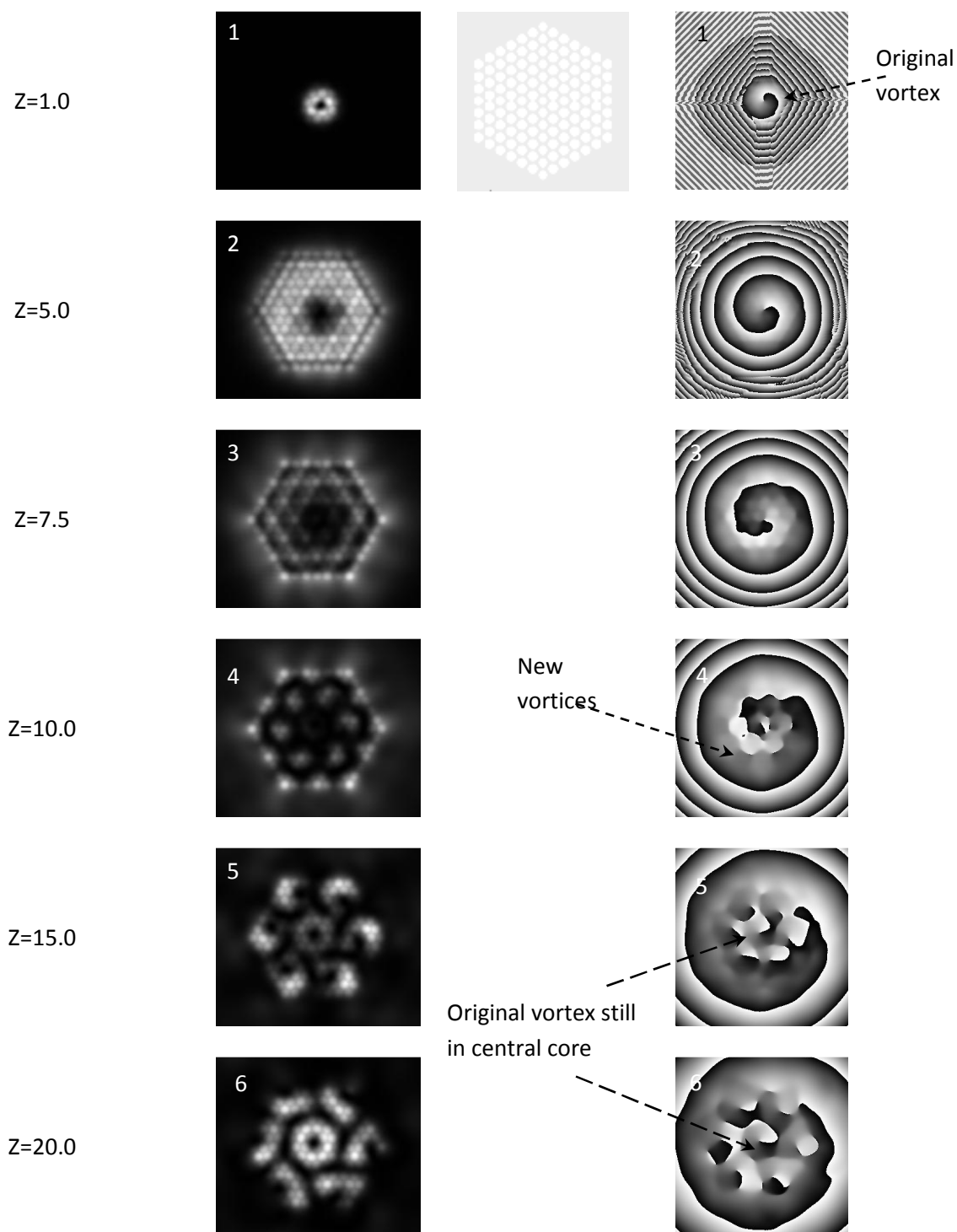Original vortex coupled to central core

Z=20.0
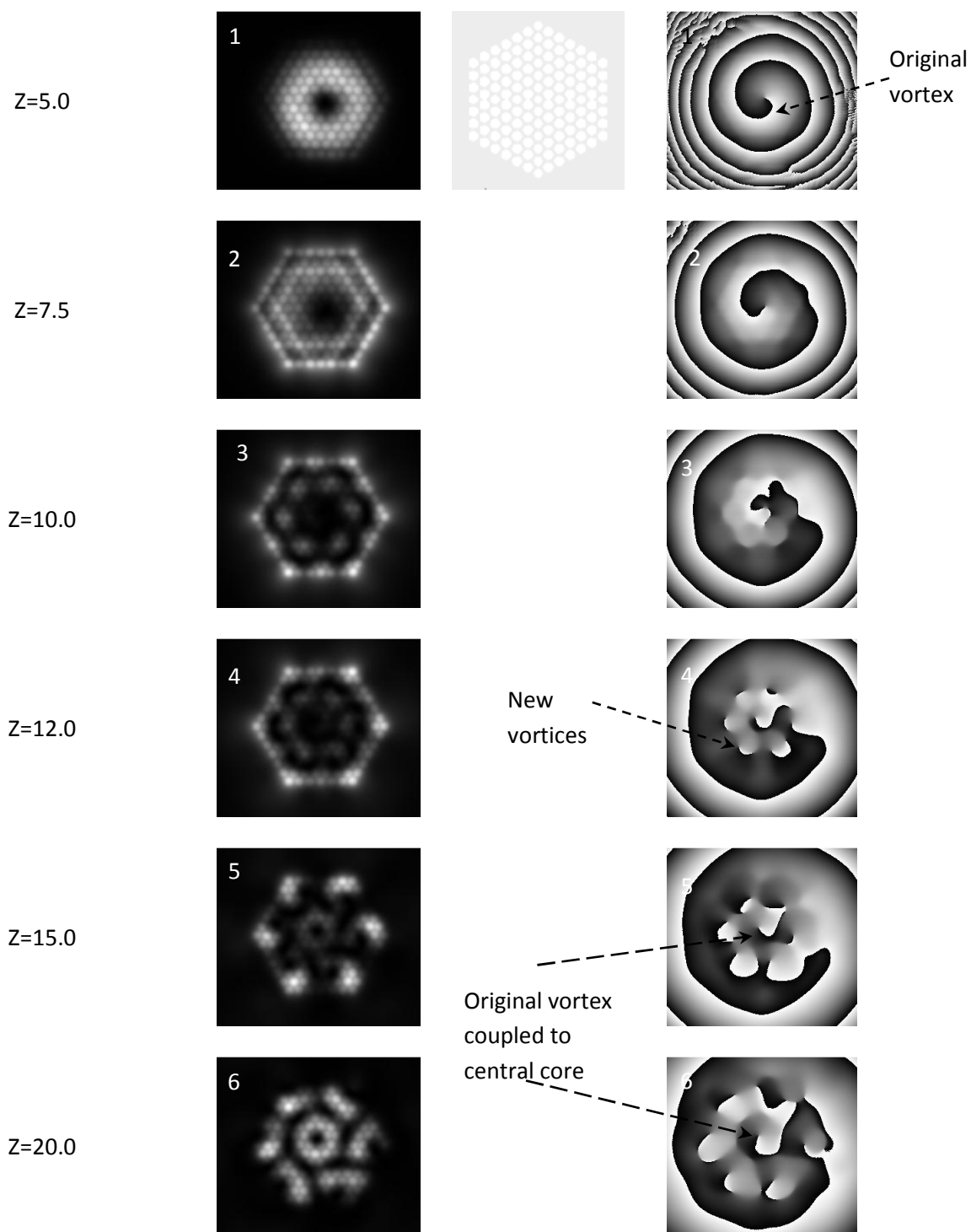
Figure 48 Image sequences for a vortex at the central core boundary in 127 non-linear cores for

n_{core}=1.5, $n_{cladding}$=1.495, Z=10, R=0.4 and D=0.2.

The image sequence shown in Figure 47 is from a simulation for a linear array of 127 cores in hexagonal arrangement with R=0.4 and D=0.2. Both the field intensity and the phase are shown at several Z points where the most important changes of the optical vortex are revealed. Intensity images exhibit the coupling of the propagating field among cores and display several points of zero intensity on the transverse plane. The phase images illustrate the coupling of the original vortex to the central core where it continues in that location without further changes. New vortices are also observed around the original one with repeated variations in their number and location.

In the linear array shown in Figure 47, the vortex started to couple to the central core at Z=8.5, whereas, it started to couple at Z=12.0 as shown in Figure 48 for the nonlinear array. The nonlinearity factor of the array could have a delaying effect on this type of vortex field coupling.

5.5   Statistical analysis

Fujikura image fiber is an optical waveguide containing a bundle array of several cores in a hexagonal arrangement [85]. The refractive index of each core and the refractive index of the cladding are n_{core}=1.5 and $n_{cladding}$=1.446 respectively. The radius of each core is r=1.45μm and the distance between cores is d=1.1μm or R=0.29 and D=0.22 respectively with normalization to w_0=5μm.

For statistical analysis, the radius of the cores is assumed to have a random change of ±10% as r±0.1r but maintain the same distance. The simulation code is run 100 times for each step in Z and the vortex density is then found for each run. The vortex density is defined as the number of vortices per fiber array area. The mean of the vortex density is

calculated and plotted versus Z with the standard deviation as error bars.
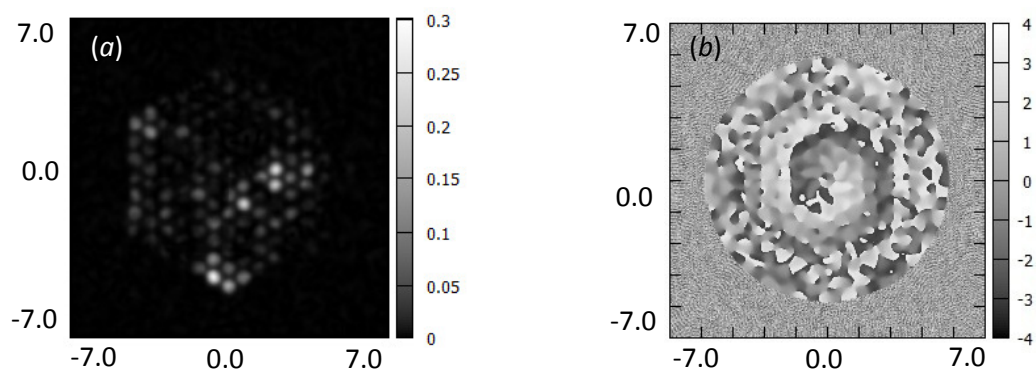
Figure 49 Intensity (*a*) and phase (*b*) in a linear array of 127 cores for n_{core}=1.5, $n_{cladding}$=1.446,
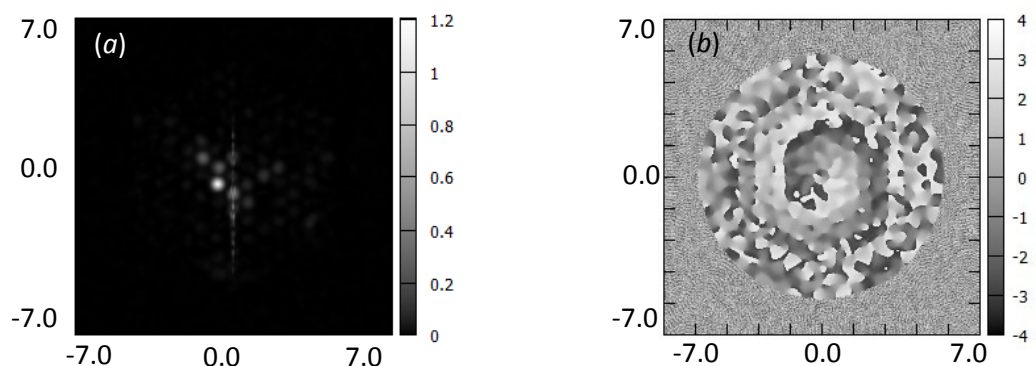
Z=10, R=0.29 and D=0.22.

Figure 50 Intensity (*a*) and phase (*b*) in a nonlinear array of 127 cores for n_{core}=1.5, $n_{cladding}$=1.446,

Z=10, R=0.29 and D=0.22.

Figure 49 shows the intensity and phase for a vortex at the center (0,0) and at Z=10 under a linear regime. Images are for a fiber array of 127 cores and a vortex beam with w_0=5μm and λ=1.5μm and the radius of the cores are $r\pm0.1r$ randomly. The propagation in a nonlinear array is shown in Figure 50 for n_2I_0=0.0001 with the same parameters as in Figure 49.

The computational area as shown from Figures 49 and 50 is $196w_0^2 = 4.9 \times 10^{-9} \text{m}^2$ or $14 \times 14 = 196$ normalized and $z_0 = \pi w_0^2 / \lambda = 5.236 \times 10^{-5}\text{m} = 52.36 \mu\text{m}$. In addition, the calculated mean is $\bar{x} = \sum_{i=1}^{n} x_i / n$, the variance is $s^2 = \sum_{i=1}^{n}(x_i - \bar{x})/n - 1$ and s is the standard deviation where n is the number of samples.
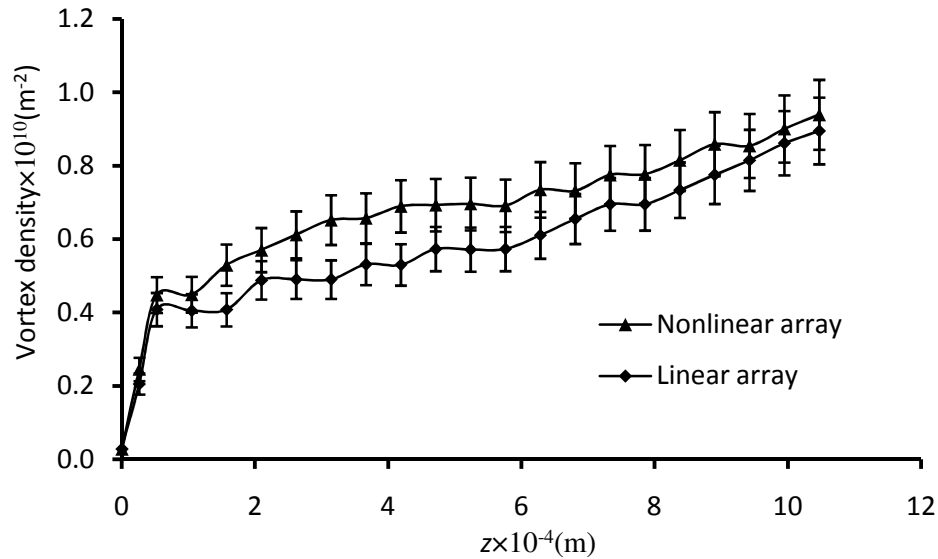
Figure 51 Statistical results of vortex density with respect to propagation distance Z for n_{core}=1.5, $n_{cladding}$=1.446, R=0.29 and D=0.22.

Statistical analysis results are shown in Figure 51 as the mean of the linear vortex density $v_{d,l}$ and nonlinear vortex density $v_{d,nl}$ in number per meters squared (m^{-2}) versus propagation distance z in meters (m). Linear and nonlinear results are shown with the standard deviation as error bars for number of samples n=100. Figure 51 indicates a continuous increase in vortex density with propagation distance. Propagation in a nonlinear array shows a little more vortex density with respect to distance compared to the linear array.

Linear regression analysis shows a positive slope with an increasing mean vortex density with propagation distance for a distance larger than 10^{-4}m. That is expressed as $([v_{d,l}]_z=0.057\times10^{14}z+0.364\times10^{10})$ and $([v_{d,nl}]_z=0.057\times10^{14}z+0.277\times10^{10})$ where $[v_{d,l}]_z$ and $[v_{d,nl}]_z$ are in m^{-2} and z is in meters.
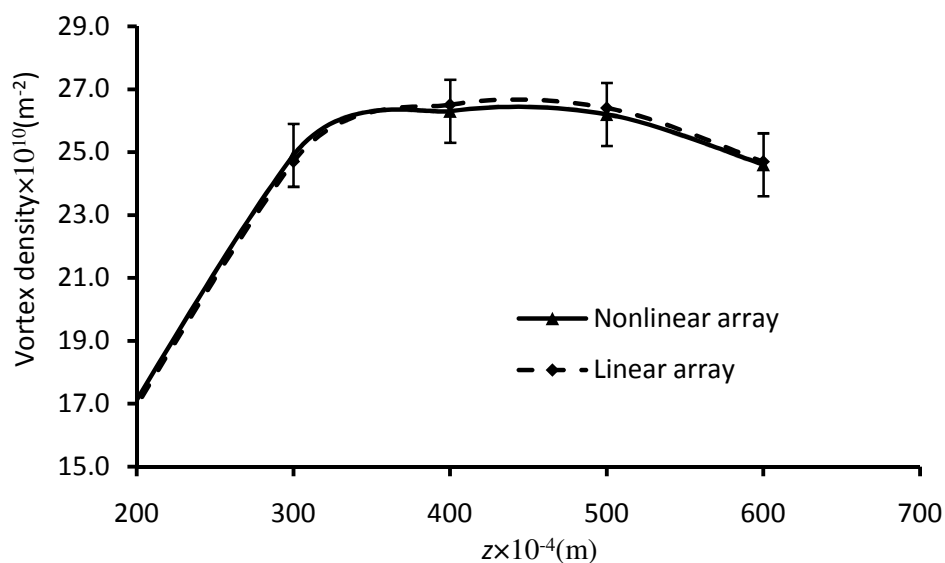
Figure 52 Statistical results of vortex density with saturation values for n_{core}=1.5, $n_{cladding}$=1.446, R=0.29 and D=0.22.

Table 11 Saturation data.

$z\times10^{-4}$(m)	300	400	500	600	
$v_{d,l}\times10^{10}$(m^{-2})	24.7	26.5	26.4	24.7	**Average** 25.575
$v_{d,nl}\times10^{10}$(m^{-2})	24.9	26.3	26.2	24.6	**Average** 25.5

As each vortex occupies a certain amount of space on the transverse plane, there should be an upper limit on the vortex number. The maximum number of vortices is approximately the total area of the transverse plane divided by the vortex area. For the case of Figure 51, the vortex radius size ranges from 0.3 to 0.7 (full width half maximum

of 0.6 to 1.4) normalized to the beam width $w_0=5\mu m$. The total area is almost 14^2 as shown in Figures 49 and 50 above. Thus, the maximum number of vortices ranges from $14^2/0.7^2{\sim}400$ to $14^2/0.3^2{\sim}2177$. As a result, the maximum mean vortex density ranges from $8.16{\times}10^{10}m^{-2}$ to $4.4{\times}10^{11}m^{-2}$ which is larger than the values shown in Figure 51. To reach these densities, z ranges from 0.0137m to 0.0772m according to the linear regression on page 91. Due to the huge number of steps for reaching this z, we limit the statistical analysis shown in Figure 52 to a smaller number of samples $n=5$ and find that the mean vortex density at saturation is approximately $25.0{\times}10^{10}m^{-2}$ for linear and nonlinear arrays when $z>0.035m$. The mean vortex density increases with respect to the propagation distance with almost the same slope shown in Figure 51 but then reaches its saturation between $400{\times}10^{-4}m$ and $500{\times}10^{-4}m$ as in Figure 52. The statistical results shown in Figures 51 and 52 are in acceptable agreement. Saturation data are listed in Table 11 where values decrease at some distance due to the annihilation of vortex pairs.
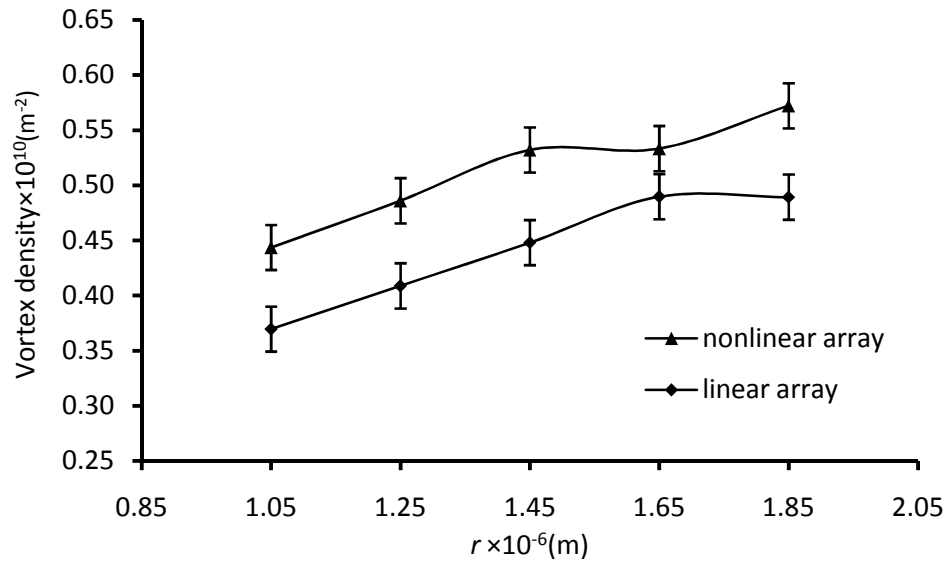
Figure 53 Statistical vortex density vs. radius for $n_{core}=1.5$, $n_{cladding}=1.446$, Z=10 and D=0.22±10%.
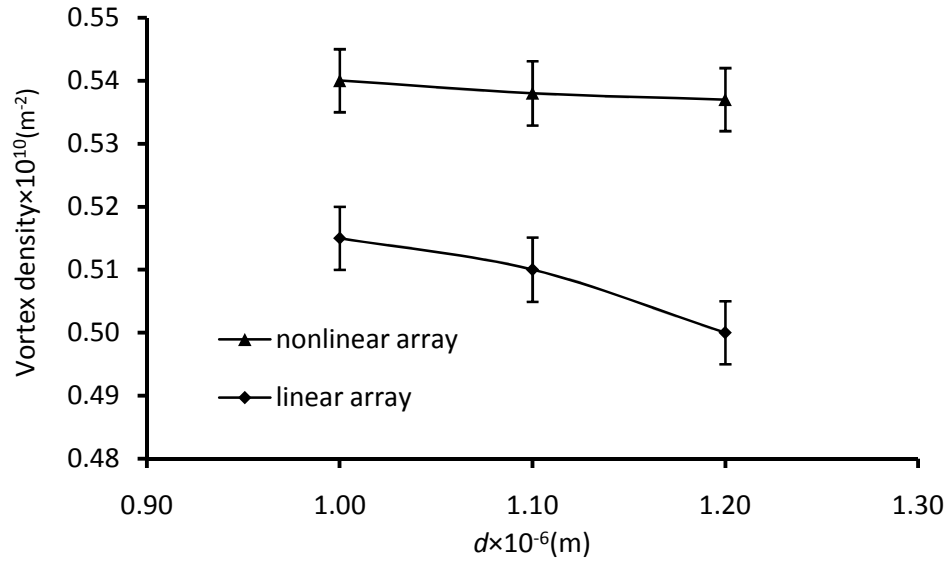
Figure 54 Statistical vortex density vs. distance for n_{core}=1.5, $n_{cladding}$=1.446, Z=10 and

R=0.29±10%.

Figure 53 shows the statistical analysis results for the mean vortex density versus core radius when the distance between the cores randomly changes by ±10%. Linear vortex density $v_{d,l}$ and nonlinear vortex density $v_{d,nl}$ in number per meters squared (m^{-2}) are plotted versus core radius r in meters (m) for 127 cores.

Linear regression analysis shows a positive slope, i.e. mean vortex density increasing with core radius. That is expressed as ($[v_{d,l}]_r$=0.158×10^{16}r+0.218×10^{10}) and ($[v_{d,nl}]_r$=0.144×10^{16}r+0.311×10^{10}) where $[v_{d,l}]_r$ and $[v_{d,nl}]_r$ are in m^{-2} and r is in meters. As new vortices are formed at the core boundaries, Equations for $[v_{d,l}]_r$ and $[v_{d,nl}]_r$ can be expressed as functions of the core perimeter as ($[v_{d,l}]_r$=0.025×10^{16}[2πr]+0.218×10^{10}) and ($[v_{d,nl}]_r$=0.023×10^{16}[2πr]+0.311×10^{10}) so that the dependence of the number of vortices on the boundaries is represented explicitly. Since cores should not touch each other, the former two Equations are only possible when 0<r<d/2.

Similarly, Figure 54 shows the statistical analysis results for the mean vortex density versus distance among cores when the core radius randomly changes by ±10%. In addition, linear vortex density $v_{d,l}$ and nonlinear vortex density $v_{d,nl}$ in number per meters squared (m^{-2}) are plotted versus distance among cores d in meters (m) for 127 cores.

The regression analysis shows a negative slope, i.e. mean vortex density decreasing with distance among cores. That is expressed as ($[v_{d,l}]_d$=-0.015×10^{16}d+0.554×10^{10}) and ($[v_{d,nl}]_d$=-0.075×10^{16}d+0.59×10^{10}) where $[v_{d,l}]_d$ and $[v_{d,nl}]_d$ are in m^{-2} and d is in meters.
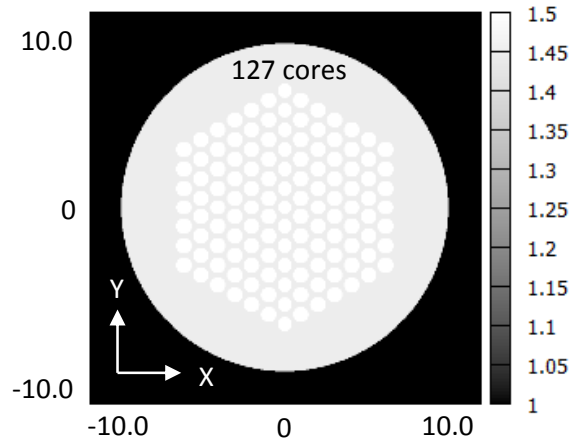
Figure 55 n(X,Y) for 127 cores with cladding in air for n_{core}=1.5, $n_{cladding}$=1.446, R=0.4 and D=0.2.

For comparison, the data in Figures 24 and 29 are re-evaluated for 127 cores with the same parameters as w_0=5.0μm, wavelength of λ=1.5μm, normalized radius of R=0.4 and normalized distance of D=0.2. The simulation results are re-calculated according to the arrangement re-shown in Figure 55 when the 127 cores with n_{core}=1.5 and cladding with $n_{cladding}$=1.446 are surrounded by are air with n_0=1.0.

Figure 56 shows the vortex density calculated from Figures 24 and 29 above. The curves pattern is different but still show an increasing tendency with respect to the

propagation distance. The vortex densities are higher for R=0.4 compared to those of R=0.29 which is in good agreements with the results in Figure 53.
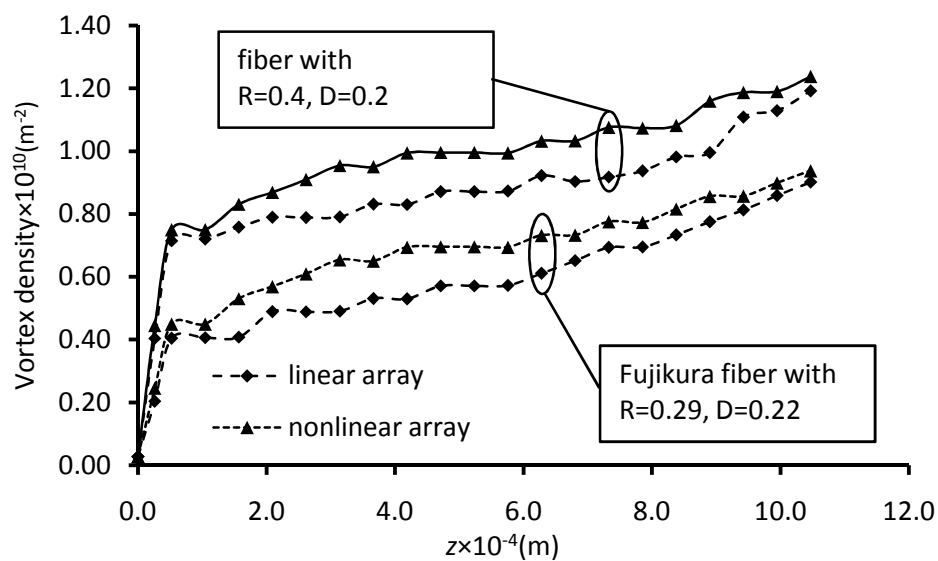
Figure 56 Comparison of results with respect to propagation distance.

Chapter 6   Implementation and Application

The optical vortex is characterized by a helical wavefront and a circular dark spot with a point of zero intensity due to phase singularity. These features construct a robust optical structure that demonstrates particle like characteristics. The harmonic azimuthal phase ramp is not affected by light diffraction and forms an inherent property in any optical vortex. The point of zero intensity and the phase singularity are therefore employed to find the location of any optical vortex. Here, we discuss the potential implementation for experiments that can the count number of vortices based on our presentations in Chapters 4 and 5. Finally, we consider possible applications of vortex counting in a fiber array.

6.1 Implementation

Work completed by simulation in Chapters 4 and 5 can be investigated experimentally to find out more about optical vortex dynamics. Figure 57 shows a possible experimental setup using a Gaussian laser beam emitted by a He-Ne source with a wavelength $\lambda=$ 632.8 nm. The optical vortex can be created using a computer generated hologram (CGH) placed at a desired distance from the source. The entire optical field can then be adjusted to a suitable beam width using defocusing lens L1 and focusing lens L2 at distance d before being split by a beam splitter BS1. The initial beam is divided into two portions travelling in different paths. In Figure 57, the portion with field of E_0 propagates along the reference path while another portion moves along the object path and is coupled to the waveguide.

The fiber being tested could be the array bundle fiber such as the Fujikura image fiber discussed in Chapter 5. Both fields can then be combined again using BS2 at an angle θ to facilitate interference and display dislocation points. Lens L3 can be used for focusing the final field to a charged coupled device (CCD) camera for imaging of the intensity profile and the interferogram.
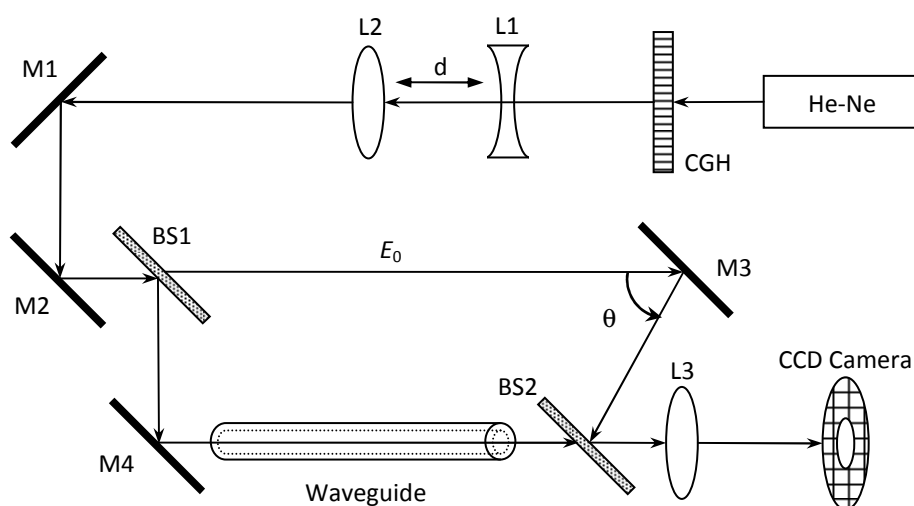
Figure 57 Possible experimental setup.

As shown in Figure 57, mirrors M1, M2, M3 and M4 are used to guide the path of the fields in the laboratory.

6.2 Application

Based on the previous statistical analysis discussed in Chapter 5, the mean vortex density varies with respect to the propagation distance and the core radius. The changes of the vortex density with respect to the core radius can be employed for sensing purposes. The radius of cores may differ in response to temperature changes or tension which will vary

the vortex density accordingly.

The Shack-Hartmann wavefront sensor can be used to detect the number of vortices and then the vortex density [38-40]. Since it is integrated with a CCD camera, it replaces the CCD camera in the setup shown in Figure 57. The technique is fundamentally based on measuring the phase slopes of the incident wavefront. As shown in Figure 58, this type of wavefront sensor uses a lenslet array to sample the wavefront of the optical field. The focal points of the lenslet array may locate on, before or after the back focal plane of the lenslet array due to the shape of the incident wavefront. The focal points may also have lateral or longitudinal shifts on the focal plane due to the slope of the wavefront. The slope for each of these samples is defined by the location of the focal point formed by each lens of the array in its back focal plane. To simplify the analysis, the lenslet array is assumed to be a square array of lenslets each with a squared sub-aperture. The CCD camera is placed in the back focal plane of the lenslet array. A small sub-array of this detector array of the camera is dedicated to each lenslet of the lenslet array. This subarray is used to determine the location of the focal point produced by each lenslet [38-40].
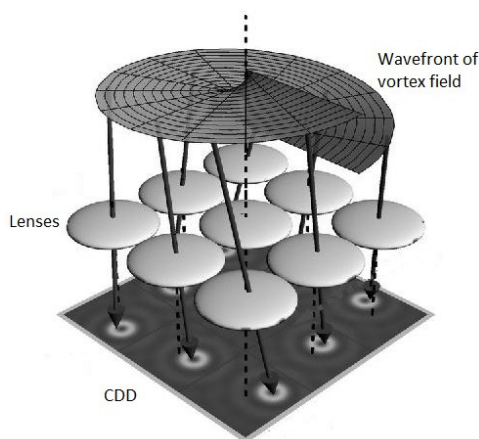
Figure 58 Vortex detection by a Shack-Hartmann wavefront sensor [48].

The average phase slope for each sub-aperture is given by the location of the focal point between the phase tilt of the incident wave in front of a lens and the location of the resulting focal point behind it. The overall structure of the Shack-Hartmann wavefront sensor is shown in Figure 58 for a vortex incident field [38-40].
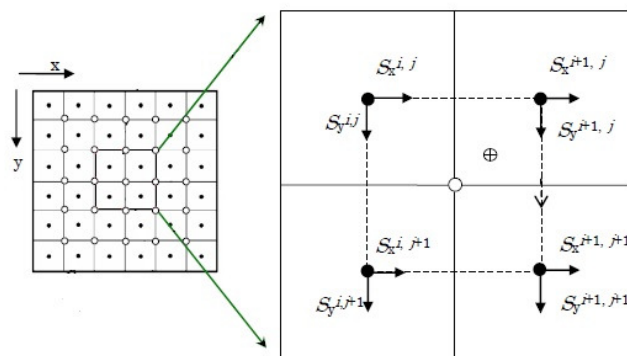
Figure 59 Circulation of phase slopes [40].

The pixels that specify the existence of a phase singularity can be determined by the circulation process illustrated in Figure 59 with S as the phase slope [40]. These pixels can be easily counted in order to calculate the vortex density from the image captured by the CCD camera in the setup of Figure 57. As shown in Figure 59, the samples used in the circulation process are denoted by the points in the centers of the sub-apertures. The circulation represents a line integral performed over the four sub-apertures along a contour denoted by the dashed lines. The result of this circulation process is a distribution of the topological charges of the optical vortices. It is positive (negative) at the locations of optical vortices with positive (negative) topological charges and it should be zero where there are no vortices [38-40].

The complete setup previously shown in Figure 57 with the Shack-Hartmann

wavefront sensor of Figure 58 can be used as a temperature or tension sensor. The sensitivity for change in vortex density with respect to core radius r is the slope of the regression line in Section 5.4. As the slope soars, the sensitivity increases accordingly indicating that higher vortex density is found when the core radius is increased.
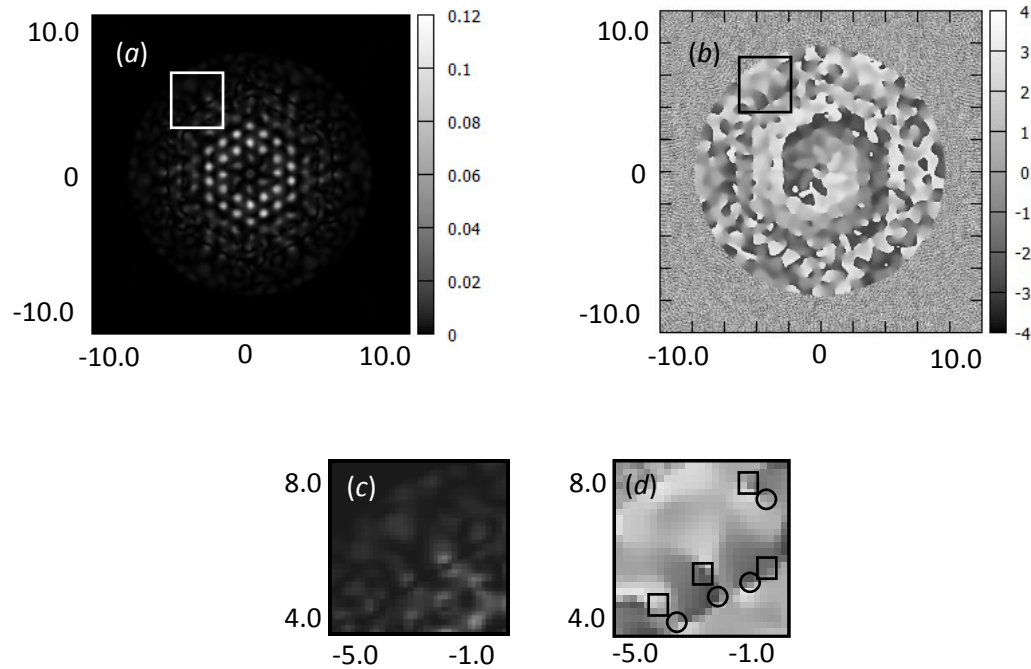
Figure 60 Intensity (a) and phase (b) in 127 cores at Z=10 for n_{core}=1.5, $n_{cladding}$=1.446, R=0.29 and D=0.22, sample of the intensity (c), sample of the phase with □=-1 charge and ○=+1 charge (d).

For the fiber array arrangement shown in Figure 55, the intensity and phase of the vortex beam are shown in Figure 60(a) and Figure 60(b) respectively. These images are generated for λ=1.5µm, w_0=5µm, R=0.29 and D=0.22 for Δ=0.02 and Z=10. The vortex beam then propagates to a beam magnifier and collimator and then to a lenslet array. A good commercially available Shack-Hartmann wavefront sensor (SHWS) can be found from THORLABS with a 1.3 Megapixel resolution CCD and a pixel size of

4.65μm×4.65μm [86]. The microlens array in this sensor has an effective focal length of 3.7mm and 39×31 lenses and a size of 1.0cm×1.0cm [86]. The setup for the SHWS is shown in Figure 61. The optical field out of the fiber array propagates in free space and then is optically magnified and collimated onto the SHWS.
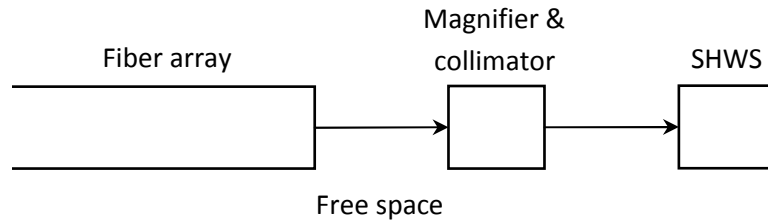
Figure 61 Setup for the SHWS.

Figure 60(b) shows the output phase for a 127 cores fiber array at Z=10 with several points of phase singularity. From Table 11, the average saturation vortex density is almost $25.5\times10^{10}\text{m}^{-2}$ with a vortex size of $9.0\times10^{-12}\text{m}^2$ for beam width w_0=5μm. As shown in Figure 58, we need at least 9 lenses to detect an optical vortex with a lenslet and thus we need $9\times25.5\times10^{10}\times14^2\times w_0^2$~11245 lenses. The required number of lenses is much larger than that of the THORLABS SHWS 39×31=1209 and thus the phase image in Figure 60(b) cannot be processed entirely. Hence, we used the beam magnifier and collimator to zoom into a smaller sample region of $4w_0\times4w_0=4\times10^{-10}\text{m}^2$ as shown in Figure 60(c) and Figure 60(d) for our analysis. In this smaller area we need $9\times25.5\times10^{10}\times16\times w_0^2$~918 lenses and thus it is possible to accurately detect phase singularities and find circulation fields. Moreover, the smaller area is selected in that part of the image shown in Figure 60(a) and Figure 60(b) in order to avoid high intensities that may saturate the CCD camera in the SHWS and prevent the setup from detecting the

number of vortices. Based on the size of the lenslet and the size of the selected area, the magnifier should enlarge the sample region by a factor of 4×5.0μm/0.01m=500.
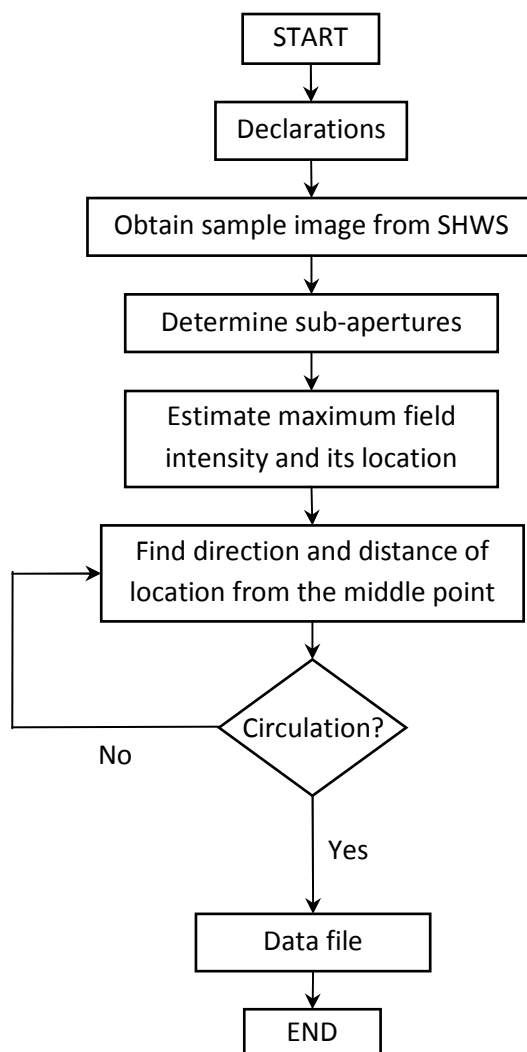
Figure 62 Circulation field flow chart.

As discussed earlier, the SHWS is a convertor that generates intensity images of light in terms of the inputted field phase. The SHWS considered here is assumed to generate an intensity image similar to that of the phase image shown in Figure 60(*d*). The image out of the SHWS as from Figure 61 can be processed using the simulation

algorithm shown in the flow chart of Figure 62 for the circulation field computation. In each sub-aperture of the wavefront sensor of Figure 59, the maximum point of the field intensity is calculated and its location is determined. The distance is then calculated between the location of the maximum point of the field intensity and the middle point of the sub-aperture. Also, the direction of that distance is found proportional to the middle point of the sub-aperture. If the calculated distances and their directions form a circulation process, these pixels specify the existence of a phase singularity with +1 for clockwise circulation and -1 for counter clockwise circulation. Otherwise, there are no circulations if the phase singularity is zero which means that there are no vortices.

The numerically simulated circulation field in Figure 63 has the same number of vortices and vortex locations as those of Figure 60(*d*). Vortex pairs are shown as white and black pixels with a polarity of +1 and -1 respectively.
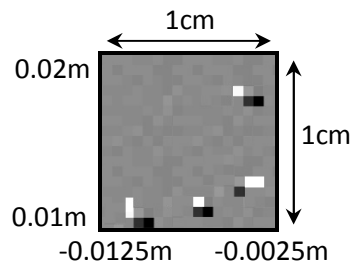
Figure 63 Circulation field for a magnified version of Figure 60(*d*)

with □=-1 charge and ■=+1 charge.

Assuming that the fiber array is composed of pure silica, the thermal expansion coefficient is about $\alpha=4.1\times10^{-7}$m/^{o}C at 20°C [87]. We also assume the fiber array to be $r=1.45\mu$m and $d=1.1\mu$m at 20°C. When this fiber array is used as a temperature sensor,

the change in temperature ΔT affect the fiber array cross section area and induces change in the core radius as $\Delta r = \alpha \Delta T$ as well as a change in the distance as $\Delta d = \alpha \Delta T$. For $\Delta T = 1^\circ C$, $\Delta r = 4.1 \times 10^{-7}$m and $\Delta d = 4.1 \times 10^{-7}$m.

Let's assume that the linear vortex density is v_d and that it changes as a function of radius core r and distance between the cores d as $v_d(r,d)$. Using total derivatives [88], the change in the number of vortices can be expressed as:

$$\Delta v_d(r,d) = \frac{\partial v_d}{\partial r} \Delta r + \frac{\partial v_d}{\partial d} \Delta d \tag{6.1}$$

where $\partial v_d/\partial r$ and $\partial v_d/\partial d$ are the slopes in Figures 53 and 54 found by regression analysis as $0.158 \frac{1 \times 10^{16}}{m^2 - m}$ and $-0.015 \frac{1 \times 10^{16}}{m^2 - m}$ approximately. Then, the change of vortex density in the ranges proposed in Figures 53 and 54 for only $1^\circ C$ change in temperature is almost 0.06×10^{10}m^{-2} with changes in core radius having stronger effects. From Figures 53 and 54, with nominal values of $r = 1.45 \times 10^{-6}$m and $d = 1.1 \times 10^{-6}$m, the tolerance in vortex density is $\pm 0.029 \times 10^{10}$m^{-2} with a vortex density of 0.46×10^{10}m^{-2} and a percentage change of ~13.04%±6.3%. This estimate illustrates that the setup can detect $1^\circ C$ temperature change although there is a random variation of ±10% in core radius.

Therefore, possible changes in the surrounding temperature may thermally expand the fiber array. As a result, the core radius r and the distance between the cores d increase. Since the increase in vortex density induced by the increase of r is more than the decrease in vortex density induced by the increase of d, the net effect is an increase in the vortex density detected by the SHWS. In this way, an optical vortex initially propagating in a fiber array can be used as a sensor.

Chapter 7   Recommendations and Conclusions

In this research, we employed BPM to investigate the propagation of an optical vortex in a fiber array. The Crank-Nicholson technique was used along with the BPM for the stability of numerical computations. The differential operators in the paraxial wave Equation were then discretized by the finite difference technique. In order to eliminate reflections of the propagating fields by the computational boundaries, the TBC technique was employed assuming a plane wave incident field with a constant of propagation calculated from a previous numerical step.

In addition, optical vortices generated numerically using FORTRAN codes showed excellent agreement with those expressed analytically by Equations based on coupled mode theory. Our simulation program is tested for different types of optical fibers as well as fiber arrays. An optical fiber with an array of multiple cores in hexagonal arrangement was particularly tested for the propagation of an optical vortex using BPM. Numerical results for arrays of two cores are compared to the semi-analytical solutions using mode coupled theory.

Calculations demonstrated satisfactory results which encouraged additional investigations for different core arrangements. The difference in the index of refraction among the cores and cladding was assumed to be very small in order to minimize the spatial frequency for that quantity. In addition, the radius of cores was supposedly relatively small with a small V number in such a way that only single mode is allowed to propagate in each core of the fiber array.

The simulation was modified to work with matrices of different sizes. The results

were evaluated for a 250×250 matrix compared to other results from 500×500 and 1000×1000 matrices. Higher matrix sizes generate better image resolution but may require more running time. Final image quality was almost acceptable but a matrix size of 1000×1000 was selected for magnifying purposes.

Following our basic definition of the optical vortex as a point of zero intensity with a phase change from $-\pi$ to π around it, new vortices are traced by both points of dislocation and phase variations. Once the zero intensity point is located, the phase around that point and its polarity is tested for a relative change between $-\pi$ and π or vice versa. In addition, dislocation points are detected by the interference of the propagating field and a plane wave reference by an angle of $\pi/4$ with respect to the x-axis.

Statistical analysis was completed to estimate the vortex density versus propagation distance, core radius and distance between the cores in the fiber array. The simulation was run 100 times with a random increase and decrease of 10% of the core radius. The averages were then calculated with the standard deviations as error bars.

The Shack-Hartmann wavefront sensor was investigated to detect phase singularities in the optical field. The generated circulation field used in this simulation was employed to create images that determine the number of vortices and their locations.

7.1   Conclusions

The finite difference beam propagation method (FD-BPM) is a robust approach to numerically deal with optical field propagations in waveguides. This numerical method was implemented successfully with the transparent boundary condition to reduce reflections from the computational boundaries. We showed the validity of this method for

the modeling of optical vortex propagation in optical fibers. In a triangular lattice fiber core array, it is possible to find the number of the zero intensity points and phase change in response to surrounding variations.

In a linear and nonlinear triangular lattice core arrangement, the generation of new vortices is very dynamic with respect to the longitudinal distance and the number of cores in the fiber array. As the number of cores increases and the beam propagates at longer distances, additional optical vortices are created. Nevertheless, new vortices could not exist constantly and may possibly fade away while other new vortices are produced at different locations.

In a linear triangular lattice of fiber array, the generation of new vortices is sensitive to the cores radius and the distance between these cores. The number of new vortices increases with the number of cores in the array lattice.

In a nonlinear triangular lattice, the generation of new vortices is also found to be sensitive to the core radius or the distance between them. However, the number of new vortices tends to increase as the core radius increases and decrease as the distance between cores increases for a positive as well as negative nonlinear coefficient.

New vortices are generated under the effects of the phase rotation around points of zero intensity. The intensity of the optical field on the transverse plane is strongly dependent on mode coupling between the array cores and shows great variations as the field propagates. On that basis, the generation pattern of the new vortices is unstable as they are continually formed with different numbers and locations along the array structure.

The original vortex field is found to continue in its central location as it propagates

in the lattice. However, an off-centered field to another core may exhibit some changes in its original location as it propagates due to coupling and reflections between the cores.

Simulations are presented mostly based on the vortex density rather than the number of vortices. This is the number of vortices per unit area which allows better calculation flexibility compared to the number of vortices. It is found that the vortex density increases with respect to the core radius and decreases as the distance between cores increases. As a consequence, this can be employed as a temperature or tension sensor with the use of the Shack-Hartmann wavefront sensor.

In our statistical analysis, the vortex density is found to increase with propagation distance until saturation where the entire area of the fiber array is full of vortices. However, farther propagation of the optical field shows a decrease in the vortex density below the saturation level due to the annihilation process of the vortex pairs. Statistical analysis also shows an increase in the vortex density with respect to the core radius which further confirms that new vortices are generated at the core boundaries. Statistical results reveal that the vortex density decreases when cores are farther away from each other in the fiber array.

The overall fiber array with cores in hexagonal arrangement can be used as a temperature sensor with an optical vortex as an initial field. The circulation field images generated by the Shack-Hartmann wavefront sensor greatly facilitate the use of the vortex density variations to gauge changes in temperature.

7.2   Future work

For comparison purposes, this research can be completed by employing different

analytical or numerical procedures such as Fourier analysis or Runge-Kutta methods. The final outcome can be assessed and judged against the methods employed in our work to find any discrepancies. Another research direction based on our works could be the use of the random, the periodic or the hexagonal fiber in data communications or in optical sensing. The intention is to develop a technique to modulate one or more parameters of the propagating optical vortex for carrying data with the highest possible signal to noise ratio.

Comparable to the work completed in this research, a number of other fiber array parameters can be modified such as the index of refraction. A beneficial future study could be the employment of a higher order optical vortex in a similar triangular lattice array to the one investigated in our research.

Potential applications in sensing could be further investigated with different types of wavefront sensors. Better accuracy and higher sensitivity are potential areas for future research of the Shack-Hartmann wavefront sensor. A sensor with a wider range could also be a topic of study.

Appendix A: Linear BPM Code

```
c     ===================
c     Muhammad A Mushref
c     PhD research in BPM
c     ===================
c
c     M=Matrix size (number of points in X),L=Number of steps in Z
c     N=numbers of holes
      parameter(M=1000,L=1100,NN=127)
      integer ifield,intfield,res
      real*8 dXY,dZ,X,Y,Z,w0,la,nh,th1,th2,th3,th4,
     +      ma(1:M,1:M),ph(1:M,1:M),pi,d,centx,centy,
     +      hx(1:NN),hy(1:NN),v1(1:NN),v2(1:NN),hr,n(1:M,1:M),
     +      nnn(1:M,1:M),r(1:M,1:M),energy(1:L)
      complex*16 mmm,AA,BB,CC,alph,gsn,vor,phiA(1:M,1:M),
     +         phiN(1:M,1:M),phiNS(1:M,1:M),phiI(1:M,1:M),
     +         BCS(1:M,1:M),BC(1:M,1:M),A(1:M,1:M),
     +         b(1:M),c(1:M),cp(1:M),dp(1:M)
      gsn(X,Y,Z,centx,centy)=(zexp(-((X-centx)**2+(Y-centy)**2)
     +              /(1.d0-(0.d0,1.d0)*Z)))
     +              /(1.d0-(0.d0,1.d0)*Z)
      vor(X,Y,Z,w0,la,centx,centy)=(dsqrt((X-centx)**2+(Y-centy)**2)/
     +              (1.d0+Z**2))*dexp(-((X-centx)**2+
     +              (Y-centy)**2)/(1.d0+Z**2))*zexp
     +              (-(0.d0,1.d0)*((2.d0*Z*(pi*w0/la)
     +              **2)+(((X-centx)**2+(Y-centy)**2)/
     +              (Z+1.d0/Z))+datan2(Y-centy,X-centx)
     +              -2.d0*datan(Z)))
      pi=3.14159265358979323846264338327 95
c
c
      print*,'Number of points in X and Y',M
      print*,'Number of steps in Z',L
      print*,'Number of holes inside core',NN
      print*,'Enter dXY'
      read*,dXY
      print*,'Enter dZ'
      read*,dZ
      print*,'Where is the center of the beam in X'
      read*,centx
      print*,'Where is the center of the beam in Y'
      read*,centy
```

```fortran
      print*,'Enter raduis of core'
      read*,hr
      print*,'Enter distance between cores'
      read*,d
      print*,'Enter refractive index of cores'
      read*,nh
      print*,'Enter beam width w0'
      read*,w0
      print*,'Enter wavelength'
      read*,la
      print*,'Enter incident angle from Z- to X-axis'
      read*,th1
      print*,'Enter incident angle from Z- to Y-axis'
      read*,th2
      print*,'Enter interference angle from Z- to X-axis'
      read*,th3
      print*,'Enter interference angle from Z- to Y-axis'
      read*,th4
      print*,'Enter integer resolution factor'
      print*,'1 means write every single step to data files'
      print*,'2 means write every second step to data files'
      print*,'3 means write every third  step to data files'
      print*,'and so on.....'
      read*,res
      open(unit=12,file='locations.dat',status='old')
      do 10 i=1,NN
        read(12,*),v1(i),v2(i)
        hx(i)=((v1(i)+v2(i))*(2.d0*hr+d)*sqrt(3.d0)/2.d0)+dXY*M/2.d0
        hy(i)=((-v1(i)+v2(i))*(2.d0*hr+d)/2.d0)+dXY*M/2.d0
10    continue
c
      alph=(0.d0,1.d0)*dZ/(4.d0*dXY*dXY)
      AA=1.d0-alph
      BB=1.d0+alph
      CC=alph/2.d0
c
      do 30 i=1,M
        do 20 j=1,M
          n(i,j)=1.d0
20      continue
30    continue
c
      do 80 ii=1,NN
       do 50 i=1,M
```

```fortran
      do 40 j=1,M
       r(i,j)=dsqrt((i*dXY-hx(ii))**2+(j*dXY-hy(ii))**2)
       nnn(i,j)=nh+int(min(r(i,j),1.9d0*hr)/hr)*(n(i,j)-nh)
40     continue
50    continue
      do 70 i=1,M
       do 60 j=1,M
         n(i,j)=nnn(i,j)
60     continue
70    continue
80   continue
c
     do 100 i=1,M
      do 90 j=1,M
        A(i,j)=zexp(-(0.d0,1.d0)*dZ*((n(i,j)**2)-1.d0)
     +          *(pi*w0/la)**2)
90     continue
100   continue
c
110    print*,'what is the initial field?'
      print*,'1 vortex   2 Gaussian'
      read*,ifield
      if(ifield.eq.1) then
       do 130 i=1,M
        do 120 j=1,M
         phiA(i,j)=vor(i*dXY,j*dXY,0.d0,w0,la,
     +           centx+dXY/2.d0,centy+dXY/2.d0)*
     +           zexp((0.d0,1.d0)*(2.d0*pi*w0/la)*(
     +           dsin(th1)*(i*dXY-centx+dXY/2.d0)+
     +           dsin(th2)*(j*dXY-centy+dXY/2.d0)))
         phiN(i,j)=phiA(i,j)
120     continue
130    continue
      elseif(ifield.eq.2) then
       do 150 i=1,M
        do 140 j=1,M
         phiA(i,j)=gsn(i*dXY,j*dXY,0.d0,centx,centy)*
     +           zexp((0.d0,1.d0)*(2.d0*pi*w0/la)*(
     +           dsin(th1)*(i*dXY-centx)+
     +           dsin(th2)*(j*dXY-centy)))
         phiN(i,j)=phiA(i,j)
140     continue
150    continue
      else
```

```fortran
       goto 110
       endif
160    print*,'what is the interference field?'
       print*,'1 plane   2 Gaussian'
       read*,intfield
       if(intfield.eq.1) then
        do 180 i=1,M
          do 170 j=1,M
            phiI(i,j)=zexp(-(0.d0,1.d0)*1800.d0*(
     +            dsin(th3)*(i*dXY-centx)+
     +            dsin(th4)*(j*dXY-centy)))
170       continue
180     continue
       elseif(intfield.eq.2) then
        do 200 i=1,M
          do 190 j=1,M
            phiI(i,j)=gsn(i*dXY,j*dXY,0.d0,centx,centy)*
     +            zexp(-(0.d0,1.d0)*30.d0*(
     +            dsin(th3)*(i*dXY-centx)+
     +            dsin(th4)*(j*dXY-centy)))
190       continue
200     continue
       else
        goto 160
       endif
c
       do 310 ie=1,L
          do 210 i=1,M
            BCS(i,1)=BB*phiN(i,1)-CC*phiN(i,2)
210       continue
          do 220 i=1,M
            BCS(i,M)=BB*phiN(i,M)-CC*phiN(i,M-1)
220       continue
          do 240 i=1,M
            do 230 j=2,M-1
              BCS(i,j)=BB*phiN(i,j)-CC*(phiN(i,j+1)+
     +              phiN(i,j-1))
230         continue
240       continue
          call td1(AA,CC,M,BCS,phiNS)
c
c
          do 250 j=1,M
            BC(1,j)=(BB*phiNS(1,j)-CC*phiNS(2,j))*A(1,j)
```

```
250      continue
     do 260 j=1,M
       BC(M,j)=(BB*phiNS(M,j)-CC*phiNS(M-1,j))*A(M,j)
260      continue
     do 280 i=2,M-1
       do 270 j=1,M
         BC(i,j)=(BB*phiNS(i,j)-CC*(phiNS(i+1,j)+
   +            phiNS(i-1,j)))*A(i,j)
270      continue
280      continue
     call td2(AA,CC,M,BC,phiN)
     energy(ie)=0.d0
     do 300 i=1,M
       do 290 j=1,M
         energy(ie)=energy(ie)+abs(phiN(i,j))**2
290      continue
300      continue
310    continue
c
   open(unit=1,file='initial_field_intensity.dat',status='new')
   open(unit=2,file='initial_field_phase.dat',status='new')
   open(unit=3,file='analytical_field_intensity_after_propagation_
   +    in_freespace.dat',status='new')
   open(unit=4,file='analytical_field_phase_after_propagationd_in_
   +    freespace.dat',status='new')
   open(unit=5,file='numerical_field_intensity_after_propagation_
   +    in_meduim.dat',status='new')
   open(unit=6,file='numerical_field_phase_after_propagation_in_
   +    meduim.dat',status='new')
   open(unit=7,file='numerical_field_after_propagation_in_meduim_
   +    real_part.dat',status='new')
   open(unit=8,file='numerical_field_after_propagation_in_meduim_
   +    imaginary_part.dat',status='new')
   open(unit=9,file='n(X,Y).dat',status='new')
   open(unit=10,file='interference_intensity.dat',status='new')
   open(unit=11,file='interference_phase.dat',status='new')
   open(unit=12,file='energy.dat',status='new')
1    format(f20.16,1x,f20.16,1x,f30.27)
   if(ifield.eq.1) then
     do 330 i=1,M,res
       do 320 j=1,M,res
         write(3,1) i*dXY,j*dXY,abs(vor(i*dXY,j*dXY,L*dZ,w0,la,
   +                 centx+dXY/2.d0,centy+dXY/2.d0))**2
         write(4,1) i*dXY,j*dXY,datan2(dimag(vor(i*dXY,j*dXY,
```

```fortran
     +                       L*dZ,w0,la,centx+dXY/2.d0,
     +                       centy+dXY/2.d0)),dreal(vor(i*dXY,
     +                       j*dXY,L*dZ,w0,la,centx+dXY/2.d0,
     +                       centy+dXY/2.d0)))
320      continue
      write(3,1)
      write(4,1)
330      continue
       else
       do 350 i=1,M,res
         do 340 j=1,M,res
           write(3,1) i*dXY,j*dXY,abs(gsn(i*dXY,j*dXY,L*dZ,
     +                   centx,centy))**2
           write(4,1) i*dXY,j*dXY,datan2(dimag(gsn(i*dXY,j*dXY,
     +                   L*dZ,centx,centy)),dreal(gsn
     +                   (i*dXY,j*dXY,L*dZ,centx,centy)))
340      continue
      write(3,1)
      write(4,1)
350      continue
       endif
       do 370 i=1,M,res
        do 360 j=1,M,res
          write(1,1) i*dXY,j*dXY,abs(phiA(i,j))**2
          write(2,1) i*dXY,j*dXY,datan2(dimag(phiA(i,j)),
     +                   dreal(phiA(i,j)))
          write(5,1) i*dXY,j*dXY,abs(phiN(i,j))**2
          write(6,1) i*dXY,j*dXY,datan2(dimag(phiN(i,j)),
     +                   dreal(phiN(i,j)))
          write(7,1) i*dXY,j*dXY,dreal(phiN(i,j))
          write(8,1) i*dXY,j*dXY,dimag(phiN(i,j))
          write(9,1) i*dXY,j*dXY,n(i,j)
          write(10,1) i*dXY,j*dXY,abs(phiI(i,j)+phiN(i,j))**2
          write(11,1) i*dXY,j*dXY,datan2(dimag(phiI(i,j)+
     +                   phiN(i,j)),dreal(phiI(i,j)+
     +                   phiN(i,j)))
360      continue
      write(1,1)
      write(2,1)
      write(5,1)
      write(6,1)
      write(7,1)
      write(8,1)
      write(9,1)
```

```fortran
      write(10,1)
      write(11,1)
370   continue
      do 380 i=1,L
       write(12,*) i*dZ,energy(i)/M
380   continue
      end
c
c
c
c
c
      subroutine td1(AA,CC,M,BC,phi)
      complex*16 mmm,AA,CC,phi(1:M,1:M),BC(1:M,1:M),
     +      b(1:M),c(1:M),cp(1:M),dp(1:M)
      do 10 i=1,M
       b(i)=AA
10    continue
      do 20 i=1,M-1
       c(i)=CC
20    continue
      c(M)=0.d0
      cp(1)=c(1)/b(1)
      do 50 jj=1,M
       dp(1)=BC(1,jj)/b(1)
       do 30 i=2,M
         mmm=b(i)-cp(i-1)*CC
         cp(i)=c(i)/mmm
         dp(i)=(BC(i,jj)-dp(i-1)*CC)/mmm
30      continue
       phi(M,jj)=dp(M)
       do 40 i=M-1,1,-1
         phi(i,jj)=dp(i)-cp(i)*phi(i+1,jj)
40      continue
50    continue
      return
      end
c
c
      subroutine td2(AA,CC,M,BC,phi)
      complex*16 mmm,AA,CC,phi(1:M,1:M),BC(1:M,1:M),
     +      b(1:M),c(1:M),cp(1:M),dp(1:M)
      do 10 i=1,M
       b(i)=AA
```

```
10      continue
        do 20 i=1,M-1
         c(i)=CC
20      continue
        c(M)=0.d0
        cp(1)=c(1)/b(1)
        do 50 ij=1,M
          dp(1)=BC(ij,1)/b(1)
          do 30 i=2,M
            mmm=b(i)-cp(i-1)*CC
            cp(i)=c(i)/mmm
            dp(i)=(BC(ij,i)-dp(i-1)*CC)/mmm
30        continue
          phi(ij,M)=dp(M)
          do 40 i=M-1,1,-1
            phi(ij,i)=dp(i)-cp(i)*phi(ij,i+1)
40        continue
50      continue
        return
        end
```

Appendix B: Nonlinear BPM Code

```
c    ===================
c    Muhammad A Mushref
c    PhD research in BPM
c    ===================
c
c    M=Matrix size (number of points in X),L=Number of steps in Z
c    N=numbers of holes
     parameter(M=1000,L=800,NN=127)
     integer ifield,intfield,res
     real*8 dXY,dZ,X,Y,Z,w0,la,nh,n2,th1,th2,th3,th4,
    +      ma(1:M,1:M),ph(1:M,1:M),pi,d,centx,centy,
    +      hx(1:NN),hy(1:NN),v1(1:NN),v2(1:NN),hr,n(1:M,1:M),
    +      nnn(1:M,1:M),r(1:M,1:M),energy(1:L)
     complex*16 mmm,AA,BB,CC,alph,gsn,vor,phiA(1:M,1:M),
    +      phiN(1:M,1:M),phiNS(1:M,1:M),phiI(1:M,1:M),
    +      BCS(1:M,1:M),BC(1:M,1:M),A(1:M,1:M),AAA(1:M,1:M),
    +      b(1:M),c(1:M),cp(1:M),dp(1:M)
     gsn(X,Y,Z,centx,centy)=(zexp(-((X-centx)**2+(Y-centy)**2)
    +             /(1.d0-(0.d0,1.d0)*Z)))
    +             /(1.d0-(0.d0,1.d0)*Z)
     vor(X,Y,Z,w0,la,centx,centy)=(dsqrt((X-centx)**2+(Y-centy)**2)/
    +             (1.d0+Z**2))*dexp(-((X-centx)**2+
    +             (Y-centy)**2)/(1.d0+Z**2))*zexp
    +             (-(0.d0,1.d0)*((2.d0*Z*(pi*w0/la)
    +             **2)+(((X-centx)**2+(Y-centy)**2)/
    +             (Z+1.d0/Z))+datan2(Y-centy,X-centx)
    +             -2.d0*datan(Z)))
     pi=3.14159265358979323846264338 32795
c
     print*,'Number of points in X and Y',M
     print*,'Number of steps in Z',L
     print*,'Number of holes inside core',NN
     print*,'Enter dXY'
     read*,dXY
     print*,'Enter dZ'
     read*,dZ
     print*,'Where is the center of the beam in X'
     read*,centx
     print*,'Where is the center of the beam in Y'
     read*,centy
     print*,'Enter raduis of core'
```

```fortran
      read*,hr
      print*,'Enter distance between cores'
      read*,d
      print*,'Enter refractive index of cores'
      read*,nh
      print*,'Enter Optical Kerr Coefficient'
      read*,n2
      print*,'Enter beam width w0'
      read*,w0
      print*,'Enter wavelength'
      read*,la
      print*,'Enter incident angle from Z- to X-axis'
      read*,th1
      print*,'Enter incident angle from Z- to Y-axis'
      read*,th2
      print*,'Enter interference angle from Z- to X-axis'
      read*,th3
      print*,'Enter interference angle from Z- to Y-axis'
      read*,th4
      print*,'Enter integer resolution factor'
      print*,'1 means write every single step to data files'
      print*,'2 means write every second step to data files'
      print*,'3 means write every third  step to data files'
      print*,'and so on.....'
      read*,res
      open(unit=12,file='locations.dat',status='old')
      do 10 i=1,NN
        read(12,*),v1(i),v2(i)
        hx(i)=((v1(i)+v2(i))*(2.d0*hr+d)*sqrt(3.d0)/2.d0)+dXY*M/2.d0
        hy(i)=((-v1(i)+v2(i))*(2.d0*hr+d)/2.d0)+dXY*M/2.d0
10    continue
c
      alph=(0.d0,1.d0)*dZ/(4.d0*dXY*dXY)
      AA=1.d0-alph
      BB=1.d0+alph
      CC=alph/2.d0
      do 30 i=1,M
        do 20 j=1,M
          n(i,j)=1.d0
20      continue
30    continue
c
      do 80 ii=1,NN
       do 50 i=1,M
```

```
      do 40 j=1,M
        r(i,j)=dsqrt((i*dXY-hx(ii))**2+(j*dXY-hy(ii))**2)
        nnn(i,j)=nh+int(min(r(i,j),1.9d0*hr)/hr)*(n(i,j)-nh)
40    continue
50    continue
      do 70 i=1,M
        do 60 j=1,M
          n(i,j)=nnn(i,j)
60      continue
70    continue
80    continue
c
      do 1000 i=1,M
        do 900 j=1,M
          AAA(i,j)=zexp(-(0.d0,1.d0)*dZ*((n(i,j)**2)-1.d0)
     +            *(pi*w0/la)**2)
900     continue
1000  continue
c
90    print*,'what is the initial field?'
      print*,'1 vortex   2 Gaussian'
      read*,ifield
      if(ifield.eq.1) then
       do 110 i=1,M
         do 100 j=1,M
           phiA(i,j)=vor(i*dXY,j*dXY,0.d0,w0,la,
     +            centx+dXY/2.d0,centy+dXY/2.d0)*
     +            zexp((0.d0,1.d0)*(2.d0*pi*w0/la)*(
     +            dsin(th1)*(i*dXY-centx+dXY/2.d0)+
     +            dsin(th2)*(j*dXY-centy+dXY/2.d0)))
           phiN(i,j)=phiA(i,j)
100      continue
110    continue
       elseif(ifield.eq.2) then
        do 130 i=1,M
          do 120 j=1,M
            phiA(i,j)=gsn(i*dXY,j*dXY,0.d0,centx,centy)*
     +            zexp((0.d0,1.d0)*(2.d0*pi*w0/la)*(
     +            dsin(th1)*(i*dXY-centx)+
     +            dsin(th2)*(j*dXY-centy)))
            phiN(i,j)=phiA(i,j)
120       continue
130     continue
      else
```

```
      goto 90
      endif
140   print*,'what is the interference field?'
      print*,'1 plane   2 Gaussian'
      read*,intfield
      if(intfield.eq.1) then
       do 160 i=1,M
         do 150 j=1,M
           phiI(i,j)=zexp((0.d0,1.d0)*30.d0*(
     +           dsin(th3)*(i*dXY-centx)+
     +           dsin(th4)*(j*dXY-centy)))
150      continue
160    continue
      elseif(intfield.eq.2) then
       do 180 i=1,M
         do 170 j=1,M
           phiI(i,j)=gsn(i*dXY,j*dXY,0.d0,centx,centy)*
     +           zexp((0.d0,1.d0)*30.d0*(
     +           dsin(th3)*(i*dXY-centx)+
     +           dsin(th4)*(j*dXY-centy)))
170      continue
180    continue
      else
       goto 140
      endif
c
      do 310 ie=1,L
         do 190 i=1,M
           BCS(i,1)=BB*phiN(i,1)-CC*phiN(i,2)
190      continue
         do 200 i=1,M
           BCS(i,M)=BB*phiN(i,M)-CC*phiN(i,M-1)
200      continue
         do 220 i=1,M
           do 210 j=2,M-1
             BCS(i,j)=BB*phiN(i,j)-CC*(phiN(i,j+1)+
     +             phiN(i,j-1))
210        continue
220      continue
         call td1(AA,CC,M,BCS,phiNS)
c
c
         do 240 i=1,M
           do 230 j=1,M
```

```
          A(i,j)=zexp(-(0.d0,1.d0)*dZ*
     +           (w0*n2*pi/(120.d0*la**2))*abs(phiN(i,j))**2)
230       continue
240     continue
c
c
      do 250 j=1,M
        BC(1,j)=(BB*phiNS(1,j)-CC*phiNS(2,j))*A(1,j)*AAA(1,j)
250     continue
      do 260 j=1,M
        BC(M,j)=(BB*phiNS(M,j)-CC*phiNS(M-1,j))*A(M,j)*AAA(M,j)
260     continue
      do 280 i=2,M-1
        do 270 j=1,M
          BC(i,j)=(BB*phiNS(i,j)-CC*(phiNS(i+1,j)+
     +           phiNS(i-1,j)))*A(i,j)*AAA(i,j)
270       continue
280     continue
      call td2(AA,CC,M,BC,phiN)
      do 300 i=1,M
        do 290 j=1,M
          energy(ie)=energy(ie)+abs(phiN(i,j))**2
290       continue
300     continue
310   continue
c
    open(unit=1,file='initial_field_intensity.dat',status='new')
    open(unit=2,file='initial_field_phase.dat',status='new')
    open(unit=3,file='analytical_field_intensity_after_propagation_
   +   in_freespace.dat',status='new')
    open(unit=4,file='analytical_field_phase_after_propagationd_in_
   +   freespace.dat',status='new')
    open(unit=5,file='numerical_field_intensity_after_propagation_
   +   in_meduim.dat',status='new')
    open(unit=6,file='numerical_field_phase_after_propagation_in_
   +   meduim.dat',status='new')
    open(unit=7,file='numerical_field_after_propagation_in_meduim_
   +   real_part.dat',status='new')
    open(unit=8,file='numerical_field_after_propagation_in_meduim_
   +   imaginary_part.dat',status='new')
    open(unit=9,file='n(X,Y).dat',status='new')
    open(unit=10,file='interference_intensity.dat',status='new')
    open(unit=11,file='interference_phase.dat',status='new')
    open(unit=12,file='energy.dat',status='new')
```

```fortran
1     format(f20.16,1x,f20.16,1x,f30.27)
      if(ifield.eq.1) then
        do 330 i=1,M,res
          do 320 j=1,M,res
            write(3,1) i*dXY,j*dXY,abs(vor(i*dXY,j*dXY,L*dZ,w0,la,
     +                 centx+dXY/2.d0,centy+dXY/2.d0))**2
            write(4,1) i*dXY,j*dXY,datan2(dimag(vor(i*dXY,j*dXY,
     +                 L*dZ,w0,la,centx+dXY/2.d0,
     +                 centy+dXY/2.d0)),dreal(vor(i*dXY,
     +                 j*dXY,L*dZ,w0,la,centx+dXY/2.d0,
     +                 centy+dXY/2.d0)))
320       continue
          write(3,1)
          write(4,1)
330     continue
      else
        do 350 i=1,M,res
          do 340 j=1,M,res
            write(3,1) i*dXY,j*dXY,abs(gsn(i*dXY,j*dXY,L*dZ,
     +                 centx,centy))**2
            write(4,1) i*dXY,j*dXY,datan2(dimag(gsn(i*dXY,j*dXY,
     +                 L*dZ,centx,centy)),dreal(gsn
     +                 (i*dXY,j*dXY,L*dZ,centx,centy)))
340       continue
          write(3,1)
          write(4,1)
350     continue
      endif
      do 370 i=1,M,res
        do 360 j=1,M,res
          write(1,1) i*dXY,j*dXY,abs(phiA(i,j))**2
          write(2,1) i*dXY,j*dXY,datan2(dimag(phiA(i,j)),
     +               dreal(phiA(i,j)))
          write(5,1) i*dXY,j*dXY,abs(phiN(i,j))**2
          write(6,1) i*dXY,j*dXY,datan2(dimag(phiN(i,j)),
     +               dreal(phiN(i,j)))
          write(7,1) i*dXY,j*dXY,dreal(phiN(i,j))
          write(8,1) i*dXY,j*dXY,dimag(phiN(i,j))
          write(9,1) i*dXY,j*dXY,n(i,j)
          write(10,1) i*dXY,j*dXY,abs(phiI(i,j)+phiN(i,j))**2
          write(11,1) i*dXY,j*dXY,datan2(dimag(phiI(i,j)+
     +                phiN(i,j)),dreal(phiI(i,j)+
     +                phiN(i,j)))
360     continue
```

```
        write(1,1)
        write(2,1)
        write(5,1)
        write(6,1)
        write(7,1)
        write(8,1)
        write(9,1)
        write(10,1)
        write(11,1)
370    continue
       do 380 i=1,L
        write(12,*) i*dZ,energy(i)
380    continue
       end
c
c
c
c
c
c
       subroutine td1(AA,CC,M,BC,phi)
       complex*16 mmm,AA,CC,phi(1:M,1:M),BC(1:M,1:M),
     +        b(1:M),c(1:M),cp(1:M),dp(1:M)
       do 10 i=1,M
        b(i)=AA
10     continue
       do 20 i=1,M-1
        c(i)=CC
20     continue
       c(M)=0.d0
       cp(1)=c(1)/b(1)
       do 50 jj=1,M
        dp(1)=BC(1,jj)/b(1)
        do 30 i=2,M
          mmm=b(i)-cp(i-1)*CC
          cp(i)=c(i)/mmm
          dp(i)=(BC(i,jj)-dp(i-1)*CC)/mmm
30      continue
        phi(M,jj)=dp(M)
        do 40 i=M-1,1,-1
          phi(i,jj)=dp(i)-cp(i)*phi(i+1,jj)
40      continue
50     continue
       return
```

```fortran
      end
c
c
      subroutine td2(AA,CC,M,BC,phi)
      complex*16 mmm,AA,CC,phi(1:M,1:M),BC(1:M,1:M),
     +          b(1:M),c(1:M),cp(1:M),dp(1:M)
      do 10 i=1,M
        b(i)=AA
10    continue
      do 20 i=1,M-1
        c(i)=CC
20    continue
      c(M)=0.d0
      cp(1)=c(1)/b(1)
      do 50 ij=1,M
        dp(1)=BC(ij,1)/b(1)
        do 30 i=2,M
          mmm=b(i)-cp(i-1)*CC
          cp(i)=c(i)/mmm
          dp(i)=(BC(ij,i)-dp(i-1)*CC)/mmm
30      continue
        phi(ij,M)=dp(M)
        do 40 i=M-1,1,-1
          phi(ij,i)=dp(i)-cp(i)*phi(ij,i+1)
40      continue
50    continue
      return
      end
```

References

[1] G. A. Swartzlander, Jr., and C. T. Law, "Optical vortex solitons observed in Kerr nonlinear media", *Physical Review Letters*, Vol. 69, 1992, pp. 2503-2506.

[2] C. T. Law and G. A. Swartzlander, Jr., "Optical vortex solitons and the stability of dark soliton stripes", *Optics Letters*, Vol. 18, No. 8, April 1993, pp. 586-588.

[3] Filippus Stefanus Roux, "Dynamical behavior of optical vortices", *Journal of the Optical Society of America B*, Vol. 12, No. 7, July 1995, pp. 1215-1221.

[4] Jason Christou, Vladimir Tikhonenko, Yuri S. Kivshar and Barry Luther-Davies, "Vortex soliton motion and steering", *Optics Letters*, Vol. 21, No. 20, October 1996, pp. 1649-1651.

[5] D. Rozas, C. T. Law and G. A. Swartzlander, Jr., "Propagation dynamics of optical vortices", *Journal of the Optical Society of America B*, Vol. 14, No. 11, November 1997, pp. 3054-3065.

[6] C. T. Law, X. Zhang and G. A. Swartzlander, Jr., "Waveguiding properties of optical vortex solitons", *Optics Letters*, Vol. 25, No. 1, January 2000, pp. 55-57.

[7] Andreas H. Carlsson, Johan N. Malmberg, Dan Anderson, Mietek Lisak, Eledna A. Ostrovskaya, Tristram J. Alexander and Yuri S. Kivshar, "Linear and nonlinear waveguides induced by optical vortex solitons", *Optics Letter*, Vol. 25, No. 9, May 2000, pp. 660-662.

[8] Isaac Freund, "Optical vortex trajectories", *Optics Communications*, Vol. 181, July 2000, pp. 19-33.

[9] Jennifer E. Curtis and David G. Grier, "Modulated optical vortices", *Optics Letters*, Vol. 28, No. 11, June 2003, pp. 872-874.

[10] M. V. Berry, "Optical vortices evolving from helicoidal integer and fractional phase steps", *Journal of Optics A: Pure Applied Optics*, Vol. 6, 2004, pp. 259-268.

[11] F. Flossmann, U.T. Schwarz and Max Maier, "Propagation dynamics of optical vortices in Laguerre–Gaussian beams", *Optics Communications*, Vol. 250, 2005, pp. 218-230.

[12] J. Leach, M. R. Dennis, J. Courtial1 and M. J. Padgett, "Vortex knots in light", *New Journal of Physics*, Vol. 7, 2005, pp. 55-65.

[13] K. N. Alekseyev and M. A. Yavorsky, "Propagation of optical vortices in coiled weakly guiding optical fibers", *Optics and Spectroscopy*, Vol. 102, No. 5, 2007, pp. 754-759.

[14] Greg Gbur and Robert K. Tyson, "Vortex beam propagation through atmospheric turbulence and topological charge conservation", *Journal of the Optical Society of America A*, Vol. 25, No. 1, January 2008, pp. 225-230.

[15] Cheng Ke, Liu Pu-Sheng and Lu Bai-Da, "Composite optical vortices in noncollinear Laguerre-Gaussian beams and their propagation in free space", *Chinese Physics B*, Vol. 17, No. 5, May 2008, pp. 1743-1751.

[16] Pascal Fischer, Susan E. Skelton, Christopher G. Leburn, Casey T. Streuber, Ewan M. Wright and Kishan Dholakia, "Propagation and diffraction of optical vortices", *Physica C*, Vol. 468, 2008, pp. 514-517.

[17] Peter Hansinger, Alexander Dreischuh and Gerhard G. Paulus , "Optical vortices in self-focusing Kerr nonlinear media", *Optics Communications*, Vol. 282, 2009, pp. 3349-3355.

[18] Yanpeng Zhang, Zhiqiang Nie, Yan Zhao, Changbiao Li, Ruimin Wang, Jinhai Si and Min Xiao, "Modulated vortex solitons of four-wave mixing", *Optics Express*, Vol. 18, No. 11, May 2010, pp. 10963-10972.

[19] H. T. Dai, Y. J. Liu, D. Luo and X. W. Sun, "Propagation dynamics of an optical vortex imposed on an Airy beam", *Optics Letters*, Vol. 35, No. 23, December 2010, pp. 4075-4077.

[20] Seyedali Vedad and Alireza Heidari, "An analytical and numerical investigation of the optical vortex solitons a computational study", *Applied Physics Research*, Vol. 4, No. 1, February 2012, pp. 78-90.

[21] C. N. Alexeyev, "Are optical vortices robust in twisted fibres", *Journal of Optics*, Vol. 14, 2012, pp. 1-6.

[22] Chengliang Zhao, Fei Wang, Yuan Dong, Yujing Han and Yangjian Cai, "Effect of spatial coherence on determining the topological charge of a vortex beam", *Applied Physics Letters*, Vol. 101, Issue 26, 2012, pp. 1104-1108.

[23] Pravin Vaity and R. P. Singh, "Topological charge dependent propagation of optical vortices under quadratic phase transformation", *Optics Letters*, Vol. 37, No. 8, April 2012, pp. 1301-1303.

[24] J. Demas, M. D. W. Grogan, T. Alkeskjold and S. Ramachandran1, "Sensing with optical vortices in photonic-crystal fibers", *Optics Letters*, Vol. 37, No. 18, September 2012, pp. 3768-3770.

[25] Yongzhou Ni and Guoquan Zhou, "Propagation of a Lorentz-Gauss vortex beam through a paraxial ABCD optical system", *Optics Communications*, Vol. 291, 2013, pp. 19-25.

[26] Dongmei Deng, Chidao Chen, Xin Zhao and Huagang Li, "Propagation of an Airy vortex beam in uniaxial crystals", *Applied Physics B Lasers and Optics*, Vol. 110, 2013, pp. 433-436.

[27] Xinzhong Li, Yuping Tai, Zhaogang Nie, Liping Zhang and Gengxin Yin, "Propagation properties of optical vortices in random speckle field based on Fresnel diffraction scheme", *Optics Communications*, Vol. 287, 2013, pp. 6-11.

[28] P. Jia, Y. Yang, C. J. Min, H. Fang and X. C. Yuan, "Sidelobe-modulated optical vortices for free-space communication", *Optics Letters*, Vol. 38, No. 4, February 2013, pp. 588-590.

[29] A. Buryak and N. Akhmediev, "Stationary pulse propagation in N-core nonlinear fiber arrays", *IEEE Journal of Quantum Electronics*, Vol.31, No.4, pp.682-688, 1995.

[30] Jianke Yang and Ziad H. Musslimani, "Fundamental and vortex solitons in a two-dimensional optical lattice", *Optics Letters*, Vol.28, No.21, pp.2094-2096, 2003.

[31] Tristram J. Alexander, Andrey A. Sukhorukov and Yuri S. Kivshar, "Asymmetric vortex solitons in nonlinear periodic lattices", *Physical Review Letters*, Vol.93, No.6, pp.63901-63905, 2004.

[32] Dragomir N. Neshev, Tristran J. Alexander, Elena A. Ostrovskaya, Yuri S. Kivshar, Hector Martin, Igor Makasyuk and Zhigang Chen, "Observation of discrete vortex solitons in optically induced photonic lattices", *Physical Review Letters*, Vol.92, No.12, pp.123903-123906, 2004.

[33] Zhigang Chen, Hector Martin and Anna Bezryadina, "Experiments on Gaussian beams and vortices in optically induced photonic lattices", *Journal of the Optical Society of America B*, Vol.22, No.7, pp.1395-1405, 2005.

[34] Maria I. Rodas-Verde and Humberto Michinel, "Dynamics of vector solitons and vortices in two-dimensional photonic lattices", *Optics Letters*, Vol.31, No.5, pp.607-609, 2006.

[35] Bernd Terhalle, Tobias Richter, Anton S. Desyatnikov, Dragomir N. Neshev, Wieslaw Krolikowski, Fiedemann Kaiser, Comelia Denz and Yuri S. Kivshar, "Observation of multivortex solitons in photonic lattices", *Physical Review Letters*, Vol.101, pp.13903-13906, 2008.

[36] Bernd Terhalle, Tobias Richter, Kody J. H. Law, Dennis Gories, Patrick Rose, Tristram J. Alexander, Panayotis G. Kerekidis, Anton S. Desyatnikov, Wieslaw Krolikowski, Fiedemann Kaiser, Comelia Denz and Yuri S. Kivshar, "Observation of double-charge discrete vortex solitons in hexagonal photonic lattices", *Physical Review A*, Vol.79, pp.43821-43829, 2009.

[37] Kody J. H. Law and P. G. Kevrekidis, "Stable higher-charge discrete vortices in hexagonal optical lattices", *Physical Review A*, Vol.79, pp.25801-25805, 2009.

[38] K. Murphy, D. Burke, N. Devaney and C. Dainty, "Experimental detection of optical vortices with a Shack-Hartmann wavefront sensor", *Optics Express*, Vol. 18, No. 15, 2010, pp. 15448-15460.

[39] C. Huang, H. Huang, H. Toyoda, T. Inoue and H. Liu, "Correlation matching method for high-precision position detection of optical vortex using Shack–Hartmann wavefront sensor", *Optics Express*, Vol. 20, No. 24, 2012, pp. 26099-26109.

[40] B. Stoklasa, L. Motka, J. Rehacek, Z. Hradil and L. Sanchez-Soto, "Wavefront sensing reveals optical coherence", *Nature Communications*, 5:3275, February 2014.

[41] J. J. Gribble and J. M. Arnold, "Beam-propagation method ray Equation", *Optics Letters*, Vol. 13, No. 8, 1988, pp. 611-613.

[42] M. Matsuhara, "A novel beam propagation method based on the Galerkin method", *Electronics and communications in Japan*, Part 2, Vol. 73, No. 5, 1990, pp. 41-47.

[43] J. Gerdes and R. Pregla, "Beam-propagation algorithm based on the method of lines", *Journal of the Optical Society of America B*, Vol. 8, No. 2, 1991, pp. 389-394.

[44] P. Vanbrabant, J. Beeckman1, K. Neyts, R. James and F. Fernandez, "A finite element beam propagation method for simulation of liquid crystal devices", *Optics Express*, Vol. 17, No. 13, 2009, pp. 10895- 10909.

[45] Lars Thylen and Chung Ming Lee, "Beam-propagation method based on matrix diagonalization", *Journal of the Optical Society of America A*, Vol. 9, No. 1, 1992, pp. 142-146.

[46] David Yevick, and Bjorn Hermansson, "Efficient beam propagation techniques", *IEEE Journal of Quantum Electronics*, Vol. 26, No. 1, 1990, pp. 109-112.

[47] H. Hoekstra, O. Noordman, G. Krijnen, R. Varshney and E. Henselmans, "Beam-propagation method for second-harmonic generation in waveguides with birefringent materials", *Journal of the Optical Society of America B*, Vol. 14, No. 7, 1997, pp. 1823-1830.

[48] Y. Tsuji, M. Koshiba and T. Tanabe, "A wide-angle beam propagation method using a finite element scheme", *Electronics and communications in Japan*, Part 2, Vol. 80, No. 1, 1997, pp. 18-26.

[49] C. R. Doerr, "Beam propagation method tailored for step-index waveguides", *IEEE Photonics Technology Letters*, Vol. 13, No. 2, 2001, pp. 130-132.

[50] Pui Lin Ho and Ya Yan Lu, "A bidirectional beam propagation method for periodic waveguides", *IEEE Photonics Technology Letters*, Vol. 14, No. 3, 2002, pp. 325-327.

[51] J. Wanguemert-Perez, I. Molna-Fernandez and M. Luque-Nieto, "A novel Fourier based 3D full-vectorial beam propagation method", *Optical and Quantum Electronics*, Vol. 36, 2004, pp. 285-301.

[52] Chin-Sung Hsiao, Likarn Wang and Y. J. Chiang, "An algorithm for beam propagation method in matrix form", *IEEE journal of Quantum Electronics*, Vol. 46, No. 3, 2010, pp. 332-339.

[53] Sami A. Shakir, Raymond Andrew Motes and Richard W. Berdine, "Efficient scalar beam propagation method", *IEEE Journal of Quantum Electronics*, Vol. 47, No. 4, 2011, pp. 486-491.

[54] R. Andrew Motes, Sami A. Shakir and Richard W. Berdine, "An efficient scalar, non-paraxial beam propagation method", *Journal of Lightwave Technology*, Vol. 30, No. 1, 2012, pp. 4-8.

[55] Youngchul Chung and Nadir Dagli, "An assessment of finite difference beam propagation method", *IEEE Journal of Quantum Electronics*, Vol. 26, No. 8, 1990, pp. 1335-1339.

[56] Hsu-Feng Chou, Ching-Fuh Lin and Gin-Chung Wang, "An iterative finite difference beam propagation method for modeling second-order nonlinear effects in optical waveguides", *Journal of Lightwave Technology*, Vol. 16, No. 9, 1998, pp. 1686-1693.

[57] Susumu Yoneta, Masanori Koshiba and Yasuhide Tsuji, "Combination of beam propagation method and finite element method for optical beam propagation analysis", *Journal of Lightwave Technology*, Vol. 17, No. 11, 1999, pp. 2398-2404.

[58] Jun Shibayama, Tomokazu Takahashi, Junji Yamauchi and Hisamatsu Nakano, "Comparative study of absorbing boundary conditions for the time-domain beam propagation method", *IEEE Photonics Technology Letters*, Vol. 13, No. 4, 2001, pp. 314-316.

[59] Yuta Nito, *et al*, "A beam-propagation method using both electric and magnetic fields", *IEEE Photonics Technology Letters*, Vol. 23, No. 7, 2011, pp. 429-431.

[60] W. P. Huang, C. L. Xu, and S. K. Chaudhuri, "A finite-difference vector beam propagation method for three-dimensional waveguide structures", *IEEE Photonics Technology Letters*, Vol. 4, No. 2, 1992, pp. 148-151.

[61] C. L. Xu, *et al*, "A full-vectorial beam propagation method for anisotropic waveguides", *Journal of Lightwave Technology*, Vol. 12, No. 11, 1994, pp. 1926-1931.

[62] W. P. Huang, C. L. Xu, and S. K. Chaudhuri, "A vector beam propagation method based on H fields", *IEEE Transactions Photonics Technology Letters*, Vol. 3, No. 12, 1991, pp. 1117-1120.

[63] J. F. Nye and M. V. Berry, ''Dislocations in wave trains'', *Proceedings of the Royal Society Series A*, Vol. 336, 1974, pp. 165-190.

[64] M. V. Berry and M. R. Dennis, "Knotted and linked phase singularities in monochromatic waves", *Proceedings of the Royal Society Series A*, Vol. 457, 2001, pp. 2251-2263.

[65] W. P. Huang, C. L. Xu, S. T. Chu and S. K. Chaudhuri, "A vector beam propagation method for guided-wave optics", *IEEE Photonics Technology Letters*, Vol. 3, No. 10, 1991, pp. 910-913.

[66] G. L. Yip and P. C. Noutsios, "An improved finite-difference vector beam propagation formulation for graded-index waveguides", *IEEE Photonics Technology Letters*, Vol. 6, No. 4, 1994, pp. 543-545.

[67] C. L. Xu, W. P. Huang, S. K. Chaudhuri and J. Chrostowski, "An unconditionally stable vectorial beam propagation method for 3-D structures", *IEEE Photonics Technology Letters*, Vol. 6, No. 4, 1994, pp. 549-551.

[68] Lars Thylen and David Yevick, "Beam propagation method in anisotropic media", *Applied Optics*, Vol. 21, No. 15, 1982, pp. 2751-2754.

[69] C. L. Xu, W. P. Huang, and S. K. Chaudhuri, "Efficient and accurate vector mode calculations by beam propagation method", *Journal of Lightwave Technology*, Vol. 11, No. 7, 1993, pp. 1209-1215.

[70] C. L. Xu and W. P. Huang, "finite difference beam propagation method for guided wave optics", *PIER*, Vol. 11, 1995, pp. 1-49.

[71] Lizhong Sun and Gar Lam Yip, "Modified finite-difference beam-propagation method based on the Douglas scheme", *Optics Letters*, Vol. 18, No. 15, 1993, pp. 1229-1231.

[72] http://gcc.gnu.org/fortran/

[73] http://www.gnuplot.info/

[74] R. M. Feshchenko and A. V. Popov, "Exact transparent boundary condition for the parabolic Equation in a rectangular computational domain", *Journal of the Optical Society of America A*, Vol. 28, No. 3, 2011, pp. 373-380.

[75] D. Jimenez and F. Perez-Murano, "Improved boundary conditions for the beam propagation method", *IEEE Photonics Technology Letters*, Vol. 11, No. 8, 1999, pp. 1000-1002.

[76] Akihiro Maruta, Yasuyuki Arai and Masanori Matsuhara, "Transparent boundary for finite-element beam-propagation method", *Electronics and Communications in Japan*, Part 2, Vol. 77, No. 5, 1994, pp. 32-38.

[77] G. Ronald Hadley, "Transparent boundary-condition for beam propagation", *Optics Letters*, Vol. 16, No. 9, 1991, pp. 624-626.

[78] G. Ronald Hadley, "Transparent boundary-condition for the beam propagation method", *IEEE Journal of Quantum Electronics*, Vol. 28, No. 1, 1992, pp. 363-370.

[79] B. Saleh and M Teich, "*Fundamentals of photonics*", John Wiley & Sons Inc., New Jersey, 2007.

[80] Isaac Freund, "Optical vortices in Gaussian random wave fields statistical probability densities", *Journal of the Optical Society of America A*, Vol. 11, No. 5, 1994, pp. 1644-1652.

[81] Natalya Shvartsman and Isaac Freund, "Vortices in random wave fields nearest neighbor anticorrelations", *Physical Review Letters*, Vol. 72, No. 7, 1994, pp. 1008-1011.

[82] Emil Zolotoyabko, "Basic concepts of crystallography", Wiley, 2011.

[83] Xinzhong Li, Yuping Tai, Zhaogang Nie, Liping Zhang and Gengxin Yin, "Propagation properties of optical vortices in random speckle field based on Fresnel

diffraction scheme", *Optics Communications*, Vol. 287, 2013, pp. 6-11.

[84] Muhammad A. Mushref, "Vortex field propagation in a hexagonal multicore fiber array", *Optics and Photonics Journal*, Vol. 4, No. 1, 2014, pp. 1-7.

[85] J. Udovich, N. Kirkpatrick, A. Kano, A. Tanbakuchi, U. Utzinger and A. Gmitro, "Spectral background and transmission characteristics of fiber optic imaging bundles", *Applied Optics*, Vol. 47, No. 25, 2008, pp. 4560-4568.

[86] http://www.thorlabs.com/newgrouppage9.cfm?objectgroup_id=2946

[87] X. Li, S. Lin, J. Liang, Y. Zhang, H. Oigawa and T. Ueda, "Fiber-optic temperature sensor based on difference of thermal expansion coefficient between fused silica and metallic materials", *IEEE Photonics Journal*, Vol. 4, No. 1, 2012, pp. 155-162.

[88] A. Polyanin and V. Zaitsev, "Handbook of Exact Solutions for Ordinary Differential Equations", Chapman & Hall/CRC Press, Boca Raton, 2003.

CURRICULUM VITA

Muhammad Abdulrahman Abdulghani Mushref
Place of Birth: Almadeenah, Saudi Arabia

EXPERIENCE

01.09.1991 – 01.09.2007   Saudi Telecom (STC), Jeddah, Saudi Arabia
    Worked in different areas in management, engineering and maintenance.

EDUCATION

PhD, University of Wisconsin - Milwaukee, August 2014
Major: Electrical Engineering
Dissertation: Propagation of an optical vortex in fiber arrays with triangular lattices.

MBA, University of Leicester, Leicester, UK, February 2009
Major: Business Administration
Thesis: Evaluation and analysis of work teams dynamics for successful implementation
    of strategic and managerial decision making.

MSc, King Abdulaziz University, Jeddah, Saudi Arabia, February 2006
Major: Nuclear Engineering
Thesis: Characterization of a sodium iodide detector using MCNP.

MSc, Brunel University, London, UK, July 1999
Major: Data Communications Systems
Thesis: Microwave modulation of semiconductor lasers for high speed transmission of
    signals in optical fiber communication systems.

MSc, University of Sunderland, Sunderland, UK, November 1998
Major: Computer Based Information Systems
Thesis: Design and implementation of a real time telephone monitoring and control
    system using scheduling algorithms in concurrent programming.

BSc, King Fahd University, Dhahran, Saudi Arabia, August 1991
Major: Electrical Engineering
Senior project: A line of site optical communications network.

PUBLICATIONS:

1. Muhammad Mushref, "Managing conflict in a changing environment", *Management Services*, Vol. 46, No. 11, Nov. 2002, pp. 8–11.

2. Muhammad Mushref, "Radiogauging checks the quality of mixtures", *Engineering Technology*, Vol. 6, No. 10, December 2003 – Jan. 2004, pp. 50.

3. Muhammad Mushref, "Radiation from a dielectric – coated cylinder with two slots", *Applied Mathematics Letters*, Vol. 71, No. 6, Jun. 2004, pp. 721–727.

4. Muhammad Mushref, "Transverse magnetic scattering of two incident plane waves by a dielectric coated cylindrical reflector", *Central European Journal of Physics*, Vol. 3, No. 2, 2005, pp. 229–246.

5. Muhammad Mushref, "Field characteristics from an eccentric dielectric coated circular cylinder with two axial slots", *Electromagnetics*, Vol. 25, No. 1, Jan. 2005, pp. 55–67.

6. Muhammad Mushref, "TM radiation from an eccentric dielectric coated cylinder with two infinite slots", *Journal of Electromagnetic Waves and Applications*, Vol. 19, No. 5, 2005, pp. 577–590.

7. Muhammad Mushref, "Analytical solution to electromagnetic scattering of N plane waves by a coated cylinder", *WSEAS Transactions on Electronics*, Vol. 3, No. 8, Aug. 2006, pp. 403–409.

8. Muhammad Mushref, "TM radiations from a coated cylinder with two slots", *WSEAS Transactions on Mathematics*, Vol. 6, No. 2, Feb. 2007, pp. 419–422.

9. Muhammad Mushref, "Closed solution to electromagnetic scattering of a plane wave by an eccentric cylinder coated with metamaterials", *Optics Communications*, Vol. 270, No. 2, 15 Feb. 2007, pp. 441–446.

10. Muhammad Mushref, "Matrix solution to electromagnetic scattering by a conducting cylinder with an eccentric metamaterial coating", *Journal of Mathematical Analysis and Applications*, Vol. 332, No. 1, Aug. 2007, pp. 356–366.

11. Muhammad Mushref, "Electromagnetic radiation from an eccentric coated cylinder with N slots of arbitrary sizes and positions", *Progress In Electromagnetic Research B*, Vol. 11, 2009, pp. 55–78.

12. Muhammad Mushref, "Electromagnetic radiation from a coated cylinder with two arbitrary slots", *High Frequency Electronics*, Vol. 9, No. 2, Feb. 2010, pp. 47–54.

13. Muhammad Mushref, "Fourier-Bessel expansions with arbitrary radial boundaries", *Applied Mathematics*, Vol. 1, No. 1, 2010, pp. 18–23.

14. Muhammad Mushref, "Radiations from an eccentric coated cylinder with N slots", *Journal of Electromagnetic Analysis and Applications*, Vol. 3, No. 8, Aug. 2011, pp. 305-311.

15. Muhammad Mushref, "Vortex field propagation in a hexagonal multicore fiber array", *Optics and Photonics Journal*, Vol. 4, No. 1, 2014, pp. 1-7.